MONITORING THE ANTARCTIC ICE SHEET FROM SPACE

by

Benjamin Lambert

A thesis submitted to the faculty of

Brigham Young University

in partial fulfillment of the requirements for the degree of

Master of Science

Department of Electrical and Computer Engineering

Brigham Young University

August 2008

BRIGHAM YOUNG UNIVERSITY

GRADUATE COMMITTEE APPROVAL

of a thesis submitted by

Benjamin Lambert

This thesis has been read by each member of the following graduate committee and by majority vote has been found to be satisfactory.

Date	David G. Long, Chair
Date	Brian D. Jeffs
Date	Richard W. Christiansen

BRIGHAM YOUNG UNIVERSITY

As chair of the candidate's graduate committee, I have read the thesis of Benjamin Lambert in its final form and have found that (1) its format, citations, and bibliographical style are consistent and acceptable and fulfill university and department style requirements; (2) its illustrative materials including figures, tables, and charts are in place; and (3) the final manuscript is satisfactory to the graduate committee and is ready for submission to the university library.

Date

David G. Long
Chair, Graduate Committee

Accepted for the Department

Michael J. Wirthlin
Graduate Coordinator

Accepted for the College

Alan R. Parkinson
Dean, Ira A. Fulton College of
Engineering and Technology

ABSTRACT

MONITORING THE ANTARCTIC ICE SHEET FROM SPACE

Benjamin Lambert

Department of Electrical and Computer Engineering

Master of Science

The Antarctic ice sheet is a geophysically - and in an age of growing concern about global warming, geopolitically - important portion of Earth. The composition and dynamics of the Antarctic ice sheet influence global climate patterns, global sea level and the planet's radiation budget. Recent evidence also suggests that the long term stability of portions of the ice sheet may be in jeopardy.

In this thesis I use data from three Ku-band space-borne scatterometers to monitor changes in the backscatter signature of the Antarctic ice sheet from 1978 through 2007. Significant changes in backscatter, which result from topographic and geophysical changes in the ice sheet itself, are found over much of the Antarctic continent, especially in West Antarctica and along much of the coasts. Less drastic changes, including regular seasonal variations, are observed over much of the ice shelf. Possible scattering mechanisms are proposed and discussed. A secondary result is the demonstration of the stability of NASA's QuikSCAT scatterometer, data from which is used extensively in this thesis and in many other publications. It is shown that QuikSCAT's observation geometry and backscatter instrumentation have remained consistent to great precision throughout it nearly nine year mission.

ACKNOWLEDGMENTS

Many students use this space to acknowledge the help of parents, spouses, children, academic advisers, and the such. I will be no different. I'd like to thank Charlie, Ruth, Natalie, Isaac, Micah, Dr. Long, and the such for their support, love, encouragement, enthusiasm, laughter, and guidance.

Table of Contents

List of Tables

List of Figures

Chapter 1

Introduction

The Antarctic ice sheet is a geophysically - and in an age of growing concern about global warming, geopolitically - important portion of Earth. The composition and dynamics of the Antarctic ice sheet influence global climate patterns, global sea level, and the planet's radiation budget. Recent evidence suggests that the long term stability of portions of the ice sheet may be in jeopardy [1]. Thus there is an urgent need to study and understand the workings of the Antarctic ice sheet and its interactions with local and global climate patterns.

1.1 Previous Work

Historically, the study of remote and inhospitable locals such as Antarctica and the Arctic, including Greenland, have been difficult, expensive, dangerous, and of too small a scale to be globally applicable. With the advent and refinement of satellite and microwave remote sensing technology scientists have been able to observe these regions from space. Microwave remote sensing is advantageous in that it allows for observations through cloud cover and without regard for time of day.

Study of Antarctica from space began in earnest with the launch of NASA's Ku-band Seasat Scatterometer (SASS) in 1978. Although SASS's mission was short-lived it proved the utility of space-borne remote sensing of many targets, including ice and snow. The European Space Agency launched identical scatterometers on-board their ERS-1 and ERS-2 platforms from 1992 through 2001. These instruments operated at a much lower C-band frequency, than did SASS, but proved the utility of studying temporal changes in ice sheet backscatter [2, 3, 4]. More recent missions

of the Ku-band instruments NSCAT, SeaWinds, and QuikSCAT have allowed for additional studies [5, 6, 7].

It is interesting to note that all of the sensors mentioned above were designed not to observe ice and snow, but to infer near-surface wind speeds by observing the backscatter from oceans. The studies mentioned here, as well as studies estimating soil erosion [8], deforestation [9], and sand dune formation [10] have been influenced by wind scattering theory and instrumentation. In addition to these active remote sensing (scatterometer) studies there has been much success using passive remote sensing instruments (radiometers) to monitor the ice sheets, for example [3, 11].

1.2 Purpose of This Thesis

The purpose of this thesis is to expand upon the work of previous researchers and present a comprehensive survey of the ku-band backscatter signature of the Antarctic ice sheet from 1978 to the present, contributing useful data to the ongoing discussion regarding the relationship between global warming and ice sheet change. My work also contributes to the science of scattering from snow and ice in general.

My research using QuikSCAT adds spatial and temporal knowledge of the ice sheet that had eluded previous researchers using other instruments. QuikSCAT's dense azimuth sampling allows for very precise, low-noise observations of azimuthally anisotropic scatterers that are abundant in much of Antarctica. This allows me to provide the first analysis of which I am aware that tracks the evolution of backscatter signature parameters other than average backscatter. The most recent large-scale survey of backscatter change from Antarctica of which I am aware is [4], which is now eight years old. Thus I am able to present new data regarding the possibly accelerating changes in the ice sheet. My research also demonstrates that QuikSCAT has operated consistently throughout its mission, a finding that validates numerous previous wind and rain studies that had assumed as much.

The respected thinker Clarence Darrow once remarked that "it is not the strongest of the species that survives, nor the most intelligent, but rather the one most adaptable to change." This thesis, then, represents my humble contribution to

the preservation of our species, by providing timely information about changes in the world we inhabit.

1.3 Organization of This Thesis

This thesis is organized as follows: I begin with a background discussion in Chapter 2. This discussion is meant to familiarize the reader with the overall nature of the Antarctic ice sheet, the basics of active scattering theory, and the instruments used. In Chapter 3 I demonstrate the stability and consistency of the QuikSCAT scatterometer. This is the most comprehensive demonstration of QuikSCAT's stability at the poles of which I am aware, and has consequences far beyond the scope of my thesis. In Chapter 4 I present and discuss important QuikSCAT-observed changes in the backscatter signature of the Antarctic ice sheet since from 1999 through 2007. In chapter 5 I expand my study to include data taken from other sensors and discuss important large-scale changes in the backscatter signature of the Antarctic ice sheet from 1978 through 2007. Chapter 6 provides a summary and discusses potential avenues for future work.

Chapter 2

Background

2.1 The Antarctic Ice Sheet

The most startling geographic feature of Antarctica, and perhaps of the whole Earth, is the kilometers-thick ice sheet under which more commonplace geographic features - planes, lakes, mountains - have been hidden from sight for millennia. The Antarctic ice sheet is by far the largest single mass of ice on Earth. It covers an area of almost 14 million km^2 and contains 30 million km^3 of ice [12]. Such vast stores of fresh water play an important role to global climate systems and as an indicator of climate change. The mass balance of the ice sheet is of particular importance due to its influence on sea level change and has been the subject of considerable research lately [13].

Figure 2.1 shows an elevation map and a composite optical, true-color image of the Antarctic continent. The highest point of Antarctica is nearly three miles above sea level. Many other interesting features, such as ice shelves, icebergs, and glacier floes, are apparent in the optical image.

The Antarctic ice system is often divided into four zones [16].

Dry snow zone – This is the largest region in the Antarctic and consists of areas where the snow never melts, even during the summer. In this region snow is transformed into ice through sintering, or compaction due to pressure caused by its own weight.

Percolation zone – This zone is classified by the presence of some surface melt during the summer. This water then seeps downward and eventually refreezes

into ice glands and lenses. This zone is limited to coastal regions, including ice shelves.

Wet snow zone – The wet snow zone is defined by the region where all of the previous year's accumulation has been raised to 0° C by the end of summer. This melt water then percolates into deeper snow layers, possibly causing them to melt as well. There are very few wet snow zones in Antarctica, all of which are located on the fringes of the Antarctic peninsula.

The locations corresponding to these zones according to Liu and others [11] is shown in Figure 2.2.

2.2 Scatterometry

Given Antarctica's size and inhospitable climate, *in situ* studies are very difficult. Space-borne microwave scatterometers however have the ability to make continental scale surveys despite inclement weather, climate, cloud cover, or light conditions.

Scatterometers are able to perform in such conditions by providing their own illumination, in the form of electromagnetic pulses directed at the Earth's surface. The return signal from such illumination is related to the target by the monostatic radar equation,

$$P_r = \frac{P_t G^2 \lambda^2 \sigma}{(4\pi)^3 R^4}, \tag{2.1}$$

where

P_r = Power received,

P_t = Power transmitted,

G = Antenna gain,

λ = wavelength,

σ = radar cross section of target,

R = distance to target.

The quantity of primary interest in this thesis is backscatter (σ^0), defined as the radar cross section, σ, normalized by the area of the resolution element. Backscatter essentially describes how well a target (or collection of targets) reflects incident energy back towards the radar, and depends on the target's physical and electrical properties, such as shape, size, orientation, roughness, dielectric constant and conductivity.

In this thesis I assume all scattering is from snow and ice, which is usually modeled as a collection of Rayleigh point scatterers in an air background. Over dry snow the penetration depth can be very large, resulting in substantial contributions from volume scatterers in addition to the scattering from the snow/air boundary. In Antarctica the snow pack is generally so deep as to render scattering from the ground/snow boundary negligible. The presence of liquid water in the snow pack decreases the penetration depth, which in turn decreases the contribution from volume scatterers and greatly reduces the total backscatter [17].

2.3 Sensors

The data used in this thesis comes from the three Ku-band space-borne scatterometers described here. The bulk of the data comes from QuikSCAT. All three sensors operate from a sun-synchronous polar orbit, and make approximately 14 revolutions per day.

2.3.1 SASS

The Seasat Scatterometer (SASS) was NASA's first Earth-orbiting scatterometer. It was launched on June 28, 1978 and was in operation until October 8 of the same year. SASS operated in interrupted CW mode at 14.6 GHz. It used four antennas to make observations at a variety of incidence and azimuth angles over two 500 km swaths separated by a 400 km nadir gap [18] [19]. Along beam resolution is achieved by Doppler filtering the return signal into 12 cross track resolution elements

("cells") each with nominal spatial resolution of 50 km. Along track resolution was achieved by exploiting knowledge of the movement of the satellite with respect to the earth. SASS operated primarily with each antenna transmitting and receiving V-pol data only [20].

2.3.2 NSCAT

The NASA scatterometer (NSCAT) flew aboard the ADEOS-1 platform from September 15, 1996 until June 29, 1997. NSCAT employed four antennas at V-pol and two antennas at dual (V and H) pol for a total of eight beams that made observations at a variety of incidence and azimuth angles over two 600 km wide swaths separated by a 330 km nadir gap. As with SASS, further Doppler processing resolved the observations into 24 cross track cells, and timing knowledge was exploited to resolve along track observations into 25 km cells as well. NSCAT observations were made at 13.995 GHz [21].

2.3.3 QuikSCAT

QuikSCAT was launched as a successor to NSCAT. Unlike SASS and NSCAT, it employs two rotating pencil beam antennas at discreet incidence angles, V-pol at 54.25° and H-pol at 46.44°, a configuration which allows for nearly continuous azimuth sampling. QuikSCAT has been in nearly continuous operation since its launch on June 19, 1999. The instantaneous QuikSCAT footprint is an elliptical 25 km by 37 km "egg" which is further divided by Doppler processing into nearly rectangular 6 km by 25 km "slices". QuikSCAT measurements are made at 13.6 GHz.

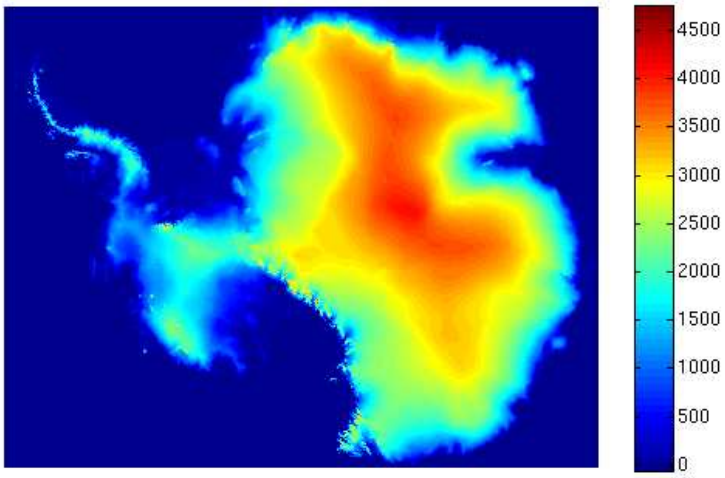

(a) Elevation map [14].

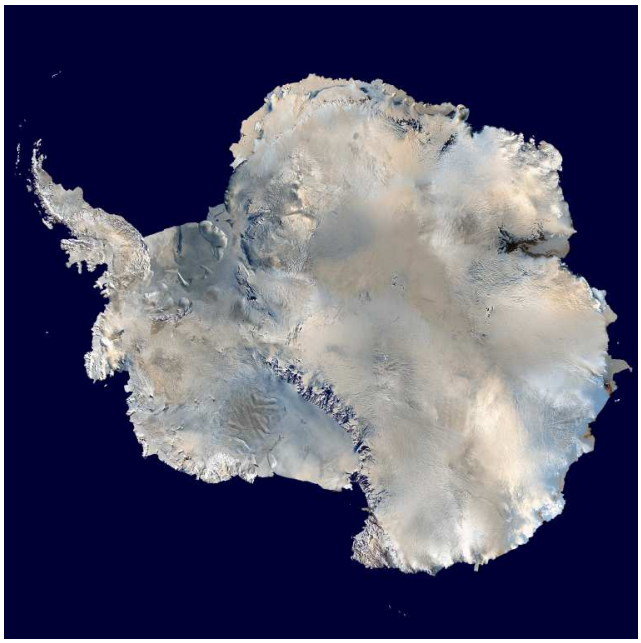

(b) True color composite image of Antarctica [15].

Figure 2.1: Antarctic maps

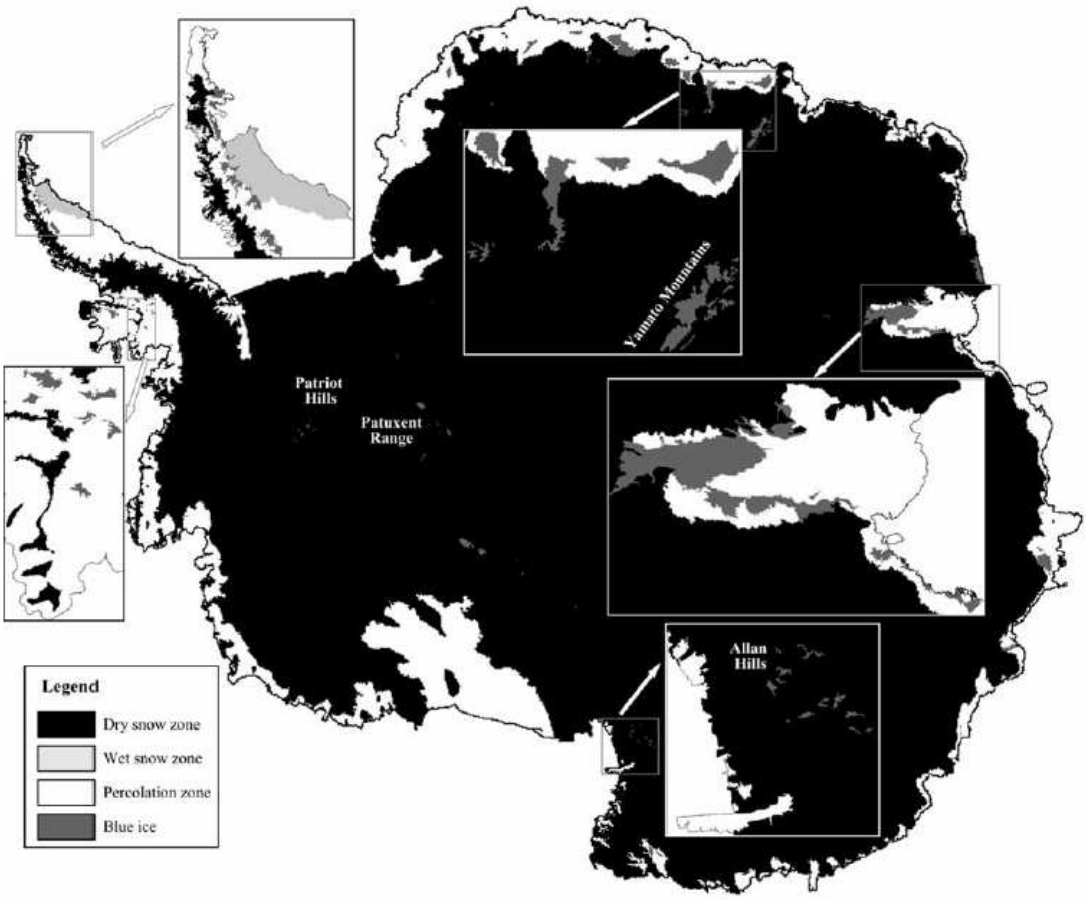

Figure 2.2: Location of snow zones, including blue ice zones, according to Liu [11].

Chapter 3

QuikSCAT Stability

The unprecedented duration of QuikSCAT's mission allows for long-term temporal analysis that has been impossible with previous space-born scatterometers, and in Chapter 4 I perform just such an analysis on observations of normalized backscatter from the Antarctic ice sheet. For the results to be geophysically meaningful however, I must first establish that QuikSCAT itself has been consistent, and that any changes observed are attributable to a dynamic target, not an unstable instrument. In this chapter I demonstrate that QuikSCAT has indeed been a stable instrument, and that observations from any time during its mission can be meaningfully compared. I proceed by first introducing my method for managing QuikSCAT's large data set, I then consider the consistency of QuikSCAT's observation geometry, and I then consider the backscatter from two Antarctic calibration targets.

3.1 Data Sets

The quantity of observations made by QuikSCAT (over one million every day from Antarctica alone) makes a comprehensive survey of 9 years of individual data points unmanageable. Thus I have found it necessary to bin data spatially and temporally, and the analysis in this section concerns statistics associated with bins of data, not individual observations

I use the term "observation" in this thesis to mean a single normalized radar backscatter measurement and its corresponding location and geometry. This results a total of seven quantities associated with every data point: backscatter, longitude, latitude, azimuth angle, incidence angle, polarization, and time. Thus the data used in this thesis is organized into such 7-tuples.

Bins are delineated temporally every four days, roughly corresponding to QuikSCAT's orbit period. Bins are delineated spatially by a simple griding process, an observation is included in an approximately 44.5 km by 44.5 km pixel if the center of the antenna footprint falls in that pixel. This pixel size is chosen to correspond to a 10 pixel by 10 pixel region from a QuikSCAT "egg" type image made with the Scatterometer Image Reconstruction algorithm [22]. I refer to these spatial bins as "pixels" throughout. In Appendix A I discuss the spatial resolution, temporal resolution, and noise trade-offs associated with this binning scheme in light of the backscatter change detection method used in Chapter 4.

This binning scheme results in a given location having 91 temporal bins per year, or 769 total temporal bins from QuikSCAT's launch in 1999 through the end of 2007. For a given four-day period the Antarctic continent is divided into approximately 7200 pixels. V-pol and H-pol data are treated separately. For consistency, data from other sensors used later in this thesis is also binned spatially according to these conventions.

The QuikSCAT data set has one known inconsistency, wherein the data reporting protocols used by NASA's Jet Propulsion Laboratory, the organization responsible for disseminating QuikSCAT's data set, were slightly modified in 2006 to correct for atmospheric effects observed during the mission of ADEOS-II in 2003 [23]. These changes effect my study only in how QuikSCAT reports incidence angle, and in section 3.2.2 are shown to be negligible.

3.2 Observation Geometry

A necessary (although in general not sufficient) condition for backscatter measurements to be meaningfully compared is that the observation geometries of each measurement be understood and controlled for. For example, its possible to attribute differences in observed backscatter from different azimuth angles and different times to a dynamic target, when in reality the target is simply an anisotropic scatterer. Thus it is necessary to demonstrate that QuikSCAT's observation geometry has remained consistent throughout its mission. To do this I consider five statistics: number of ob-

Table 3.1: Locations of three pixels for temporal study.

	Latitude	Longitude
Location 1	-74.5	123.0
Location 2	-78.5	106.9
Location 3	-71.0	4.0

servations, mean incidence angle, incidence angle standard deviation, mean azimuth angle, and azimuth angle standard deviation. In principle, if these quantities can be shown to have remained nearly constant in each data bin throughout QuikSCAT's mission, then it can be reasonably concluded that QuikSCAT has been a stable platform from which to make backscatter measurements.

I perform two types of analysis on each statistic. The first type of analysis is spatially broad but temporally disparate, using continent-wide data subsets from days 213 to 216, 1999, corresponding to the beginning of QuikSCAT's mission, and 357 to 360, 2007, which is the most recently available data. The purpose of this analysis is to demonstrate the spatial distribution of QuikSCAT's observation geometry parameters. The second type of analysis is temporally broad but spatially disparate, using data subsets from three selected locations, listed in Table 3.1, for the entire duration of QuikSCAT's mission. Locations 1 and 2 are chosen to correspond to regions analyzed in detail in Section 3.3, location 3 is chosen somewhat arbitrarily from a lower latitude far from locations 1 and 2. The purpose of this analysis is to demonstrate the temporally consistent nature of QuikSCAT's observation geometry. A complete analysis of both the temporal and spatial characteristics of QuikSCAT's observation geometry would require hundreds of pages and accomplish little that these two smaller analyses do not.

3.2.1 Number of Observations

Spatial Analysis

If the number of observations per bin changes, then the statistics associated with observation geometry parameters become less reliable. Figures 3.1 and 3.2 shows

the spatial distribution of QuikSCAT's observations in 1999 and 2007. In both Figures the distribution is as one would expect from an instrument in a polar sun-synchronous orbit, with the greatest density of observations occurring near QuikSCAT's southernmost extent.

The difference images display many pixels of small difference and a radially repeating patterns of large and small magnitudes. The zero-centered histograms and the spatial coherence of the difference maps suggest that the small observed changes from 1999 to 2007 are artifacts of slight orbital period mismatch of the two four-day periods observed. Indeed the total number of observations for each four day period (Table 3.2) varies on the order of one one-hundredth of a percent.

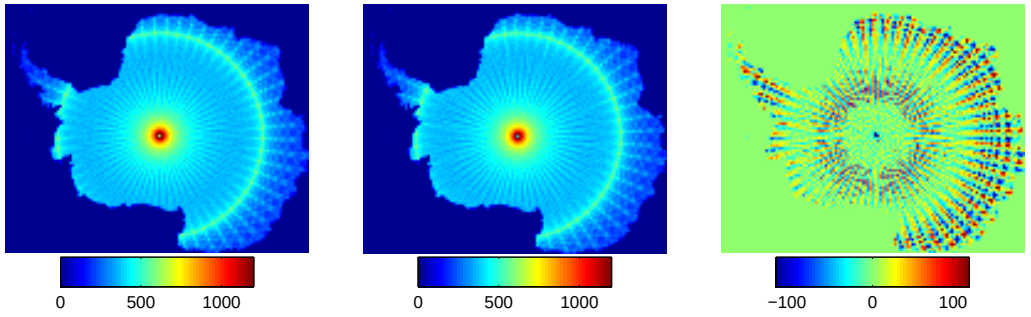

(a) Maps of the number of observations per pixel, V-pol. Left) 1999. Center) 2007. Right) Difference, 2007 - 1999.

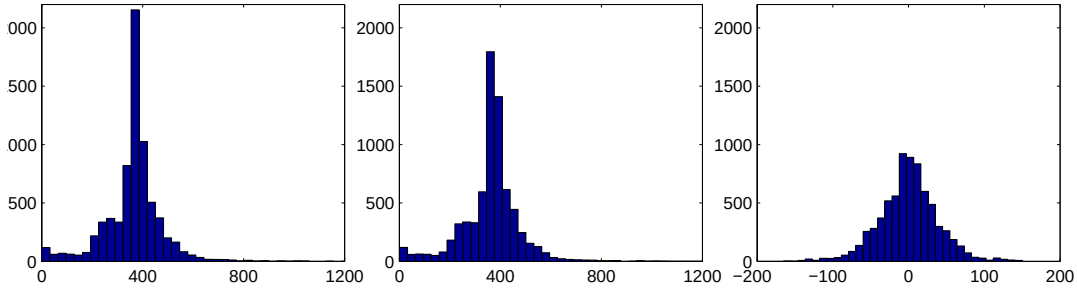

(b) Histograms of the number of observations per pixel. V-pol. Left) 1999. Center) 2007. Right) Difference, 2007 - 1999.

Figure 3.1: Number of observations per pixel. V-pol.

Table 3.2: Total Number of observations per four day period.

	1999	2007	difference	% difference
V-pol	2622301	2622576	275	0.0105
H-pol	2712639	2711969	-670	0.0247

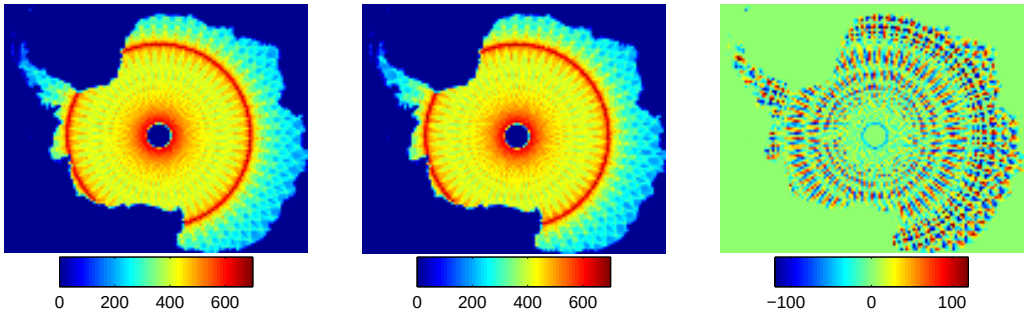

(a) Maps of the number of observations per pixel, H-pol. Left) 1999. Center) 2007. Right) Difference, 2007 - 1999.

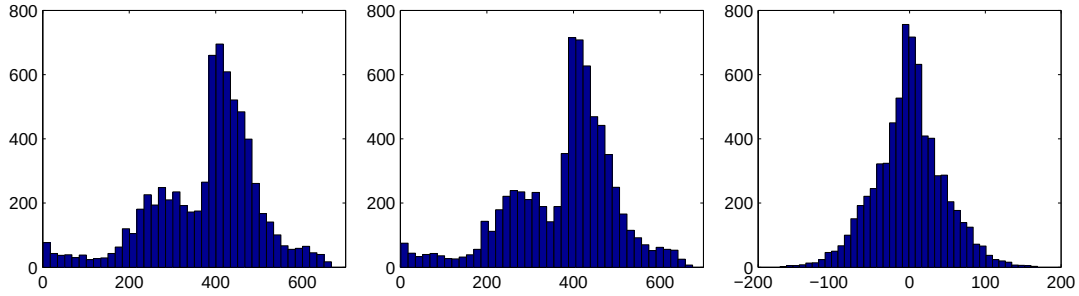

(b) Histograms of the number of observations per pixel. H-pol. Left) 1999. Center) 2007. Right) Difference, 2007 - 1999.

Figure 3.2: Number of observations per pixel. H-pol.

Temporal Analysis

Time series data of the number of observations per four day period at the three locations listed in Table 3.1 are shown in Figures 3.3, 3.4, and 3.5. Inspection of these plots shows some variability, but the overall trend is constant. The large magnitude, short duration, alternating polarity nature of anomalies suggests that much

of the variation can be attributed to QuikSCAT's not-quite-four-day orbit period. QuikSCAT has also experienced short instrument outages intermittently throughout its mission, resulting in missing observations. In all three locations the variations in H-pol data seem to lessen during the course of the mission, while the V-pol data appears consistently variable throughout.

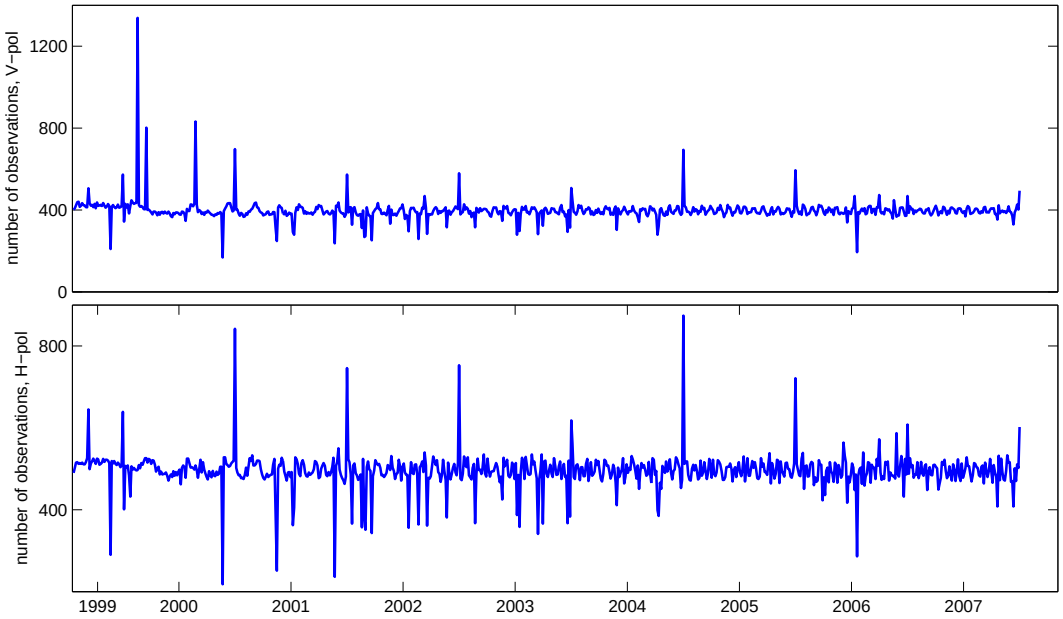

Figure 3.3: Time series of number of observations at location 1.

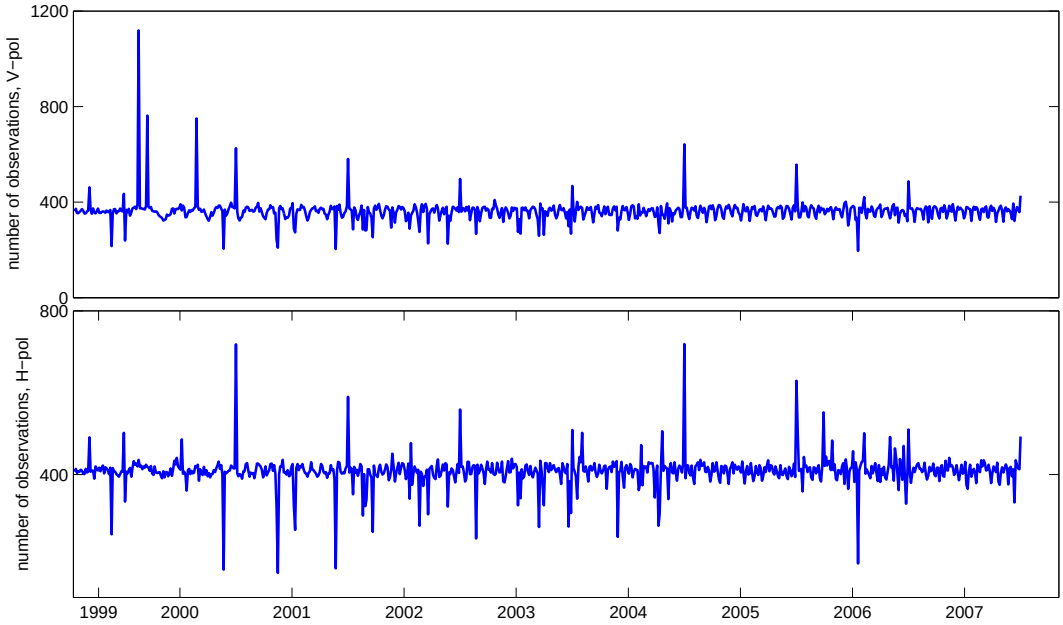

Figure 3.4: Time series of number of observations at location 2.

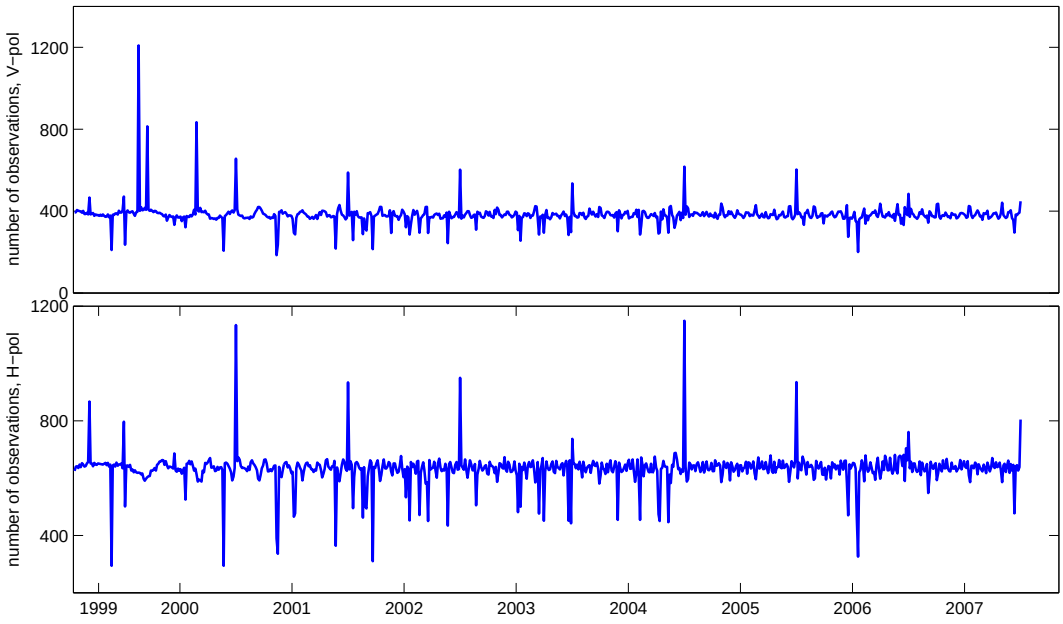

Figure 3.5: Time series of number of observations at location 3.

3.2.2 Incidence Angle

Spatial Analysis

I now consider spatial analysis of incidence angle mean and standard deviation, pixel-wise maps of which, along with corresponding histograms for V- and H-pol data are shown in Figures 3.6, 3.7, 3.8, and 3.9. These maps and histograms reveal several interesting things.

In both the V-pol and H-pol data sets the predominate mean incidence angle tended to be slightly smaller in the 2007 data than in the 1999 data. In 1999 the predominate V-pol mean incidence angle is 54.254°, in 2007 it is 54.206°. The corresponding H-pol values are 46.448° and 46.414°. In both cases the change is on the order of -0.03°, and is accompanied by a larger spread in incidence angle means. Both cases also show that no pixel exhibits a change in mean incidence angle greater than -0.054°.

Standard deviation data is also similar between the V- and H-pol data sets. In both cases standard deviation of incidence angle is larger and more spread out in 2007 than in 1999. In 1999 the predominate V-pol standard deviation is 0.0054°, in 2007 it is 0.0185°, while the predominate H-pol standard deviation is 0.0070° in 1999 and 0.0185° in 2007. No single pixel exhibits a change of more than 0.0195° from 1999 to 2007. Although the increase in standard deviation in general suggests a possible decreased stability, the magnitude of the resulting values remain very small, and temporal analysis confirms that much of the increase is attributable to changed data reporting procedures, as discussed in Section 3.1.

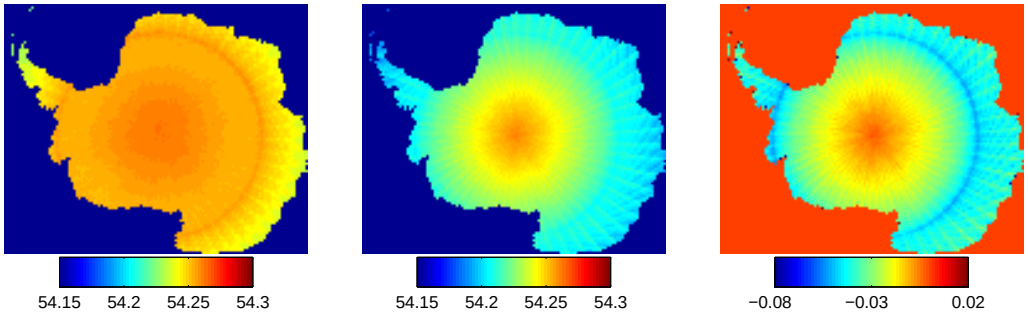

(a) Maps of V-pol mean incidence angle, in degrees. Left) 1999. Center) 2007. Right) Difference, 2007 - 1999. The isolated pixels along the coast showing large values are edge artifacts.

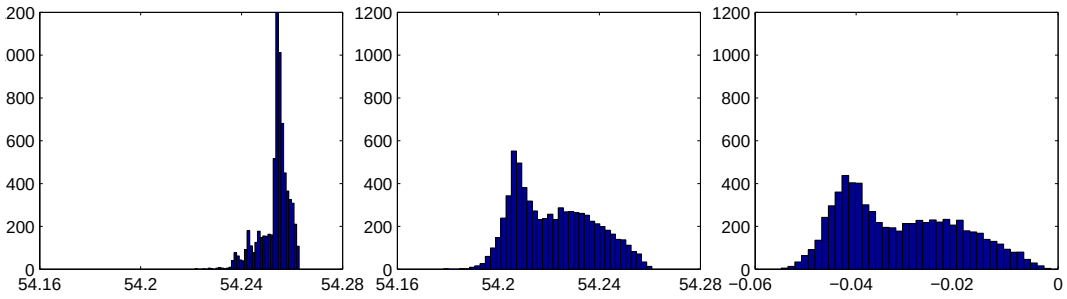

(b) Histograms of V-pol mean incidence angle, in degrees. Left) 1999. Center) 2007. Right) Difference, 2007 - 1999.

Figure 3.6: Mean incidence angle data, V-pol.

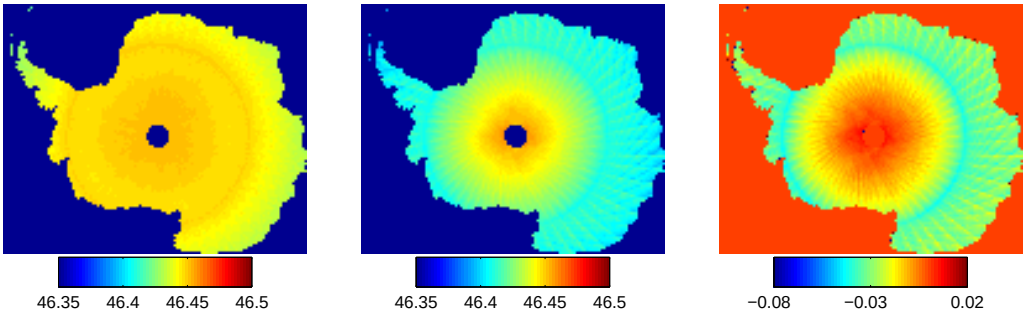

(a) Maps of H-pol mean incidence angle, in degrees. Left) 1999. Center) 2007. Right) Difference, 2007 - 1999. The isolated pixels along the coast showing large values are edge artifacts.

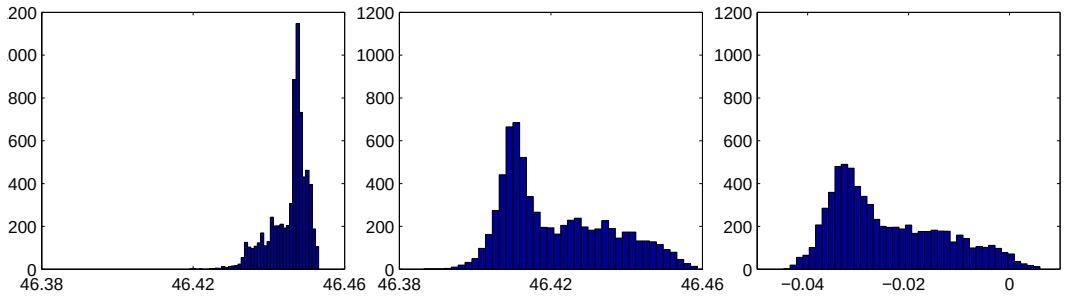

(b) Histograms of H-pol mean incidence angle, in degrees. Left) 1999. Center) 2007. Right) Difference, 2007 - 1999.

Figure 3.7: Mean incidence angle data, H-pol.

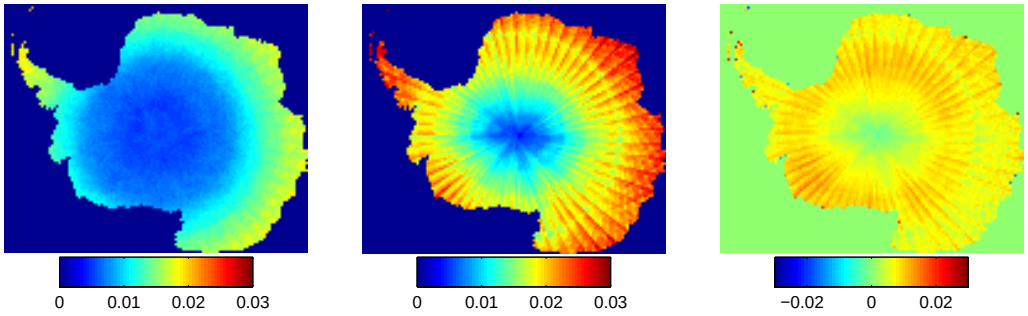

(a) Maps of V-pol incidence angle standard deviation, in degrees. Left) 1999. Center) 2007. Right) Difference, 2007 - 1999.

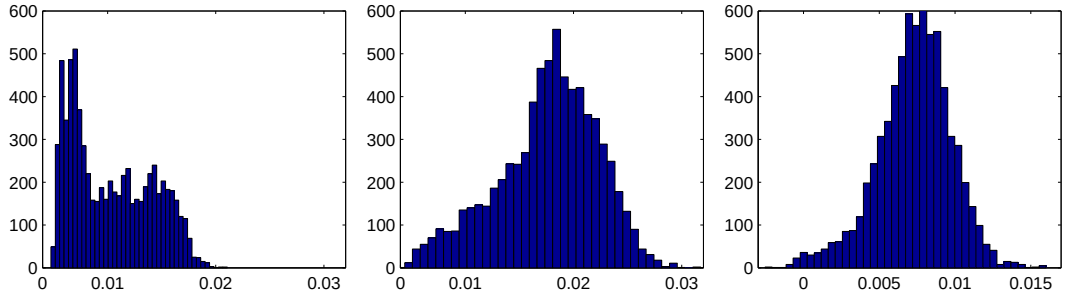

(b) Histograms of V-pol incidence angle standard deviation, in degrees. Left) 1999. Center) 2007. Right) Difference, 2007 - 1999.

Figure 3.8: Incidence angle standard deviation data, V-pol.

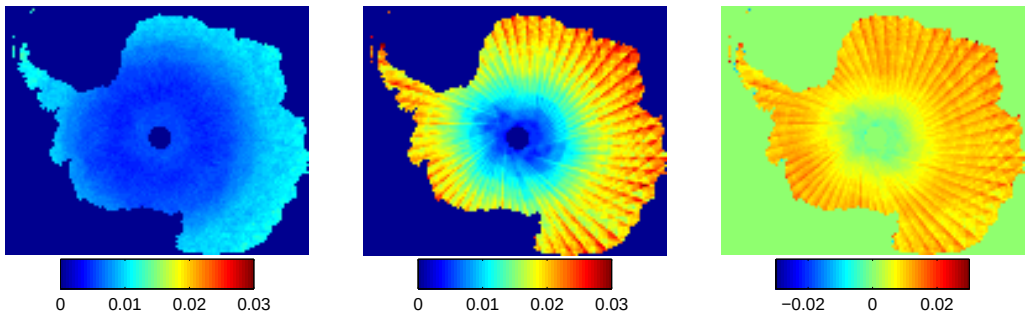

(a) Maps of H-pol incidence angle standard deviation, in degrees. Left) 1999. Center) 2007. Right) Difference, 2007 - 1999.

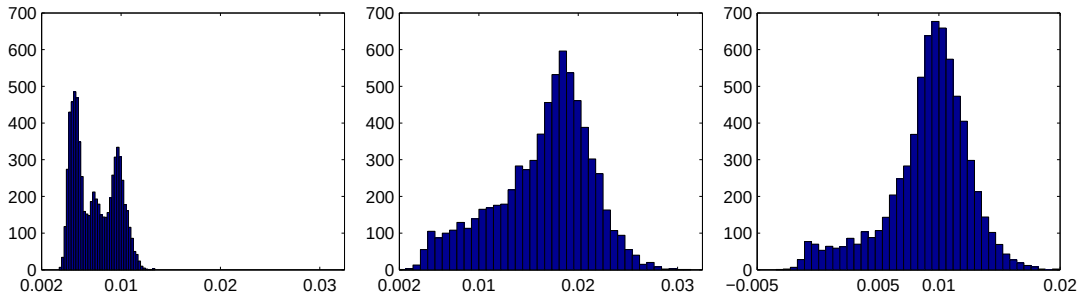

(b) Histograms of H-pol incidence angle standard deviation, in degrees. Left) 1999. Center) 2007. Right) Difference, 2007 - 1999.

Figure 3.9: Incidence angle standard deviation data, H-pol.

Temporal Analysis

A time series analysis of incidence angle statistics at the locations listed in Table 3.1 is shown in Figures 3.10, 3.11, 3.12. The trends revealed by these plots are very similar at all three locations and for both V- and H-pol data sets. In each case there are a few (usually three) data points at the beginning of the series where the values of mean and standard deviation vary much more than during the rest of the mission. During this initial period incidence angle means can vary by as much as 0.05°, and standard deviation can vary by as much as 0.1°. Anomalies at the beginning of the mission can be attributed to initial QuikSCAT operation and calibration before beginning its standard operation, and can thus be ignored.

After these slight initial wobbles, the statistics remain very stable for more than six years. During this span both mean and standard deviation vary periodically, with slight downward trends, over a range of approximately 0.01° and 0.001° respectively every 120 days. This periodic pattern is attributable to QuickSCAT's orbit geometry and Doppler processing. There is some deviation from this pattern, most noticeably in late 2001 (clearest in Figure 3.10, bottom), but for the most part this period is characterized by remarkable consistency.

Coincident with the beginning of 2006 all data sets abruptly begin to deviate from the pattern established during the previous six years. From the beginning of 2006 through the end of 2007 both mean and standard deviation statistics show an approximately annual periodicity during which they vary by as much as 0.05° and 0.02° respectively. These results are consistent with, and help to explain, the increased standard deviation in the continent-wide analysis from 1999 and 2007 seen previously. This change of scheme is entirely attributable to the changes in QuikSCAT's data processing, discussed above (Section 3.1).

In general, incidence angle is demonstrated to be stable to within approximately 0.02° throughout its mission, with a worst case change of approximately 0.05° in the three study locations. Since typical Ku-band dependence of backscatter from snow and ice on incidence angle tends to be on the order of -0.2 dB per degree, this worst case scenario corresponds to an approximately 0.1 dB change in observed

backscatter, which is well below the noise floor for typical short-term observations of Antarctica.

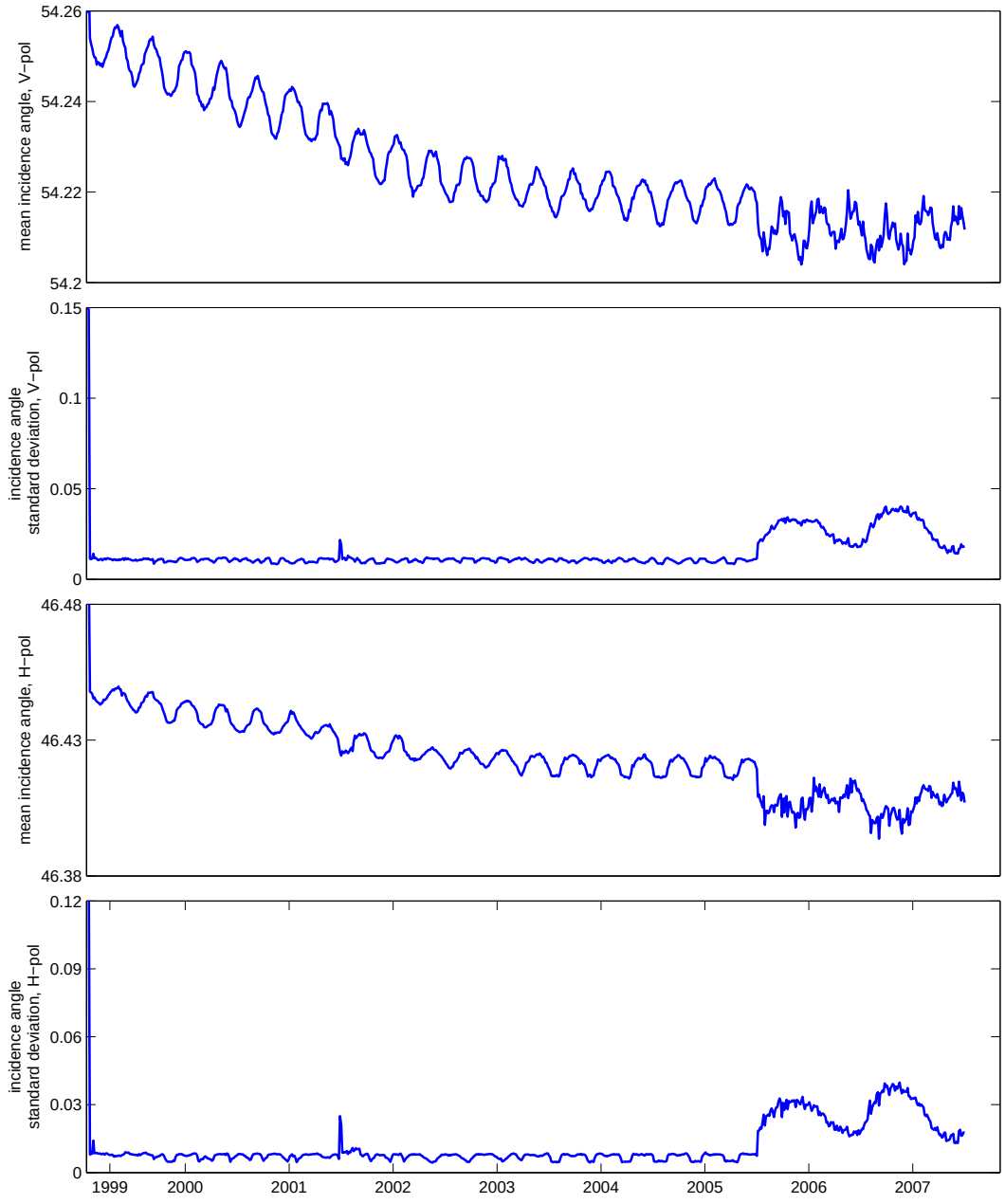

Figure 3.10: Time series of incidence angle statistics at location 1, units in degrees.

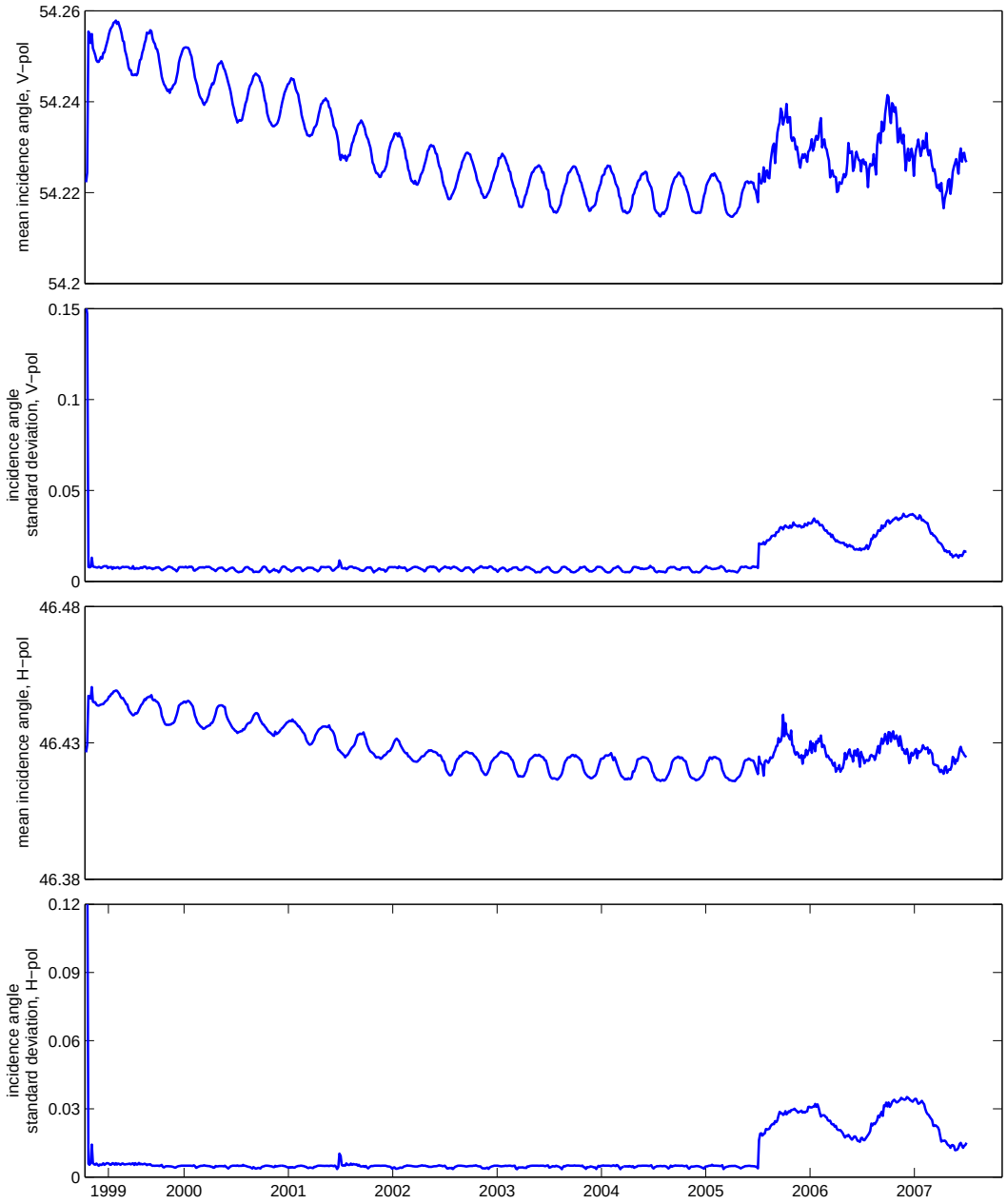

Figure 3.11: Time series of incidence angle statistics at location 2, units in degrees.

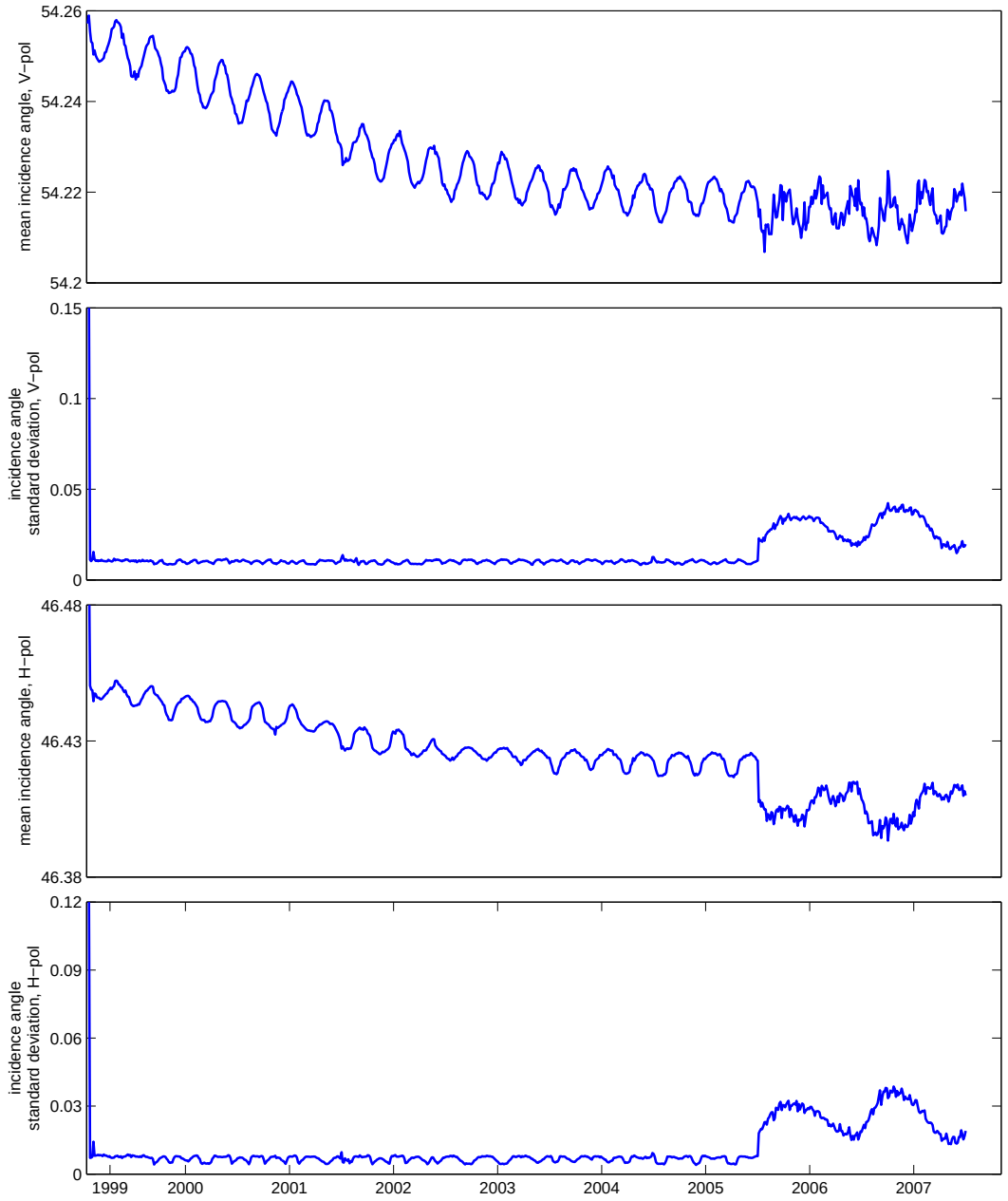

Figure 3.12: Time series of incidence angle statistics at location 3, units in degrees.

3.2.3 Azimuth Angle

Azimuth angle is the second variable quantity of observation geometry that must be considered. To account for the wrap-around problem common to sets of direction data, azimuth mean is computed as

$$\bar{\phi} = \tan^{-1}\left(\frac{\frac{1}{N}\sum_{i=1}^{N}\sin\phi_i}{\frac{1}{N}\sum_{i=1}^{N}\cos\phi_i}\right). \tag{3.1}$$

Standard deviation is somewhat more involved to quantify, and it helps to first define the circular variance,

$$V = 1 - \frac{1}{N}\left(\left(\sum_{i=1}^{N}\cos\phi_i\right)^2 + \left(\sum_{i=1}^{N}\sin\phi_i\right)^2\right)^{1/2}. \tag{3.2}$$

As with typical data sets, V is a measure of centrality, although in the circular case it varies only between $0 \leq V \leq 1$ [24]. Instead of simply defining standard deviation as $\sqrt{V}$, as one would in the linear case, the accepted method has been to follow Mardia [25] and use the transform

$$1 - V = \exp -\frac{1}{2}\sigma^2, \tag{3.3}$$

which yields a standard deviation of

$$\sigma = \left(-2\log\left(1-V\right)\right)^{\frac{1}{2}}. \tag{3.4}$$

The justification for this method is that it seems the most natural mapping of a variance on $(0, 1)$ degrees-squared to $(0, \infty)$ degrees.

Spatial Analysis

Figures 3.13, 3.14, 3.15, and 3.16 show pixel-wise maps and histograms of azimuth angle means and standard deviations for V- and H-pol data sets from 1999 and 2007. Both V- and H-pol mean data sets show a predominate value at 0°, which is expected at high southern latitudes, where the north direction dominates.

A secondary mode also appears at ±180°. The maps suggest most of the pixels with a large mean value are located very far south, where QuikSCAT has limited azimuth diversity.

Standard deviation results are somewhat more difficult to interpret than are the mean results, but the modes of 90° in both H-pol and V-pol data sets suggest that the observations are well dispersed in every direction, and the radial pattern observed in the difference images suggest that what changes there are from 1999 to 2007 are simply due to orbit period mismatch.

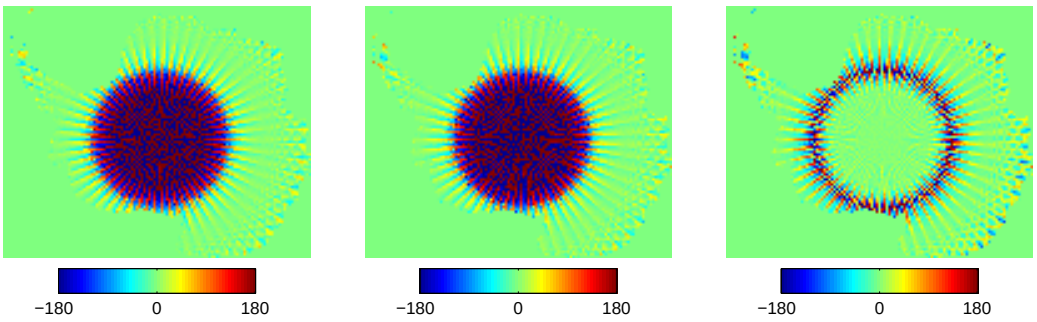

(a) Maps of V-pol mean azimuth angle, in degrees. Left) 1999. Center) 2007. Right) Difference, 2007 - 1999.

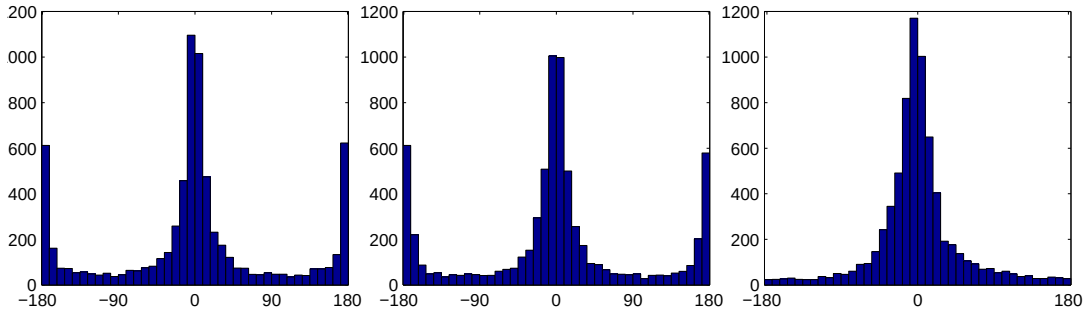

(b) Histograms of V-pol mean azimuth angle, in degrees Left) 1999. Center) 2007. Right) Difference, 2007 - 1999.

Figure 3.13: Mean azimuth angle data, V-pol.

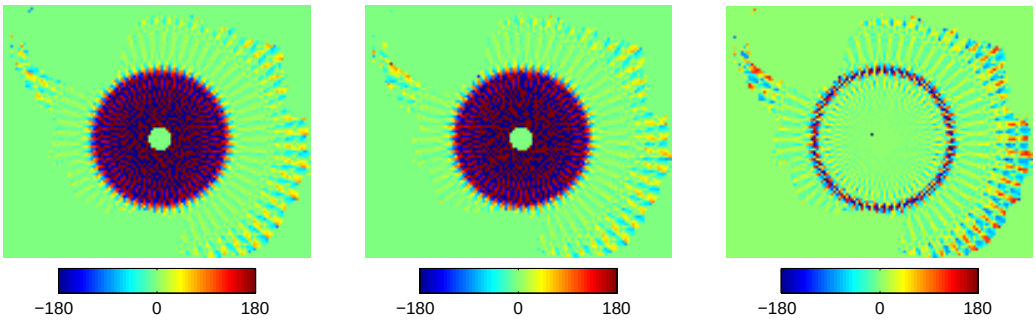

(a) Maps of H-pol mean azimuth angle, in degrees. Left) 1999. Center) 2007. Right) Difference, 2007 - 1999.

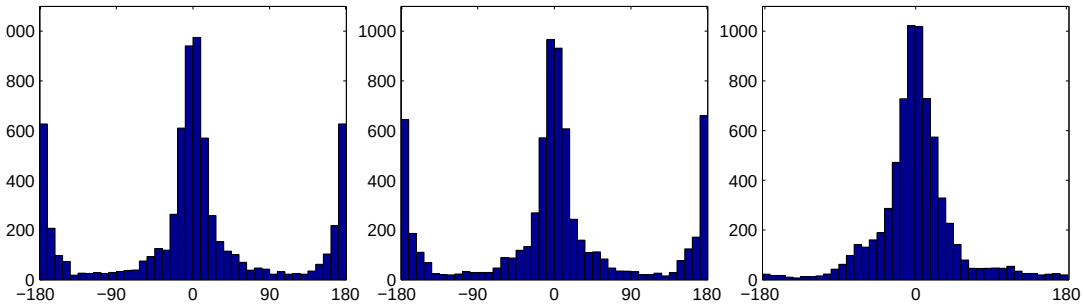

(b) Histograms of H-pol mean azimuth angle, in degrees. Left) 1999. Center) 2007. Right) Difference, 2007 - 1999.

Figure 3.14: Mean azimuth angle data, H-pol.

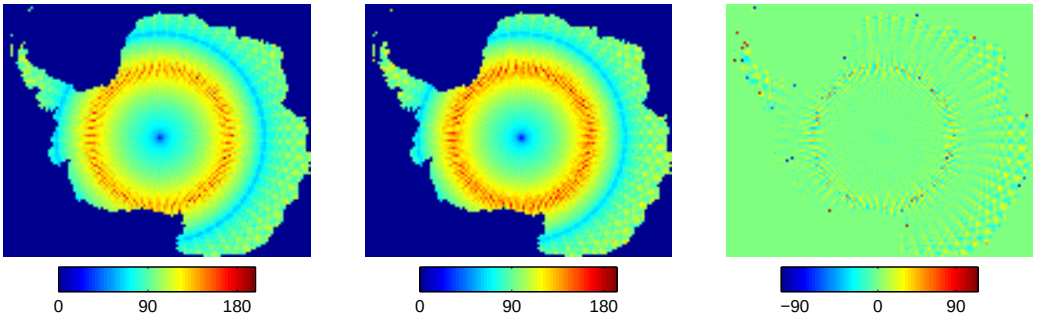

(a) Maps of V-pol azimuth angle standard deviation, in degrees. Left) 1999. Center) 2007. Right) Difference, 2007 - 1999.

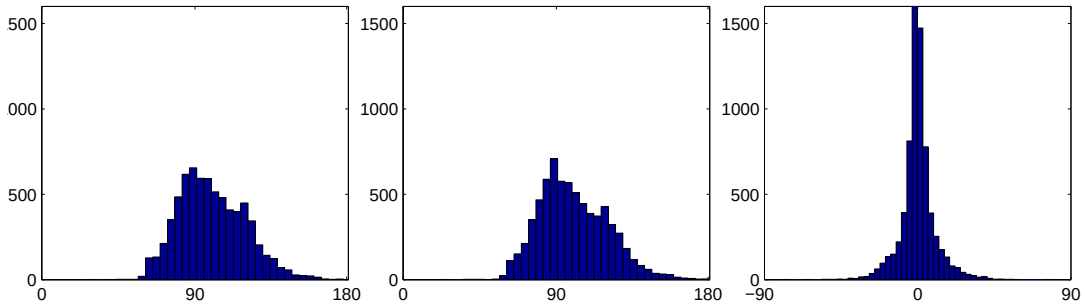

(b) Histograms of V-pol azimuth angle standard deviation, in degrees. Left) 1999. Center) 2007. Right) Difference, 2007 - 1999.

Figure 3.15: Azimuth angle standard deviation data, V-pol.

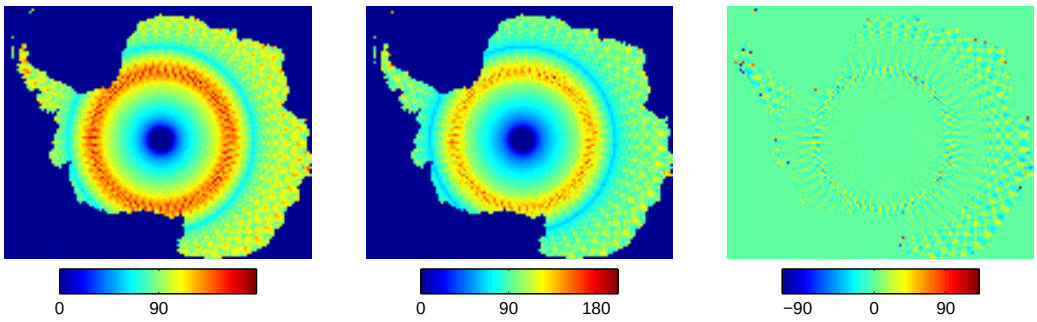

(a) Maps of H-pol azimuth angle standard deviation, in degrees. Left) 1999. Center) 2007. Right) Difference, 2007 - 1999.

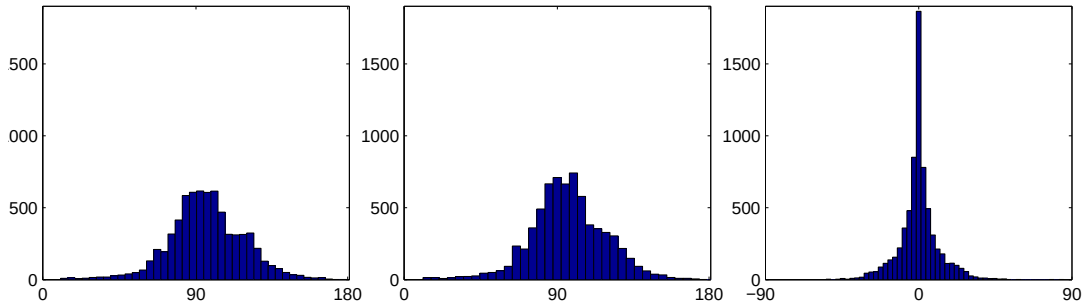

(b) Histograms of H-pol azimuth angle standard deviation, in degrees. Left) 1999. Center) 2007. Right) Difference, 2007 - 1999.

Figure 3.16: Azimuth angle standard deviation data, H-pol.

Temporal Analysis

Figures 3.17, 3.18, and 3.19 show time series data of azimuth angle statistics from the three pixels shown in Table 3.1. Trends from all three locations and both polarizations are similar. All azimuth angle means display an initial period of relative consistency followed by years of a regular, periodically alternating pattern. This pattern corroborates the bi-modal distribution of the histogram of the continent-wide data presented above. Standard deviation data in all three locations shows fair consistency and generally large values, suggesting a generally uniform distribution distorted by the tendency towards north at these latitudes.

The trends from locations 1 and 3 are almost identical, which is unsurprising given their similar latitudes. Both polarizations at these locations show an approximately zero-centered bimodal distribution of azimuth angle mean, and a fairly constant standard deviation. At both locations V-pol data shows a higher standard deviation than H-pol data. This is attributable to V-pol's greater coverage and higher incidence angle. Location 2 also shows a zero-centered bimodal distribution of azimuth angle mean and a fairly constant standard deviation for both polarizations, but with much higher variability in all quantities than at Locations 1 and 2. This variability is attributable to Location 2's extremely southern latitude.

The data presented here demonstrates that in general the azimuth angle of QuikSCAT observations, while highly variable, shows no discernible long-term trends. When combined with the incidence angle results in the previous section, these azimuth angle results permit one to conclude that QuikSCAT has been a stable platform throughout its mission.

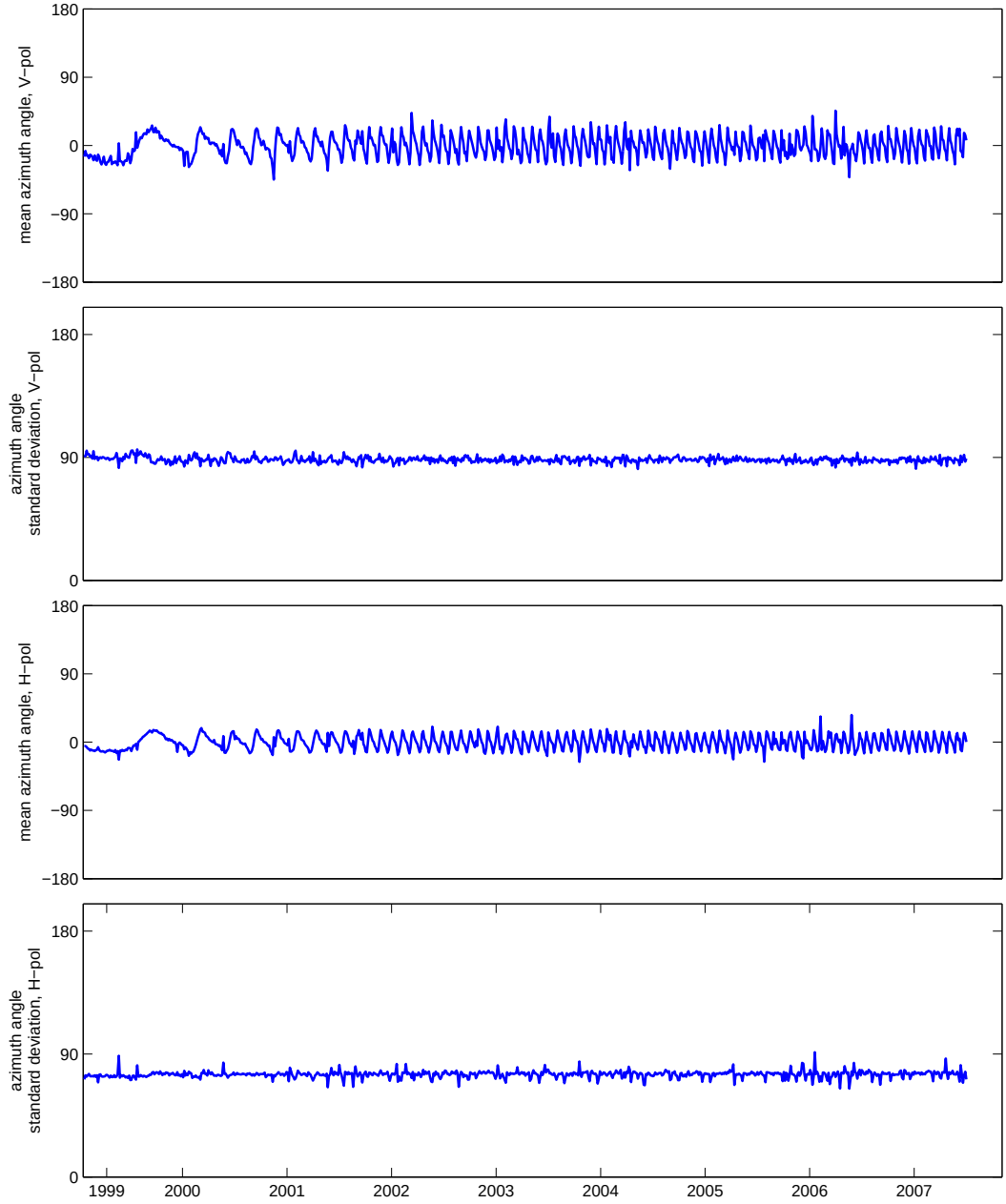

Figure 3.17: Time series of azimuth angle statistics at location 1, units in degrees.

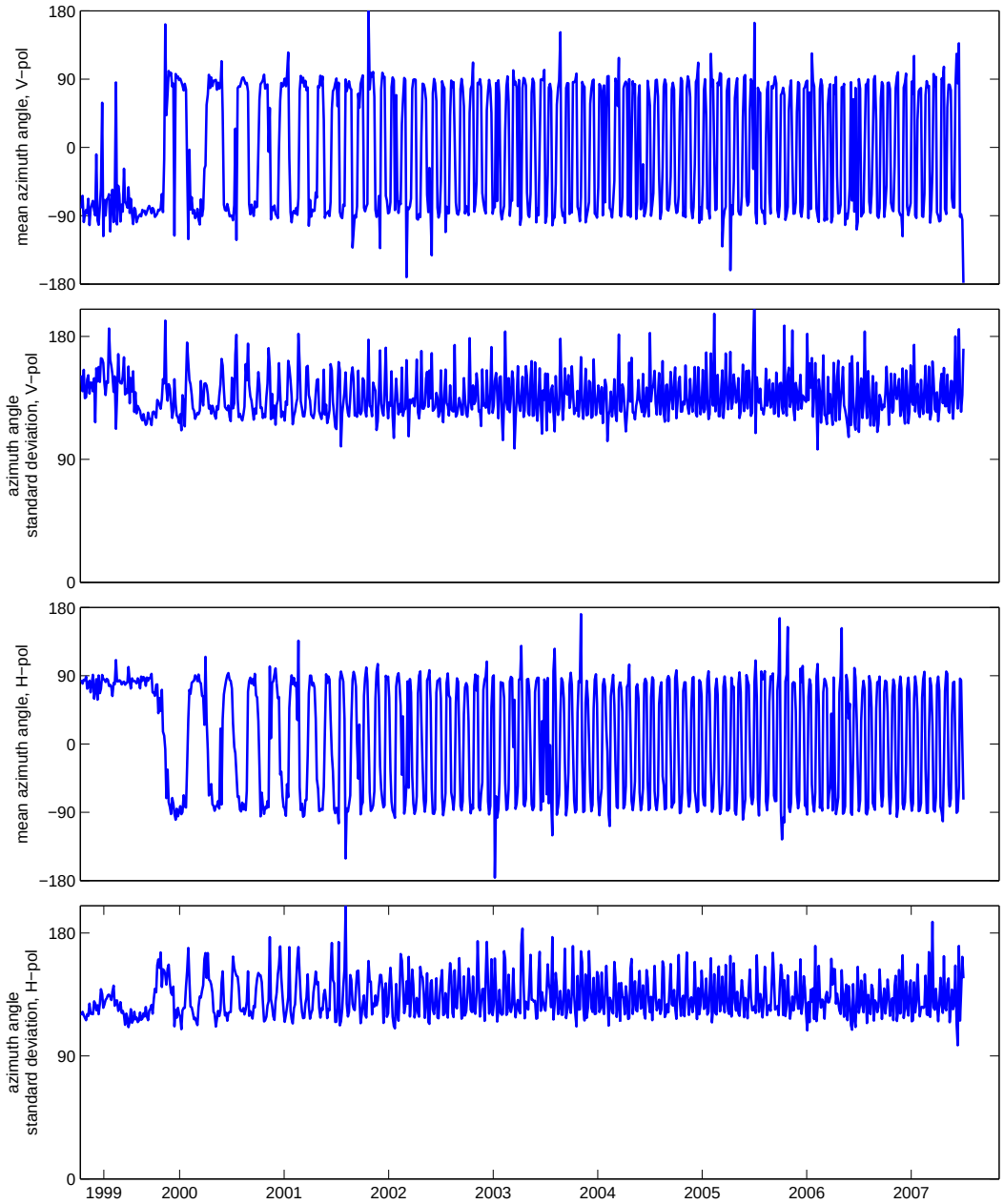

Figure 3.18: Time series of azimuth angle statistics at location 2, units in degrees.

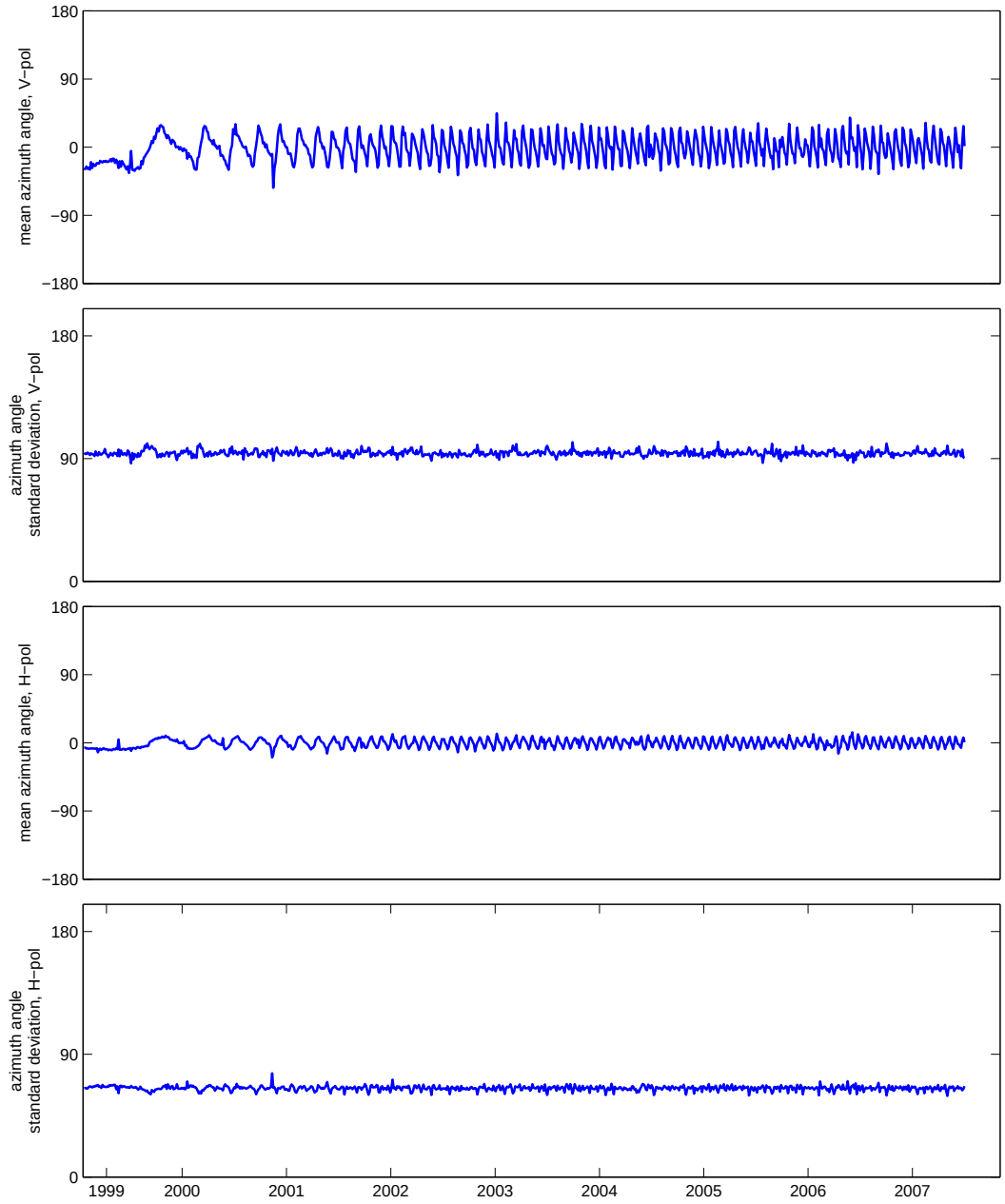

Figure 3.19: Time series of azimuth angle statistics at location 3, units in degrees.

3.3 Backscatter

Having established that QuikSCAT's observation geometry is consistent, I now demonstrate the consistency of QuikSCAT's backscatter observations. Previous backscatter calibration studies have used terrestrial targets such as the Amazon Rain Forest [26], which exhibits diurnal variations, and the Sahara Desert [27], backscatter measurements of which tend to be noisy. Long and Drinkwater [3] demonstrate that the crest of the Antarctic ice divide - where latitude, elevation (see Figure 2.1), and the Antarctic katabatic wind regime [28] contribute to what is perhaps the most predictable weather on Earth - exhibits many desirable qualities of a calibration target. This region does exhibit large seasonal variations in temperature which, despite never causing the firn to melt, does effect its backscatter properties, and must be controlled for. For a further discussion of seasonal variations in backscatter see Chapter 4.

To demonstrate the consistency of QuikSCAT's backscatter measurements I have chosen two climatologically stable locations (locations 1 and 2 in Table 3.1) on the ice sheet crest from which I present air temperature and backscatter data. I use the classical statistical technique of hypothesis testing on regression coefficients to show the magnitude and significance of long term changes in both quantities at both locations. Small or statistically insignificant changes in long term temperature confirm climatological stability, and small or statistically insignificant changes in backscatter suggest instrument stability.

To control for seasonal variations I use a sinusoidal model of the form

$$x = a + bt + c\cos(2\pi t - d), \tag{3.5}$$

where x is the variable of interest (temperature or backscatter), and t is the time index, measured in years. a, b, c, and d are model coefficients representing the mean, slope, magnitude of average seasonal variation, and phase of average seasonal variation of the variable of interest, respectively. Coefficient estimates and variances are solved for in the weighted least squares sense, a more complete discussion of which is found

in Appendix B. The quantity of greatest interest in this case is $\hat{b}$, the estimate of the long term linear change in either temperature or backscatter.

Air temperature data [29] at both locations is shown in Figures 3.20 and 3.21. Since data is unavailable for 1999, 2007, and some isolated periods in between, I have had to extrapolate missing data points from yearly averages. Inspection of the boundaries between extrapolated and reported data, combined with the regular periodicity of the reported data suggest that little precision is lost over the course of the study. The predominate temperature trends are a very large, approximately 45 C, seasonal variation and a slightly increasing long term trend. The magnitude and statistical significance of this linear trend, listed in Table 3.3, show an average annual increase of 0.262 C at location 1 and 0.190 C at location 2, which correspond to overall temperature increases of approximately 2.21 C and 1.61 C over the course of this nearly nine year study. Inspection of the model (Equation 3.5) suggests an adequate fit and description of the underlying data, with the exception of slightly understating the magnitude of seasonal variations.

Scatter plots of QuikSCAT-observed backscatter as a function of temperature at these locations, shown in Figures 3.22 and 3.23, reveal that the large temperature variations at these locations correspond to rather small, less than 0.5 dB, changes in backscatter. It is reasonable to assert that backscatter at these locations is generally insensitive to temperature changes, and that a nine year change of approximately 2 C is negligible for the purposes of the present temporal calibration. Indeed, even if long term temperature increases are understated by 100% - which is highly unlikely - as a result of the necessary temperature data extrapolation, this still corresponds to a change of only approximately -0.02 dB in backscatter, which is so small as to be considered negligible.

I now consider the backscatter from the two calibration locations as a function of time, data for which is shown in Figures 3.24 and 3.25. At both locations and for both V- and H-pol data sets there is a small magnitude, negative trend in average backscatter, and in both locations the V-pol data shows smaller and less significant change than H-pol data. At location 1 the linear trend in both polarizations

is insignificant at the 0.9 level, while at location 2 only V-pol data is statistically insignificant at this level. Thus under the assumption that the backscatter properties of the target location are truly unchanging from year to year and that all change in the backscatter time series is due to changes in QuikSCAT's instrumentation, then the worst-case scenario is that QuikSCAT's H-pol instrumentation has changed by an average of -0.0352 dB/year, or -0.28 dB from 1999 to 2007, and QuikSCAT's V-pol instrumentation has changed by -0.0123 dB/year, or -0.099 dB from 1999 to 2007.

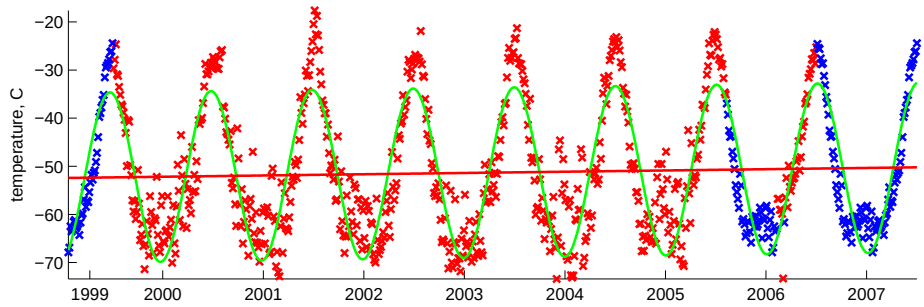

(a) Four-Day mean temperatures at control location 1.

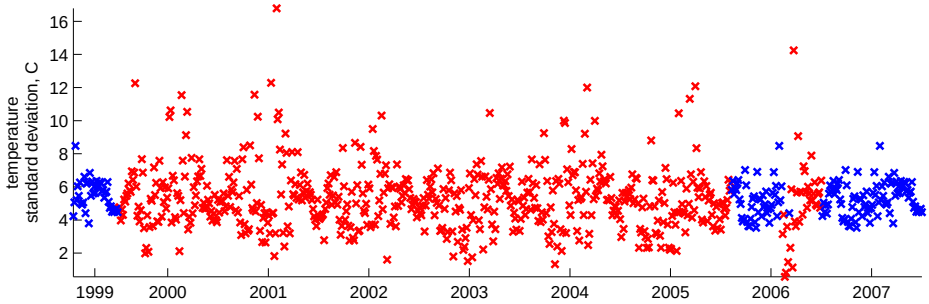

(b) Four-Day temperature standard deviations at control location 1.

Figure 3.20: Air temperature at control location 1. Blue data points represent missing data extrapolated from yearly averages.

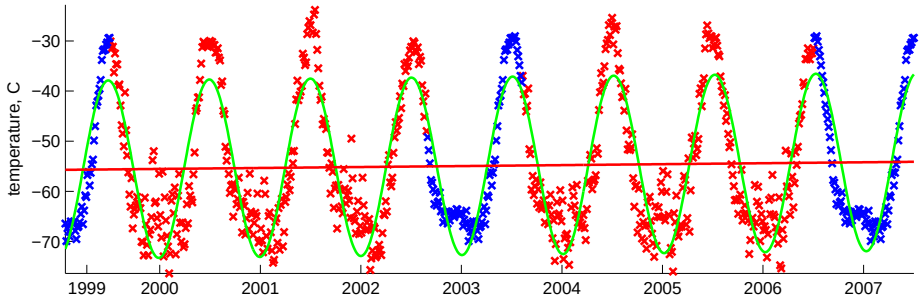

(a) Four-Day mean temperatures at control location 2.

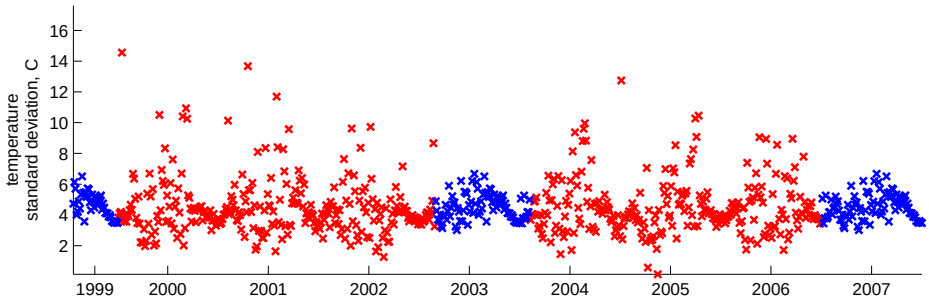

(b) Four-Day temperature standard deviations at control location 2.

Figure 3.21: Air temperature at control location 2. Blue data points represent missing data extrapolated from yearly averages.

Table 3.3: Model coefficients and indicators of significance.

Temperature				
	$\hat{b}$ C/year	var($\hat{b}$) (C/year)^2	Z_b	p_b
Location 1	.262	1.29e-07	8.01	1.0
Location 2	.190	1.08e-07	6.35	1.0

Backscatter				
	$\hat{b}$ dB/year	var($\hat{b}$) (dB/year)^2	Z_b	p_b
Location 1, V-pol	-0.0036	1.40e-08	-0.33	0.26
Location 1, H-pol	-0.0123	1.52e-08	-1.09	0.73
Location 2, V-pol	-0.0051	1.40e-08	-0.47	0.36
Location 2, H-pol	-0.0352	1.52e-08	-3.14	0.99

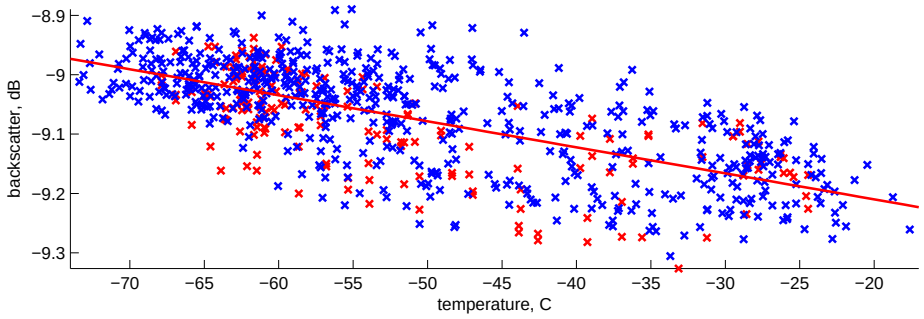

(a) Temperature vs backscatter, control location 1, V-pol. Slope of trend line = -0.0044 dB per degree.

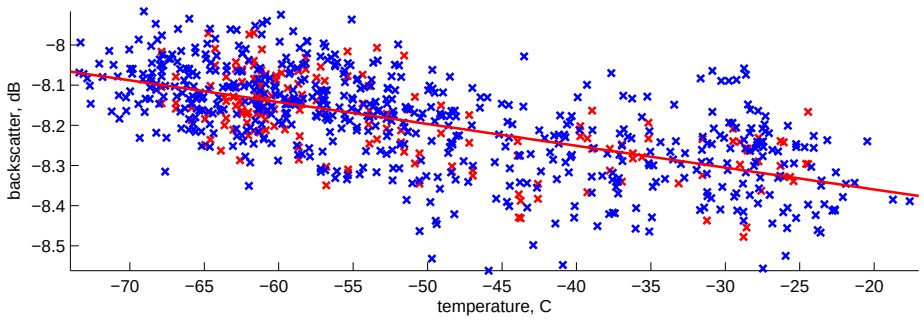

(b) Temperature vs backscatter, control location 1, H-pol. Slope of trend line = -0.0054 dB per degree.

Figure 3.22: Temperature vs backscatter, control location 1. Blue data points represent missing data extrapolated from yearly averages.

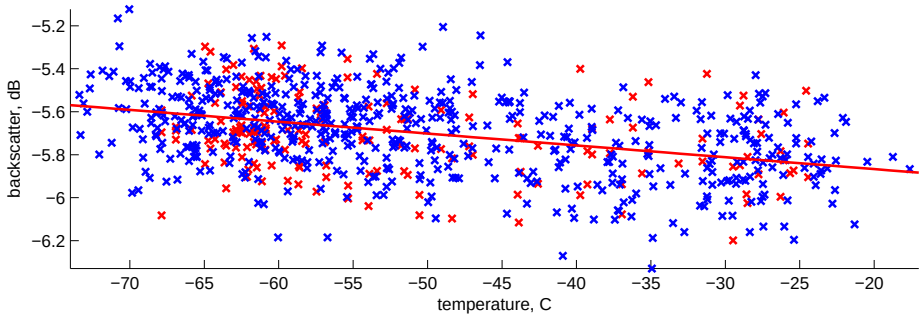

(a) Temperature vs backscatter, control location 2, V-pol. Slope of trend line = -0.0057 dB per degree.

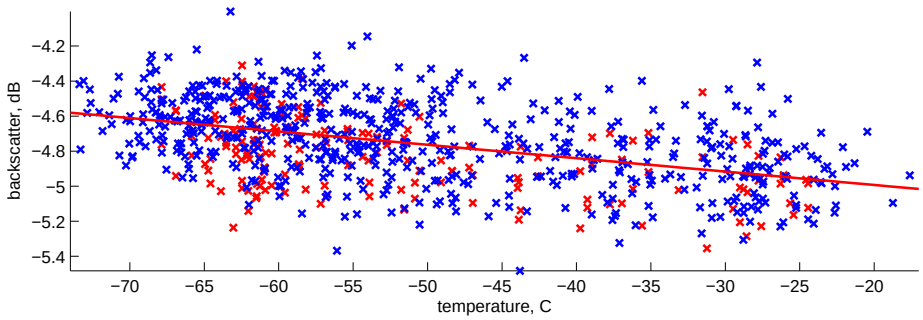

(b) Temperature vs backscatter, control location 2, H-pol. Slope of trend line = -0.0081 dB per degree.

Figure 3.23: Temperature vs backscatter, control location 2. Blue data points represent missing data extrapolated from yearly averages.

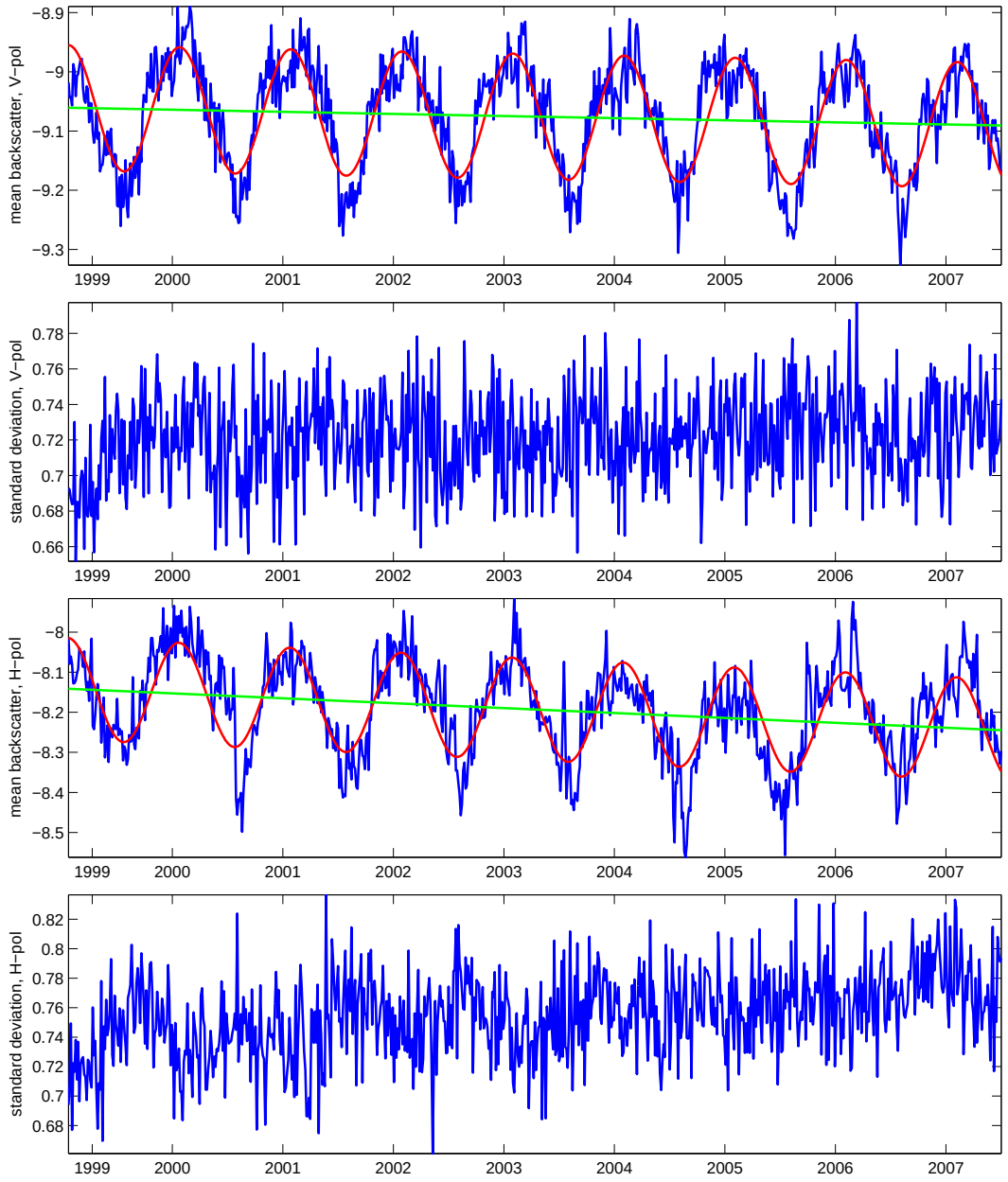

Figure 3.24: Backscatter time series data at control location 1. From top to bottom) V-pol mean backscatter, V-pol backscatter standard deviation, H-pol mean backscatter, H-pol backscatter standard deviation.

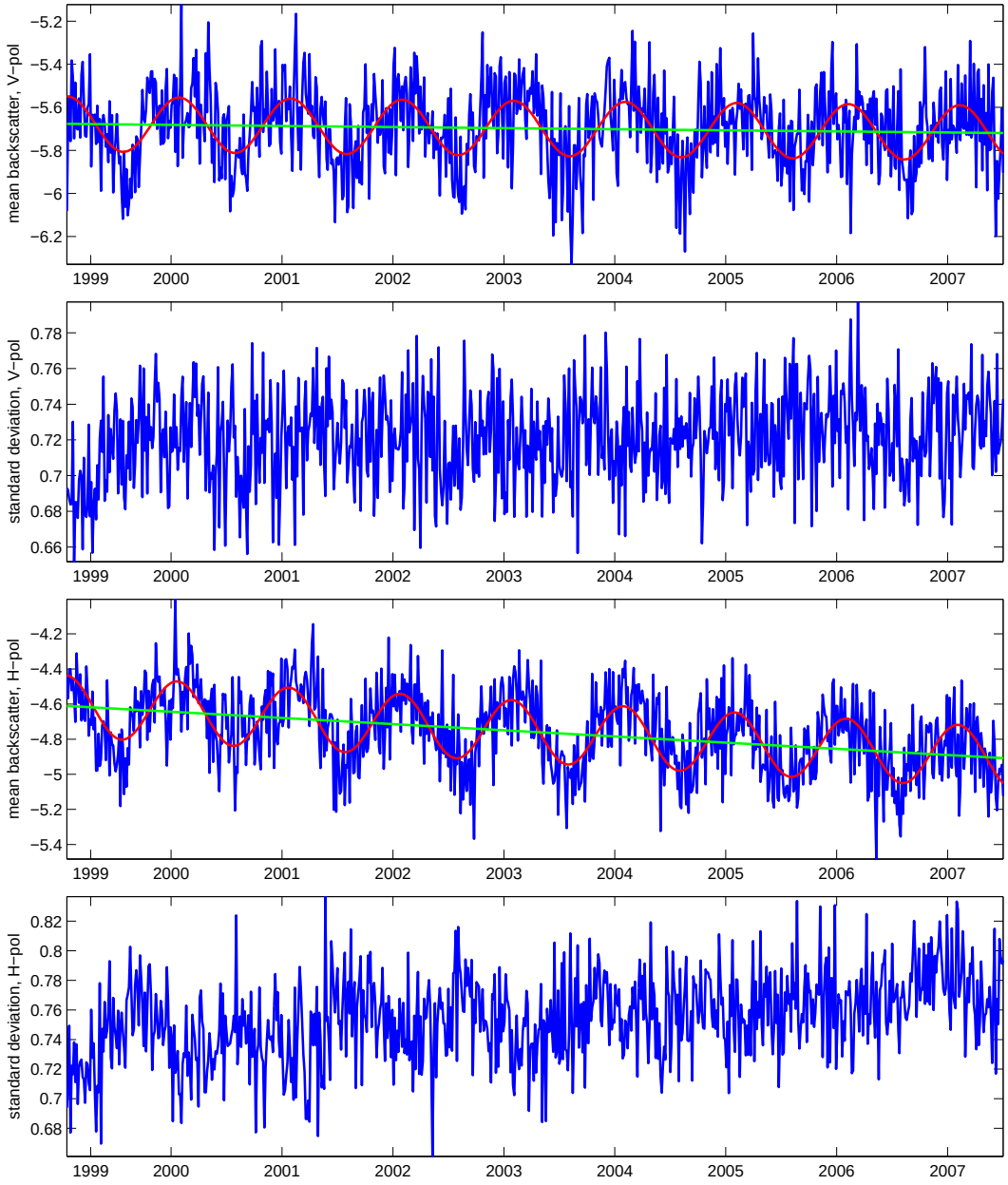

Figure 3.25: Backscatter time series data at control location 2. From top to bottom) V-pol mean backscatter, V-pol backscatter standard deviation, H-pol mean backscatter, H-pol backscatter standard deviation.

To ensure that the two calibration locations are not anomalous bastions of apparent stability I perform the preceding analysis for each pixel in the entire continent, pixel-wise values and variances of $\hat{b}$ are shown in Figure 3.26. These maps show that over most of the continent H-pol data has undergone larger and more significant change than has V-pol data. The crest region of the Antarctic ice sheet shows the smallest and least significant change at both polarizations of any Antarctic region. Since this is the region that one would expect, for glaciological and geophysical reasons, to change least, and does indeed show the smallest change, it is reasonable to conclude that what change is observed in the rest of the continent - where one would expect to find a dynamic backscatter signature for reasons discussed in Chapter 4 - is due primarily to changing backscatter mechanisms, and not to changing instrumentation.

Furthermore inspection of the maps reveals that location 2 is somewhat to the interior of the region of smallest change and although the temperature there has been shown to be stable, it is possible that there are other, subtle, geophysical forces at work there causing the observed change in backscatter. In any case changes in QuikSCAT's backscatter instrumentation are likely much smaller than the worst-case scenario presented above.

3.4 Summary

This nine year survey of important parameters from QuikSCAT verifies its consistency as a remote sensing instrument. Observation geometry parameters are shown to be exceptionally stable from 1999 to 2007, and, although the lack of an ideal ground target somewhat limits the verification of QuikSCAT's instrumentation, an acceptable worst-case bound of -0.03 dB/year in instrumentation drift is established, although actual backscatter precision is likely much better. In general, the large scale, long-term changes in backscatter presented in the following chapter can be assumed to result from changes in the observed, not the observer.

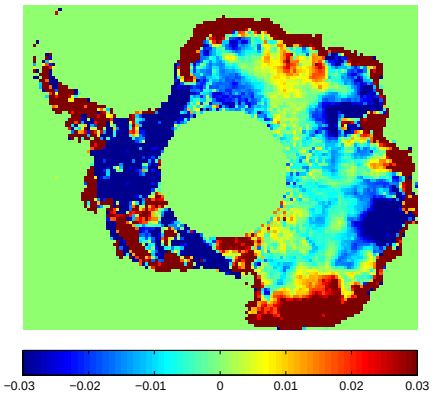

(a) Pixelwise estimates of interannual change in average backscatter, $\hat{b}$, V-pol.

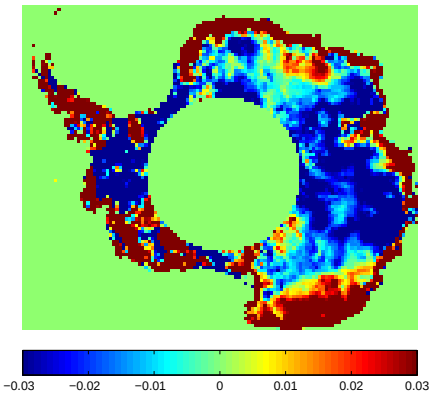

(b) Pixelwise estimates of interannual change in average backscatter, $\hat{b}$, H-pol.

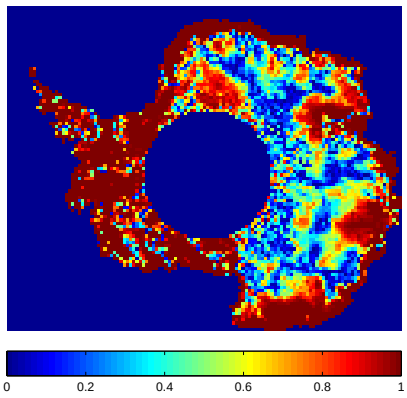

(c) Pixelwise significance levels of $\hat{b}$, V-pol

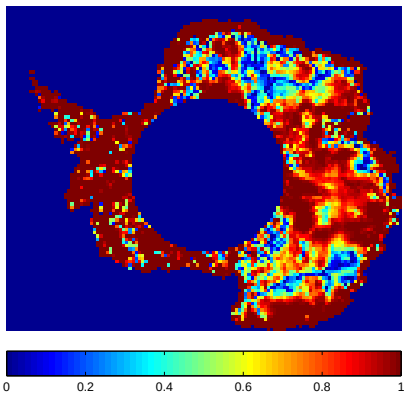

(d) Pixelwise significance levels of $\hat{b}$, H-pol

Figure 3.26: Estimates and significance levels of linear changes in backscatter. To emphasize small changes in $\hat{b}$, the color scale in sub-figures (a) and (b) is chosen such that all but the smallest values saturate.

Chapter 4

Seasonal and Interannual Variations

The previous chapter has established that QuikSCAT observations from any time since its launch in 1999 can be directly compared. In this chapter I consider how the backscatter signature from various locations on the Antarctic ice sheet has changed since 1999. I begin with a brief discussion of simple scattering models for snow and ice, and then consider pixelwise maps. Finally I present time series data of some backscatter signature parameters.

4.1 Backscatter Signature

Many studies of backscatter from snow and ice have used an empirical backscatter signature model of the form

$$\sigma^0(\theta,\phi) = A + \sum_{i\in\mathcal{G}} B_i(\theta-\theta_0)^i + \sum_{j\in\mathcal{F}} C_j(\theta)(j\phi-\phi_j). \tag{4.1}$$

Where σ^0 is normalized backscatter cross section, in dB, as is customary, θ is incidence angle, ϕ is azimuth angle, and θ_0 is a reference incidence angle. This model borrows from ocean scattering theory and nicely summarizes the dependence of backscatter on observation geometry. $\mathcal{F}$ has previously been given as $\mathcal{F}=\{2\}$ [30], $\mathcal{F}=\{1,2\}$ [3], and $\mathcal{F}=\{1,2,3,4\}$ [7, 31]. $\mathcal{G}$ is usually given as $\mathcal{G}=\{1\}$ or $\mathcal{G}=\{1,2\}$ [32].

A gives a measure of the total backscatter at the reference incidence angle. In general this quantity can be thought of as the superposition of rough surface scattering and volume scattering from within the snow pack at the reference incidence angle. The ratio of surface to volume backscatter is related to B_i. As mentioned previously, B_1 tends to be on the order of -0.2 dB per degree from snow and ice. A steeper slope (more negative B_1) generally suggests scattering from a rougher surface than a less

steep slope (less negative B_1). C_j and ϕ_j are related to the size and orientation of azimuthally anisotropic scatterers. Antarctic examples of such scatterers are wind-formed erosional features, such as sastrugi, and depositional features, such as dunes.

Since QuikSCAT has an essentially fixed incidence angle for each beam, I let $B_i = 0$, and $C_j(\theta) = C_j$, a constant. The utility of using a fourth order azimuth modulation model, that is letting $\mathcal{F} = \{1, 2, 3, 4\}$ was first shown in [7], and to take advantage of QuikSCAT's dense azimuth sampling I follow that approach here. I apply this model to each data bin, solving for a total of nine model parameters, A, C_j, and ϕ_j for $j = 1, 2, 3, 4$ in the least squares sense. To smooth high frequency fluctuations I first average data into one degree azimuth bins. An example V-pol data bin (a single pixel at 71.0 degrees south latitude and 120 degrees east longitude in East Antarctica from days 109 through 112, 2005) and its model fit are shown in Figure 4.1. The behavior of this bin is typical, and similar behavior has been previously noted in both ocean and snow backscatter [33, 3].

In addition to the nine model parameters that are directly solved for there are three secondary quantities of interest: the direction of maximum backscatter (denoted W_{max}), the direction of minimum backscatter (denoted W_{min}), and the overall size of the backscatter modulation (denoted M). These three parameters are defined as the azimuth angle where the model achieves its maximum value, the azimuth angle where the model achieves its minimum value, and the difference between the model maximum and minimum values, respectively. This yields a total of 12 backscatter signature parameters for each polarization in each data bin. The values of these 12 parameters for the example V-pol data bin are shown in Table 4.1.

Maps of all 12 parameters for an arbitrarily chosen four day period (days 109 - 112, 2005) illustrating typical spatial distributions, are shown in Figure 4.2. Note that in these maps the circle absent of data around the pole is due to insufficiently diverse observation geometry to support the empirical model. These plots reveal many interesting geographic features. For the following discussion of general backscatter signature from various Antarctic regions I divide the continent as shown in Figure 4.3. The most important backscatter signature parameters, and hence the ones upon

Table 4.1: Values of 12 backscatter signature parameters for a single bin.

	Value	Units
A	-19.024	dB
C_1	0.936	dB
C_2	2.506	dB
C_3	0.480	dB
C_4	1.116	dB
ϕ_1	-39.754	deg
ϕ_2	68.591	deg
ϕ_3	1.991	deg
ϕ_4	126.918	deg
W_{max}	28	deg
W_{min}	155	deg
M	6.92	dB

which I focus this analysis, are generally the even (which correspond to the real, or cosine portion of a Fourier series) terms. The discussion also focuses on V-pol data, as large scale scattering effects are very similar for both polarizations.

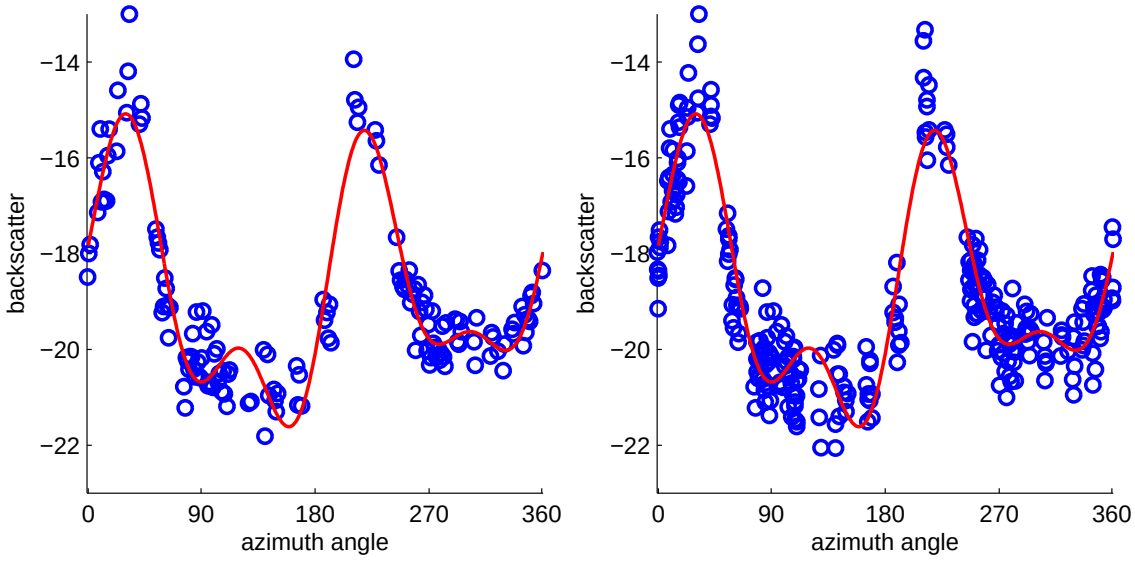

Figure 4.1: Examples of data from one bin (71 degrees south latitude, 120 degrees east longitude, days 109 through 112, 2005) with superimposed model. Left) Data averaged over 1° wide azimuth angle bins. Right) Raw data.

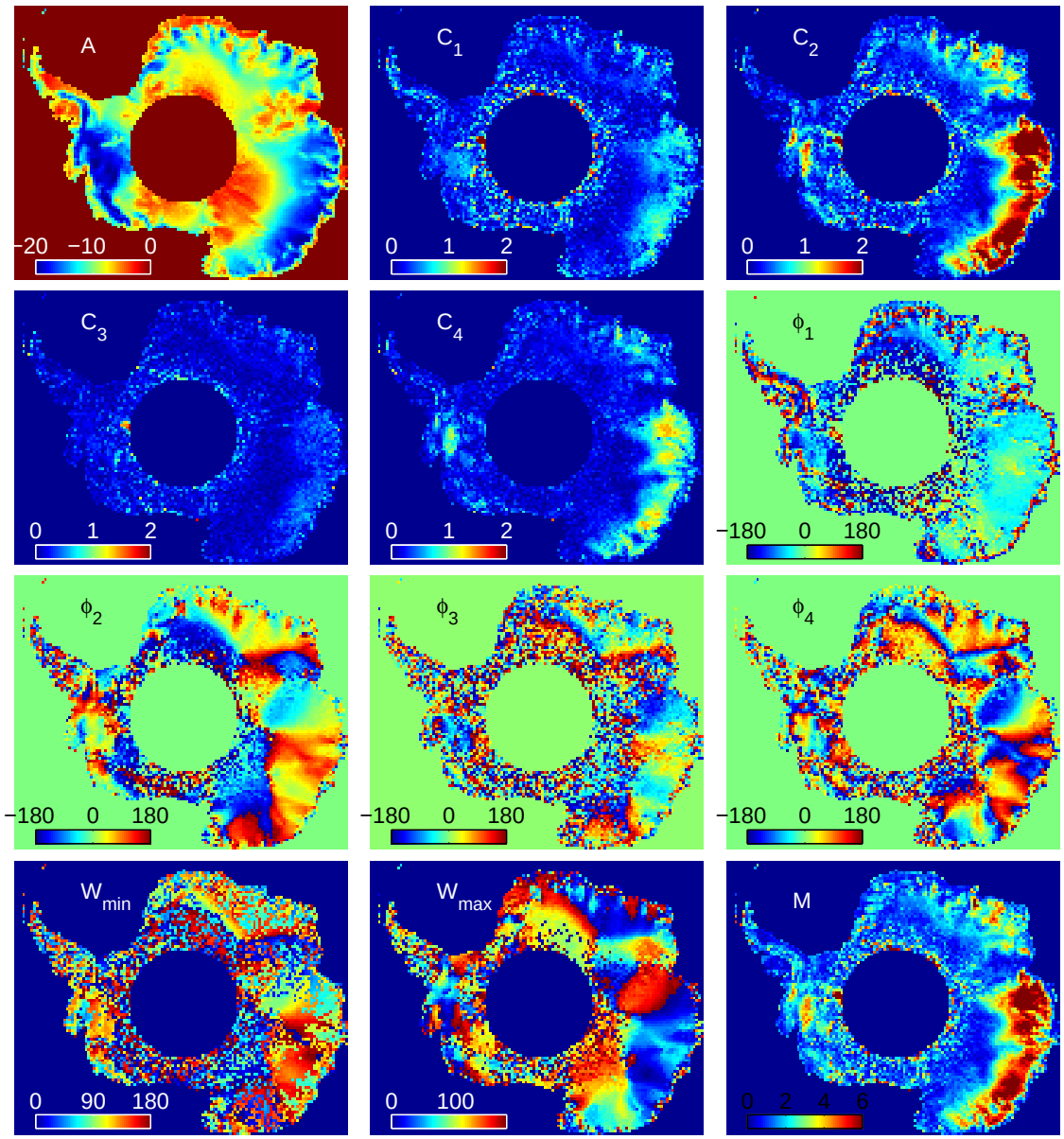

Figure 4.2: Maps of the 12 backscatter signature parameters listed in Table 4.1 for every pixel during a single four day period during the 2005 austral summer. Plots in this Figure are for V-pol; H-pol data looks similar.

4.1.1 East Antarctic Plateau

The ice sheet plateau is characterized by fairly bright, approximately -12 dB, average V-pol backscatter and very little azimuth modulation. At the center of the plateau lies the ice sheet crest, which is clearly demarcated as a boundary between positive and negative values in the second and fourth order azimuth modulation phase (ϕ_2, ϕ_4) and in the direction of maximum backscatter (W_{max}).

4.1.2 Wilkes Land

The East Antarctic region is characterized by relatively low average V-pol backscatter (A) values but exceptionally large azimuth modulation magnitude values. Typical V-pol values of second order azimuth modulation magnitude (C_2) in this region are 1.5 to 2.5 dB, with a maximum value of nearly 4 dB achieved in isolated regions. Fourth order azimuth modulation magnitude (C_4) also attains its highest values, greater than 1 dB, in this region. Typical V-pol overall modulation values in this region are approximately 5 dB, with a maximum value of nearly 10 dB observed for individual pixels. Inspection of the azimuth modulation phase terms shows extremely large regions of spatial coherence and low noise, even for the fourth order term.

These fourth order observations are possibly the result of superposition of continental scale elevation gradient, which effects the local incidence angle, and sastrugi. Previous studies [3], [30] were limited to second order observation due to the limited azimuthal diversity of SASS, ERS-1/2, and NSCAT. However with QuikSCAT we are able to observe surprising spatial coherence in fourth order magnitude terms as well, suggesting the complexity and symmetry of the ice sheet. Preliminary research shows that increasing the model order beyond four contributes little.

This large azimuth angle modulation is thought to be caused by sastrugi, erosional features of meter scale which are carved into the ice sheet by the Antarctic katabatic wind regime. Over much of Antarctica air is forced along specific drainage paths as it cools and flows down from the continent's interior through confluence zones nearer the coasts [34]. This consistent and intense airflow increases surface roughness

in the cross-wind direction, which results in a strongly second order anisotropic radar response. Thus the strongest backscatter is generally observed in the "across" sastrugi directions and the weakest backscatter is generally observed in the "up/down" directions. This bi-directional anisotropicity introduces a $\pm 180^\circ$ ambiguity into many directional quantities observed over regions were sastrugi is a prominent scatterer. An example of such an ambiguity can be seen in Figure 4.1, where the model had two nearly identical local maxima. Sastrugi is considered a surface scattering mechanism, although the actual backscatter likely includes effects from buried layers as well.

4.1.3 Megadune Region

Perhaps the most interesting region of Antarctica is the 500,000 km^2 area in East-Antarctica characterized by the presence of large-scale periodic snow pack features known as megadunes. (A smaller dune field is also found in southern Queen Maud Land.) Megadunes are large, highly regular surface ripples with 2-4 m amplitude, 3-5 km period, and up to hundreds of kilometers in extension. Additional features of this region include large-grained, glazed firn on the leeward faces of the dunes, and what is termed "severe sastrugi" at the base of the windward faces of the dunes [35]. An large-scale optical image of a portion of the megadune region is shown in Figure 4.4.

Typical backscatter signature from the megadunes is very bright, perhaps the brightest Ku-band terrestrial target. Figure 5.12 shows that for NSCAT data observed in 1997 the megadune region's backscatter is less sensitive to incidence angle than that in many other regions, suggesting that volume scattering, such as from larger-than-typical grain sizes [36], are the likely cause of this brightness. Unwrapping the precise scattering mechanisms of the megadune region is particularly challenging due to the unique topographic combination of erosional and depositional features found there.

4.1.4 Amery Ice Shelf

The backscatter signature from the Amery Ice Shelf is different than surrounding areas for almost every backscatter parameter. In the average backscatter (A) image it appears very bright, as are the glaciers that feed it. It is also noticeable as the region of smallest azimuthal modulation magnitude for all orders. The azimuth modulation phase parameters are also somewhat noisier than those of surrounding regions. It is postulated that wind direction is less consistent and wind intensity less severe at the Amery Ice Shelf than in other coastal regions. This wind regime, combined with regular severe melt events results in a backscatter dominated by bright volume scatterers, which accounts for the large average backscatter and low azimuth modulation.

4.1.5 Confluence Zones

The confluence zones appear strongly textured in many of the images. The portions nearest the coast have very high average backscatter values, likely caused by large (relative to grain size) ice pipes and lenses that result from the melt/refreeze cycle. This also results in little azimuth modulation. Interior to this bright band, but exterior to the higher portions of the ice sheet plateau, there is a band of alternating azimuth modulation magnitude and phase values. These strong textures are likely the result of topography and surface/air-stream interaction that produce sastrugi-like features. These scattering mechanisms are not completely understood.

4.1.6 West Antarctica

The West Antarctic portion of the ice sheet has been the subject of much study lately due to concerns of a possible collapse and the accompanying $\sim$5 m rise in ocean level [37], [38]. The V-pol backscatter signature over West Antarctica is characterized by low average backscatter values. NSCAT data observed in 1997, shown in Figure 5.12, shows that West Antarctica has a very strong, approximately -0.3 dB per degree, dependence of backscatter on incidence angle, suggesting that in this region there is a higher contribution of surface to volume scattering relative to other areas. West

Antarctica had a highly varied, generally mountainous, geography, which influences the snow surface and disrupts the continental-scale katabatic winds that prevail in East Antarctica. Thus there is much less observed azimuthal modulation in this region relative to others.

4.1.7 Antarctic Peninsula

The Antarctic peninsula's relatively small size, patchwork of ice shelves, ice sheets from various snow zones, and its exposed, rocky summertime terrain make its backscatter signature very different from the rest of Antarctica, and beyond the scope of this thesis. The V-pol backscatter signature seen here consists of a thin filament of low average backscatter surrounded by extremely high backscatter values. The boundary between these two portions of the Antarctic peninsula likely corresponds to the dry snow line. The first order azimuth modulation phase term shows surprising, and possibly aberrational, spatial coherence. Long and Drinkwater [3] suggest continental-scale slope as the geophysical mechanism primarily responsible for first order azimuth modulation: however this seems unlikely for the Antarctic Peninsula's highly variable topography. There is possibly some other, as yet unknown, source for this surprising backscatter signature.

4.1.8 Ross and Ronne Ice Shelves

The Ross and Ronne ice shelves are the largest permanent ice shelves in Antarctica, and exhibit similar backscatter signatures. Unlike the Amery ice shelf these regions are characterized by uninteresting average backscatter, very small azimuth modulation magnitude terms, and extremely noisy azimuth modulation phase terms. Although the interior portion of the Ross Ice Shelf is surprisingly bright, probably due to buried ice lenses from infrequent melt events.

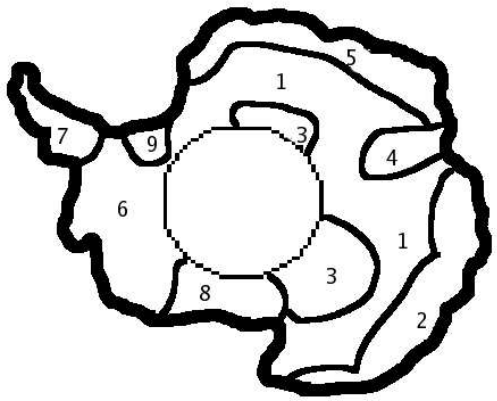

Figure 4.3: Definitions of various Antarctic regions. 1) East Antarctic plateau. 2) Wilkes land. 3) Megadune regions. 4) Amery Ice Shelf. 5) Confluence zones. 6) West Antarctica. 7) Antarctic peninsula. 8) Ross ice shelf. 9) Ronne Ice Shelf. These region definitions are very approximate. The region around the pole is left undefined.

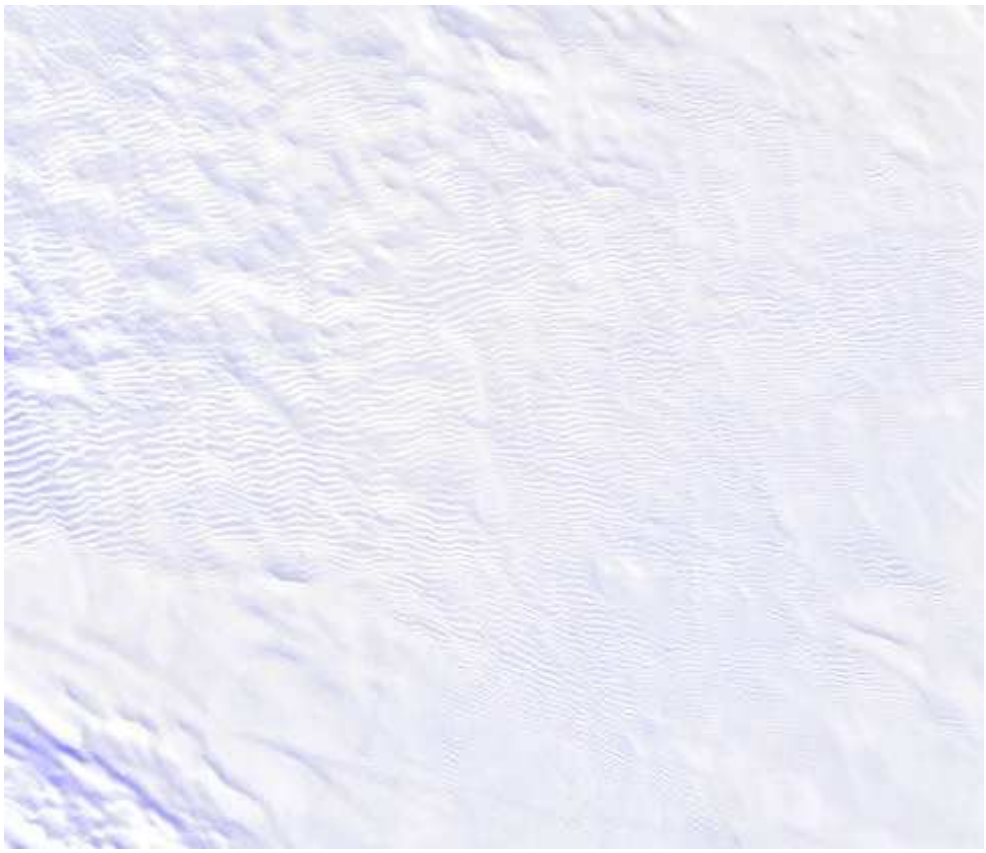

Figure 4.4: Optical image of the megadune region [39].

4.2 Seasonal and Interannual Model

To model how these backscatter signature parameters change seasonally and interannually I adopt a model that describes the superposition of a linear, long-term trend and sinusoidal seasonal variations,

$$x = a + bt + c\cos(2\pi t - d), \tag{4.2}$$

where x is any of the backscatter signature parameters, t is the time index, in years, and a, b, c, d describe the parameter's variation with time. In the previous chapter only the estimate of b was of interest. Here I consider b and c, as both are important to quantify change in the ice sheet's backscatter properties. For the remainder of this chapter I adopt the notational convention where A_b indicates the long term linear change in A, or the value b takes when the model is applied to average backscatter (that is, when $x = A$). $C_{2,c}$ then indicates the seasonal variation in C_2, or the values c takes when $x = C_2$, and so on. Further subscripts indicate polarization.

4.2.1 Magnitude Quantities

The most interesting backscatter signature parameters is A_b, the long term trend in average backscatter. A pixelwise map of this quantity is displayed in Figure 3.26, with the color scale purposefully narrowed to emphasize regions of small change, most of which are concentrated along the ice sheet crest. That map is repeated here, Figure 4.5, with a more informative color scale, also included are maps of A_c, $C_{2,b}$, and $C_{2,c}$, for both V- and H-pol.

Inspection of these maps reveals several trends in the spatial distribution of the change parameters associated with backscatter parameters A and C_2. Maps of A_b show regions of both large positive and negative change. The largest negative change appears in Elsworth Land in West Antarctica, while much of the coast shows a large positive trend. The region of largest positive trend appears near the margin of the Ross Ice Shelf.

Maps of A_c show a fairly sharp boundary between regions with significant seasonal change and regions with little. This boundary is likely coincident with the

dry snow line, as the presence of liquid water greatly decreases the backscatter from otherwise dry snow, resulting in seasonal variations of as much as 20 dB, peak to trough, in some locations. Most of the continent shows much less than 0.5 dB of seasonal variation in average backscatter. One noticeable region of seasonal variation in second order azimuth modulation ($C_{2,c}$) is on the boundary of the Ross Ice Shelf. This observation, combined with the strongly increasing linear trend in average backscatter at an adjacent location suggests that the nature of the Ross ice shelf and nearby regions is changing. Severe geophysical changes, including melt events, in this region have been observed and previously reported [40].

Maps of $C_{2,b}$ show that in general second order azimuth modulation has changed very little since 1999, although what change does appear is concentrated along the coasts. Maps of $C_{2,c}$ show that there is some spatially coherent seasonal change in second order azimuth modulation, although this change too is very small.

4.2.2 Directional Quantities

As discussed above, azimuthal anisotropy of the backscatter signature from much of Antarctica is strongly second order, which introduces a $\pm 180^\circ$ ambiguity into many directional quantities. This ambiguity makes the empirical model (Equation 4.2) used to describe seasonal and interannual variations in magnitude quantities inadequate for describing the same changes in directional quantities. So, I resort to the more primitive technique of observing the differences in same-season maps of second and fourth order azimuth modulation phase (ϕ_2 and ϕ_4) from 1999 to 2007. These maps are shown in Figure 4.6 and 4.7 for data from days 213 through 216 (chosen arbitrarily) of each year. The difference images show very little change, except for some "salt and pepper" noise along the ice sheet crest and along the Lambert (no relation) Glacier. There is a spatially coherent phase change in West Antarctica, which is surprising given the small azimuth modulation magnitudes observed there.

In general the azimuth modulation phase parameters remain remarkably similar in both study periods. Given the strong second order nature of the backscatter and its associated ambiguities, the lack of noise in the phase and phase difference images

over the whole of East Antarctica is startling. This suggests that the katabatic wind regime is perhaps more consistent and more important to scattering than previously believed. The noise observed in the second order difference images is along the ice sheet crest, where wind direction tends to be less consistent and the wind speed is smaller, thus producing weaker surface scatterers. The fourth order phase and phase difference images also reveal remarkable consistency, with significant noise observed only along the ice sheet crest, over the Amery Ice Shelf, and, unlike the second order case, in the megadune fields, which suggests the wind regime in the megadune region may be changing more rapidly and independently of the wind regime in the remainder of East Antarctica.

Given that the directional quantities from 1999 and 2007 appear so similar, it is unlikely that that neglecting seasonal or single-year changes is detrimental to understanding the dynamics of the ice sheet. Because some directional quantity estimates require more azimuth diversity than magnitude quantities, there is more noise apparent at the southernmost reported latitudes in the phase images (Figures 4.6 and 4.7) than in the magnitude images (Figure 4.5).

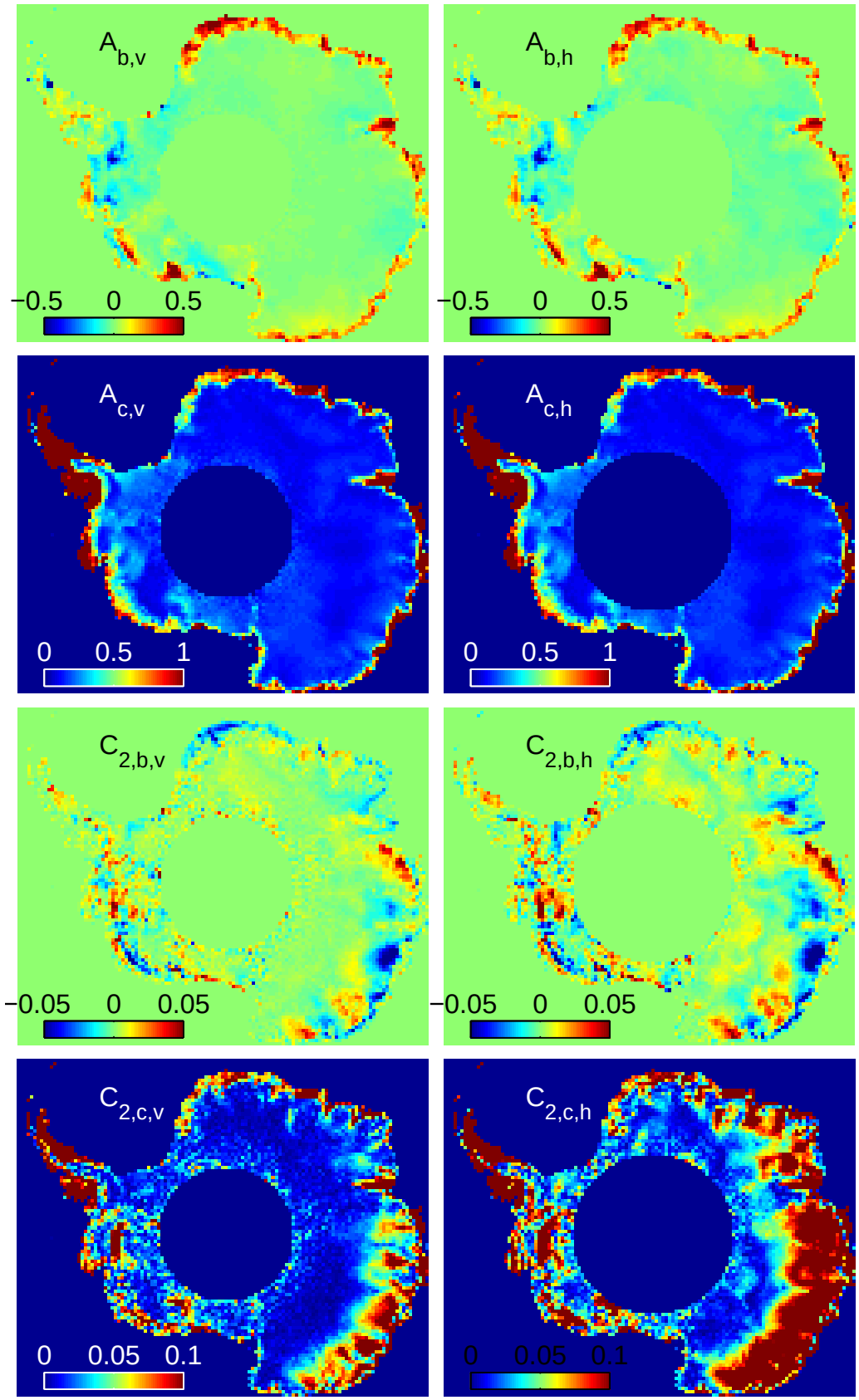

Figure 4.5: Maps of pixelwise values of A_b, A_c, $C_{2,b}$, and $C_{2,c}$.

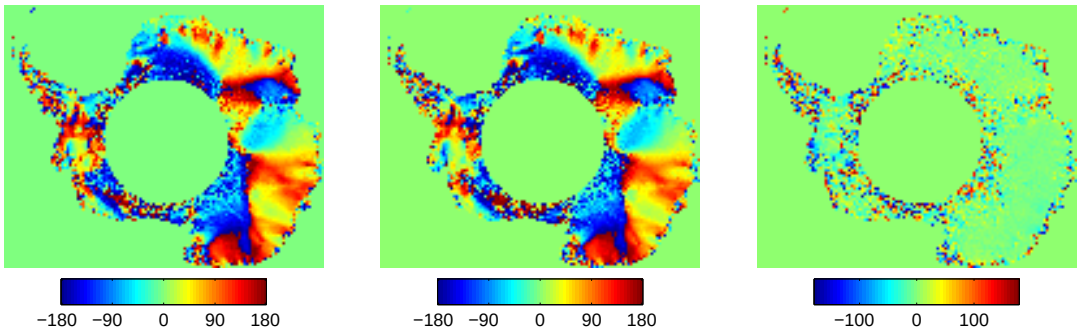

(a) Maps of second order azimuth modulation phase, ϕ_2, V-pol, in degrees relative to north. Left) 1999. Center) 2007. Right) Difference, 2007 - 1999.

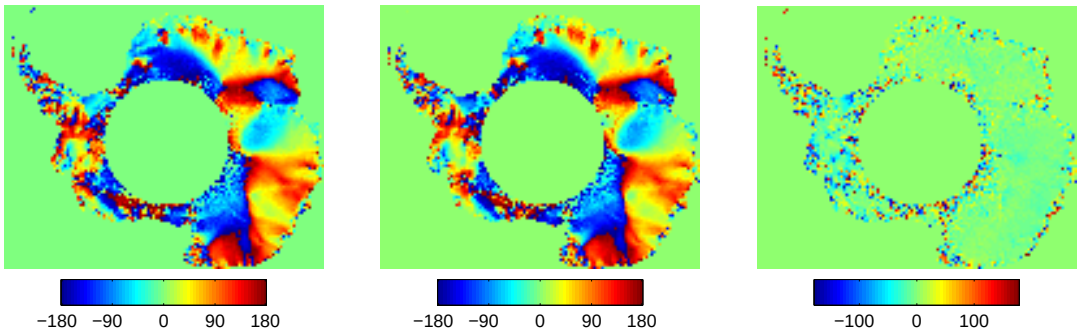

(b) Maps of second order azimuth modulation phase, ϕ_2, H-pol, in degrees relative to north. Left) 1999. Center) 2007. Right) Difference, 2007 - 1999.

Figure 4.6: Second order azimuth modulation phase and phase difference maps.

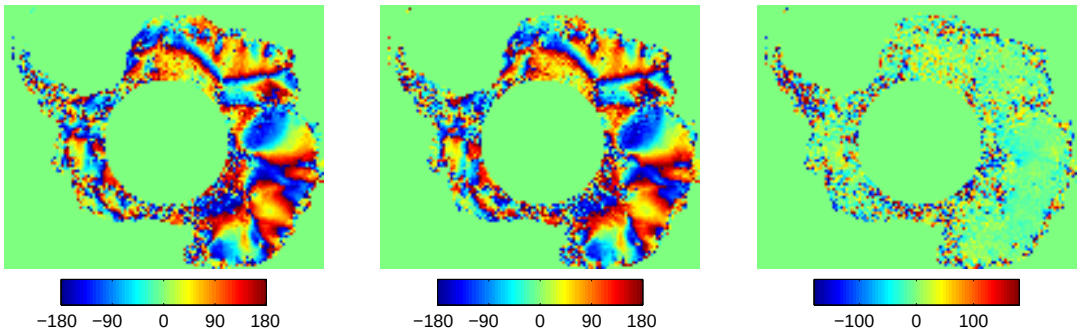

(a) Maps of fourth order azimuth modulation phase, ϕ_4, V-pol, in degrees relative to north. Left) 1999. Center) 2007. Right) Difference, 2007 - 1999.

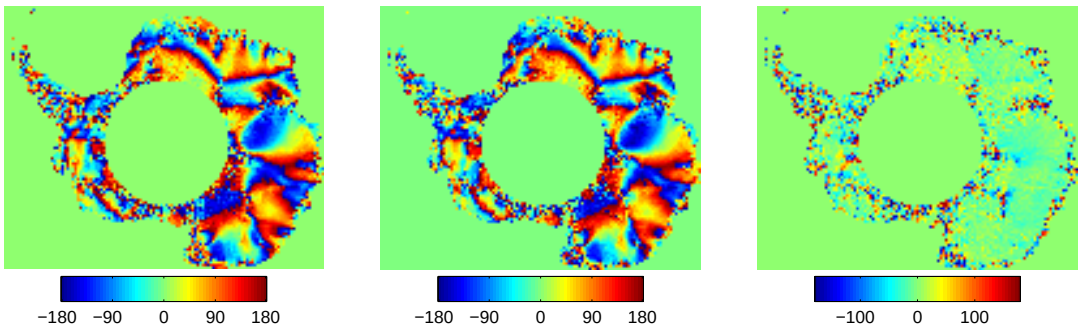

(b) Maps of fourth order azimuth modulation phase, ϕ_4, H-pol, in degrees relative to north. Left) 1999. Center) 2007. Right) Difference, 2007 - 1999.

Figure 4.7: Fourth order azimuth modulation phase and phase difference maps.

4.3 Study Locations

The purpose of displaying continent-wide data for various quantities is to conveniently encapsulate how the backscatter signature of the ice sheet as a whole has changed since 1999 and to identify regions that warrant further investigation. Figure 4.8 and Table 4.2 display the locations of four regions chosen for study in detail. These locations are chosen arbitrarily because they exhibit interesting and diverse backscatter changes throughout the nearly nine year study period.

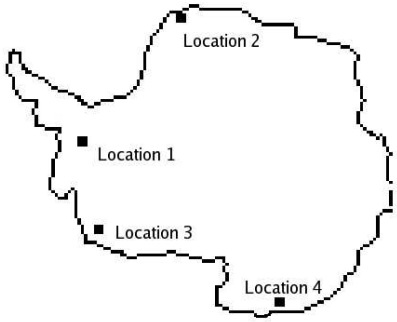

Figure 4.8: Locations of four study regions.

Table 4.2: Locations of four study regions.

		Latitude	Longitude
Location 1	Ellsworth Land	-76.29	-74.65
Location 2	Queen Maud Land	-71.73	-4.90
Location 3	Marie Byrd Land	-74.71	-125.87
Location 4	King George V Land	-68.48	144.1

4.3.1 Study Location 1 - Ellsworth Land

Ellsworth Land is situated in West Antarctica at the base of the Antarctic Peninsula. Although the general area is mountainous, the location I have selected

appears to be free of exposed mountain tops in visual images [14], [39], suggesting that snow and ice are the dominant backscatter features. Surface temperature data (Figure 4.9) suggests that this region falls within the percolation zone.

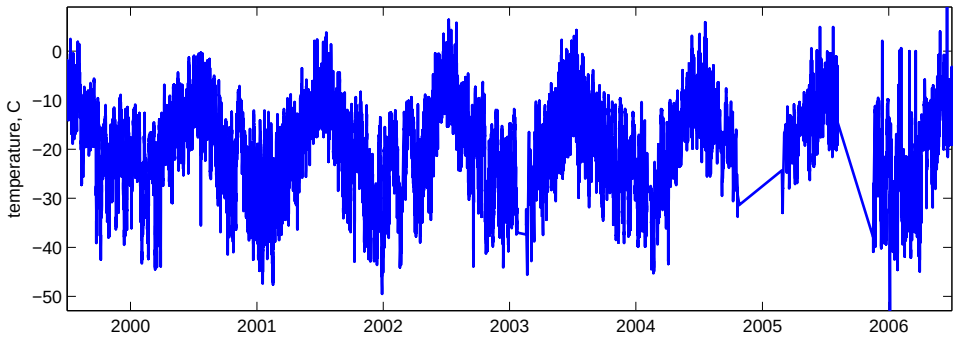

Figure 4.9: NCAR [29] reported air temperature at study region 1. Some gaps exist in the data set during 2005 and 2006.

Time series data of average V-pol backscatter (σ^0_V) and average H-pol backscatter (σ^0_H), with model (Equation 4.2) superimposed, are shown in Figure 4.10. Also shown is the quasi polarization ratio (QPR), defined as $\sigma^0_V - \sigma^0_H$, which gives a measure of how the two data sets are changing relative to each other. This quantity is not a true polarization ratio because the data sets are observed at different incidence angles.

The data shows an average seasonal variation of 0.26 dB and a strongly decreasing linear trend of over 0.5 dB for both V- and H-pol, with the H-pol data exhibiting a somewhat steeper negative trend. This is also evidenced in the generally increasing trend of the QPR. Bingham and Drinkwater [4] have speculated that similar, although less drastic, backscatter trends such as this are the result of thermal forcing, which accounts for the seasonal variations, and accumulation, which accounts for the negative linear trend. Thermal forcing, the result of seasonal temperature variations, subtly effects the size and dielectric constant of individual crystals. This causes the observed small seasonal variation seen here and the backscatter/temperature relationship (Figures 3.22 and 3.23) seen at the control locations in the previous chapter.

Scattering models of layered firn (see [5], [41]) suggest that damping due to a 600 mm think layer of fine-grained, high-density accumulation falling on top of an older layer of low-density, coarse-grained firn could decrease backscatter by 0.5 dB. In regions with well-established scattering layers, such as those caused by melt/refreeze events, less accumulation could account for similar decreases [4]. Given this region's location within the percolation zone, it's relatively low altitude, and the modest quantity of accumulation needed to produce the observed changes, it is not unreasonable to conclude that the mechanism driving long term negative change in this region is the accumulation of fine-grained snow upon layers of more substantial scatterers, possibly the results of a severe melt-refreeze event in the recent past.

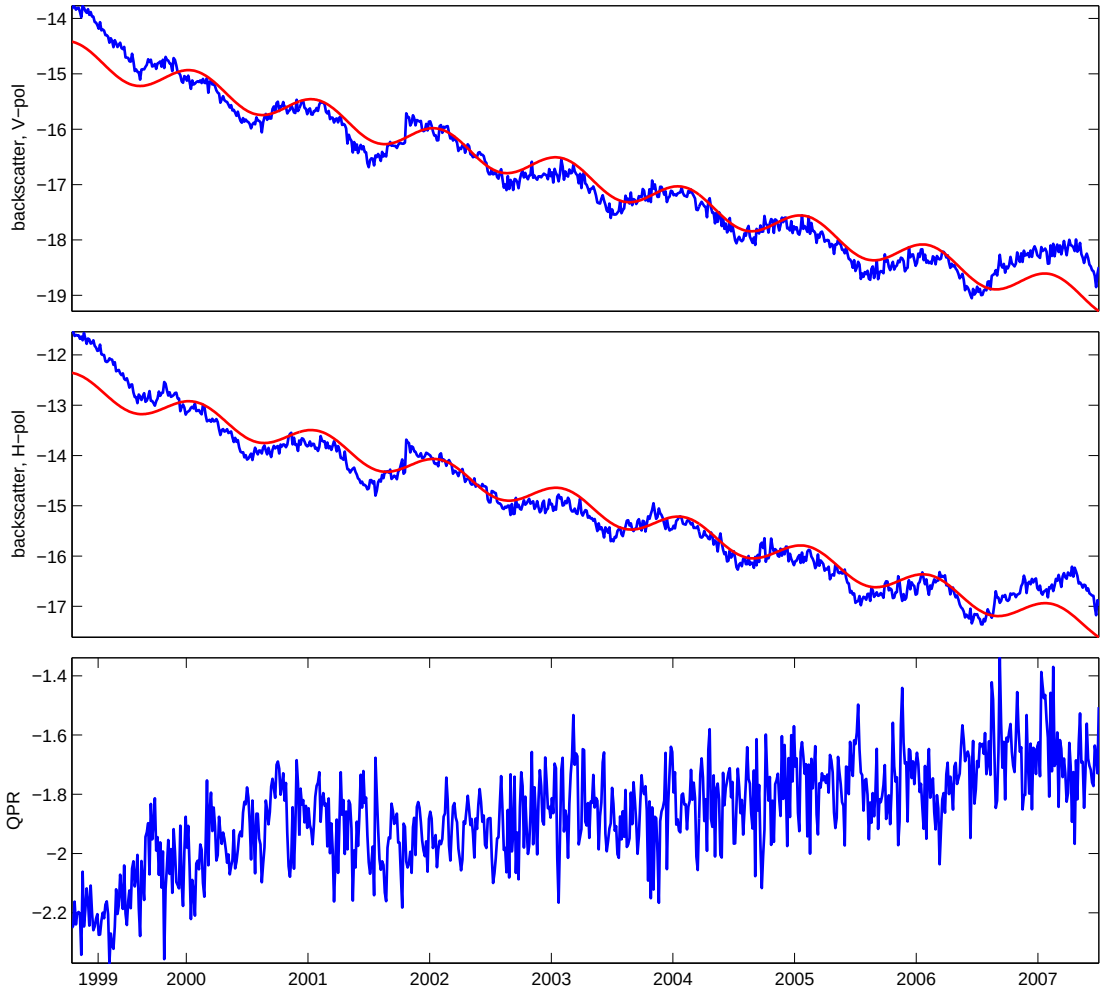

Figure 4.10: Average backscatter at location 1, Ellsworth Land. Top) V-pol. Model: $\sigma_V^0 = -14.67 - 0.52t + 0.26\cos(2\pi t - 8.78)$. Middle) H-pol. Model: $\sigma_H^0 = -12.60 - 0.57t + 0.26\cos(2\pi t - 8.78)$. Bottom) Quasi Polarization Ratio, $\sigma_V^0 - \sigma_H^0$.

4.3.2 Study Location 2 - Queen Maud Land

Queen Maud Land is at a lower elevation and latitude than location 1. Time series data at this location, shown in Figure 4.11, shows large decreases in backscatter indicating melt events during every austral summer from 2001/2002 through 2004/2005, with smaller such decreases during the 2000/2001 and 2005/2006 melt seasons. There is little or no indication of melting during the 1999/2000 and 2006/2007 summers. The 2003/2004 melt event was both the most severe, in terms of overall backscatter decrease, and the longest. Interestingly, the melt event during the 2001/2002 is associated with a large negative spike in QPR, in this case because H-pol data "recovers" from the melt event sooner than the V-pol data. A smaller positive spike in QPR appears during the next three melt seasons, and is most noticeable during the 2003/2004 melt event. In this case the effect is at the beginning of the melt event, as the melt is apparent in H-pol data slightly earlier than in V-pol data. These results suggest that the H-pol scattering in dominated by near-surface volume scattering relative to V-pol scattering, which is dominated by scatterers deeper in the snow pack. The greater sensitivity of H-pol illumination relative to V-pol illumination to the presence of liquid water in snow is well established [27].

After several of the melt events there is a substantial, up to 4 dB, increase in average backscatter. This is attributable to the formation of relatively large ice pipes and lenses and an overall increase in grain size upon refreezing [4]. In the absence of large melt events, there is a generally decreasing backscatter trend. After the large 2004/2005 melt the magnitude of backscatter change is approximately -1.5 dB per year. As in location 1, it is reasonable to conclude that this behavior is the result of accumulation damping the backscatter from these newly-formed scatterers. These results give credence to the assertion of a severe melt even at location 1 in the recent past.

4.3.3 Study Location 3 - Marie Byrd Land

The study locations in Marie Byrd Land and Queen Maud Land exhibit very different behaviors, despite being at comparable latitudes and elevations, see Figure

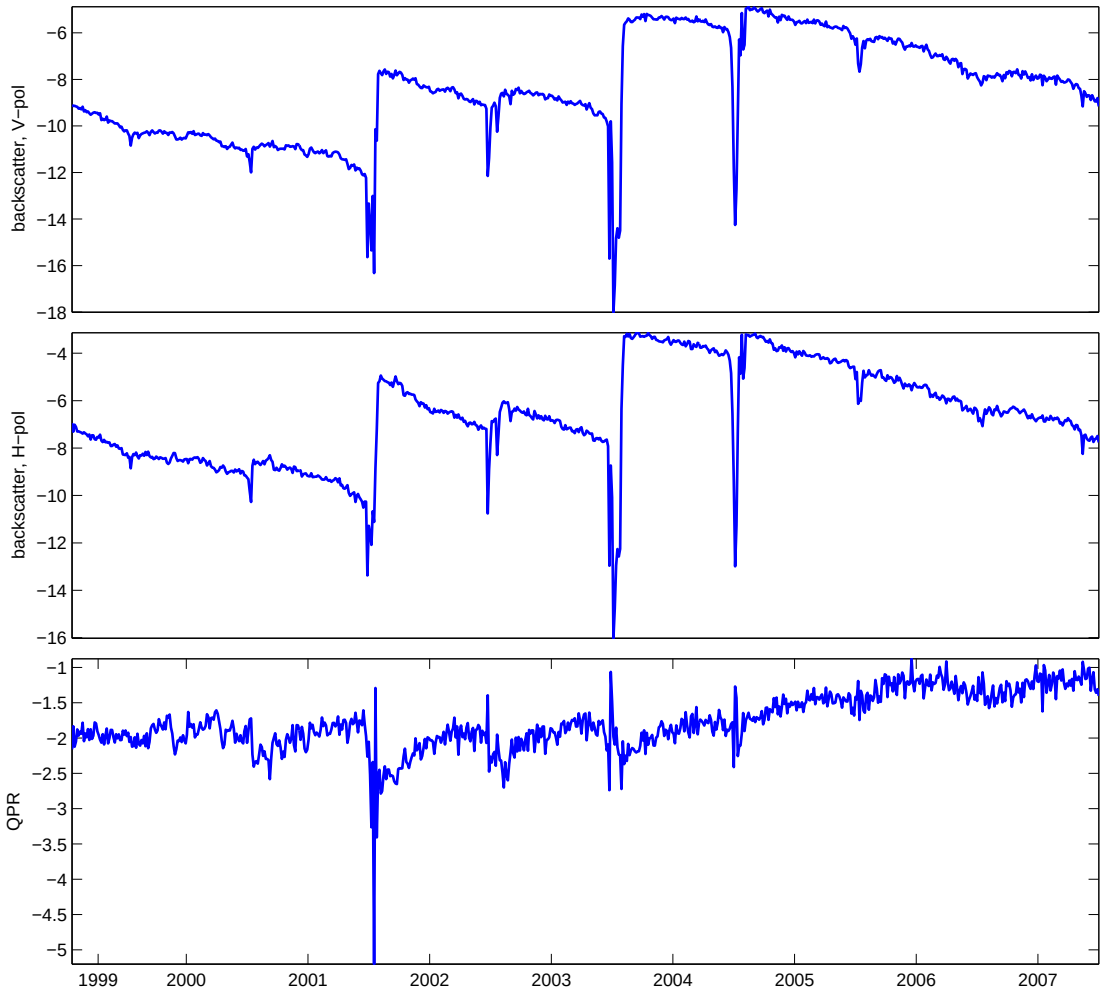

Figure 4.11: Average backscatter at location 2, Queen Maud Land. The erratic nature of seasonal variations at this location results in a poor fit of (4.2). Top) V-pol, σ^0_V. Middle) H-pol, σ^0_H. Bottom) Quasi Polarization Ratio, $\sigma^0_V - \sigma^0_H$.

4.12. The study location in Queen Maud Land shows frequent and severe melt events, while the location in Marie Byrd Land shows evidence of only two melt events during the eight melt seasons observed. The backscatter values at location 2 are also much smaller than at location 1; even the smallest backscatter values observed during severe melt events at location 1 are generally brighter than typical backscatter values at location 2.

The first potential melt event observed at location 2, during the 2001/2002 austral summer, lacks the large backscatter decrease that serves as direct evidence of

melting. Instead, the only evidence of melt is a drastic increase in backscatter and a noticeable negative spike in QPR. I find it likely that the drastic backscatter increase is similar to that seen in location 3, and caused by newly formed ice features. In this case the ice features were formed by a melt event that was too short, less than 4 days, to be observed by my temporal binning scheme.

The second melt event, during the 2004/2005 austral summer, shows direct evidence of a very short melt event, perhaps less than eight days long. After the melt the backscatter pattern seen at location 2 - that is, a sudden increase in backscatter followed by a gradual negative trend for several years - is observed here. In this case, however, the sudden increase is approximately 6 dB and the gradual decrease is over 3 dB per year, both of which are much more dramatic than seen at location 2. The change in the QPR associated with this melt event is also very different than that seen previously, here the QPR approaches its previous levels only after years, as opposed to the almost instantaneous normalization seen earlier. This difference in QPR behavior, combined with the overall smaller backscatter values at location 3 relative to location 2, suggest that the melt/refreeze and accumulation mechanisms presumed responsible for backscatter signature evolution at location 2 likely do not apply here. I am unable to offer an explanation for the backscatter behavior during 2007, where an anomalous 2 dB peak is observed.

4.3.4 Study Location 4 - King George V Land

The time series of average backscatter from King George V Land, shown in Figure 4.10, is somewhat less interesting that of the locations previously considered, with regular seasonal variations and a fairly consistent interannual mean. The polarization ratio also remains consistent throughout. In this region, however, there is a significant seasonal variation in second order backscatter modulation, shown in Figure 4.14. In fact the seasonal variation in backscatter modulation is nearly as large as the seasonal variation in average backscatter for H-pol data (0.21 dB to 0.24 dB). The likely mechanism behind this behavior is again thermal forcing, which changes properties of the firn nearest the surface the most, which in turn decreases

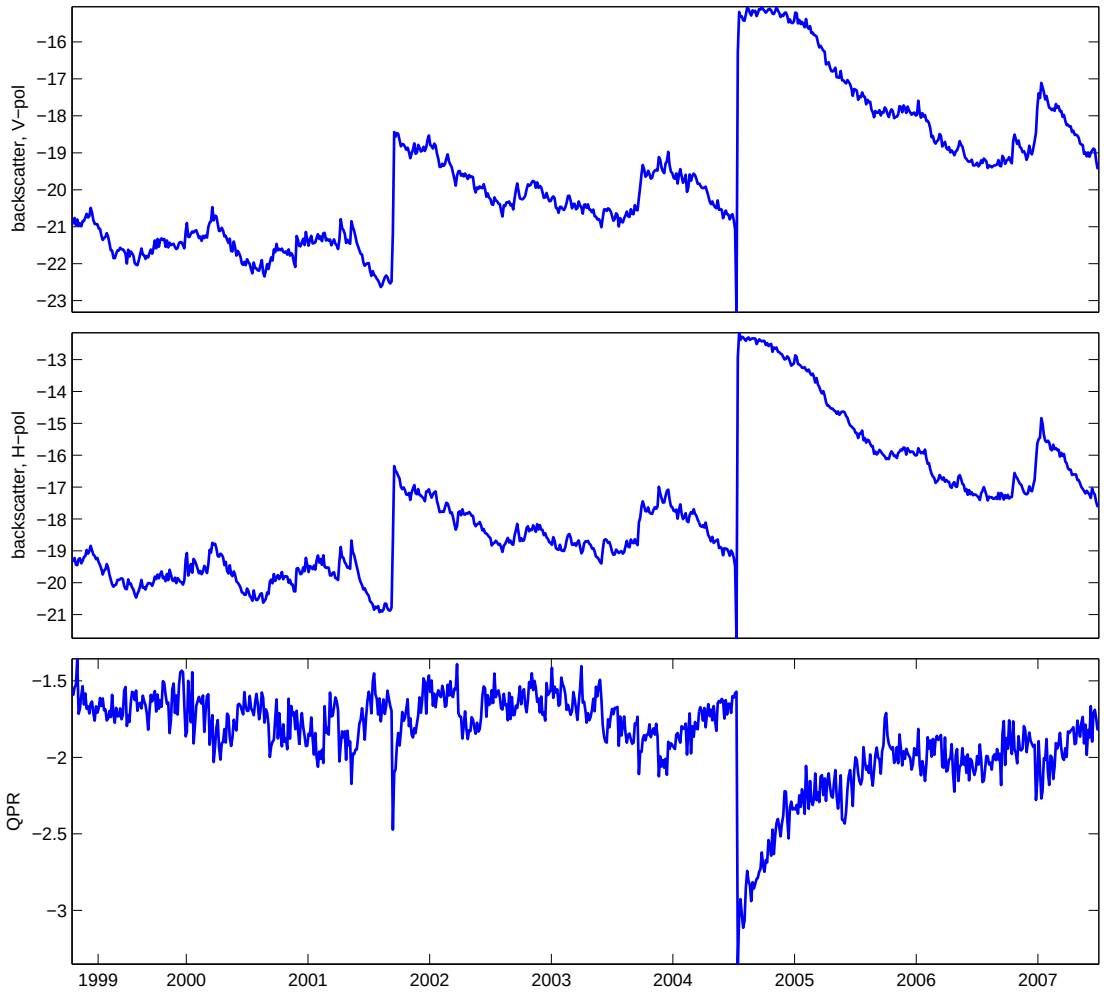

Figure 4.12: Average backscatter at location 3, Marie Byrd Land. The erratic nature of seasonal variations at this location results in a poor fit of (4.2). Top) V-pol, σ^0_V. Middle) H-pol, σ^0_H. Bottom) Quasi Polarization Ratio, $\sigma^0_V - \sigma^0_H$.

the contribution from surface scatterers and increases the relative contribution from azimuthally isotropic volume scatterers. Why this behavior is not more apparent over more of the continent remains undetermined.

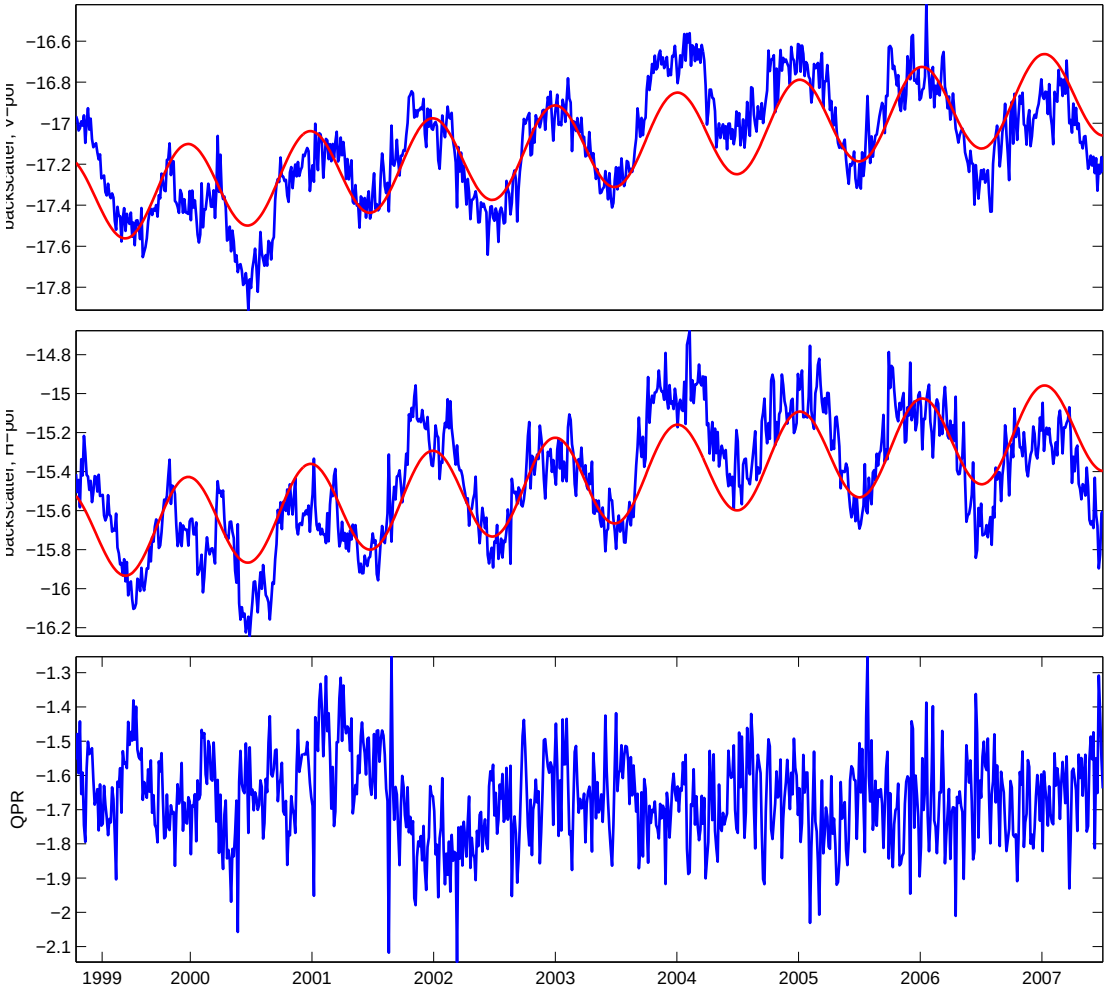

Figure 4.13: Average backscatter at location 3, King George V Land. Top) V-pol. Model: $\sigma^0_V = -17.37 + 0.062t + 0.21\cos(2\pi t + 28.64)$. Middle) H-pol. Model: $\sigma^0_V = -15.73 + 0.067t + 0.24\cos(2\pi t + 28.04)$. Bottom) Quasi Polarization Ratio, $\sigma^0_V - \sigma^0_H$.

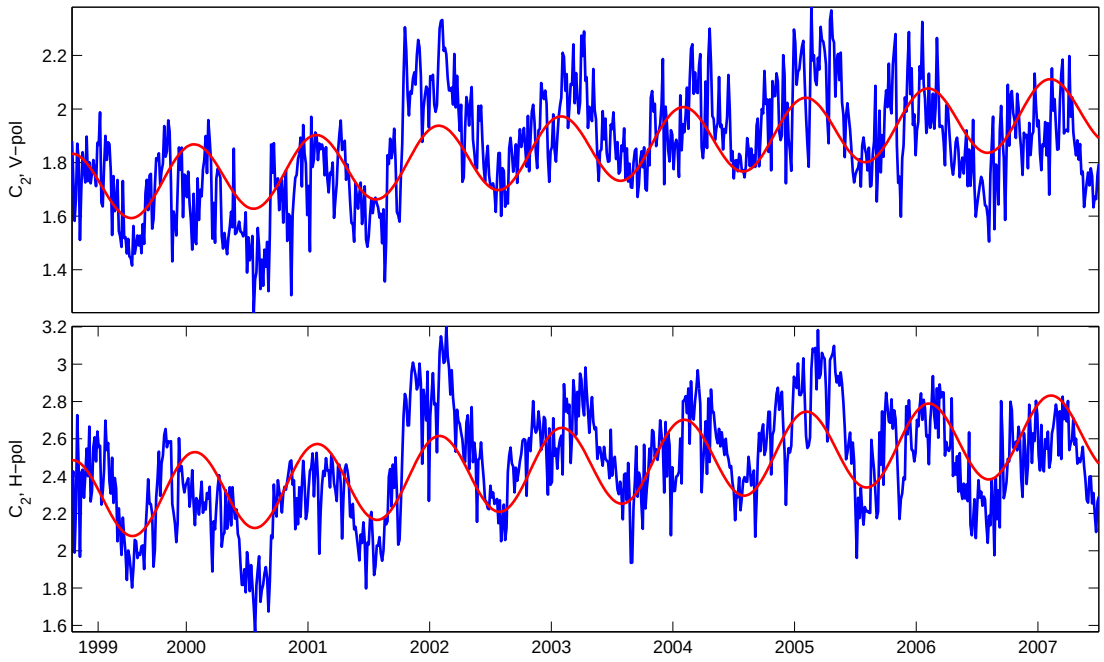

Figure 4.14: Second order backscatter azimuth modulation at location 4, King George V Land. Top) V-pol. Model: $\sigma^0_V = 1.70 + 0.035t + 0.13\cos(2\pi t - 0.98)$. Bottom) H-pol. $\sigma^0_V = 2.27 + 0.043t + 0.21\cos(2\pi t - 0.21)$.

4.4 Summary

There are significant seasonal and interannual variations in the backscatter signature from much of the Antarctic continent. As expected, most of the regions demonstrating the largest changes are at lower latitudes and elevations, with much of the coastal regions showing a generally increasing trend in average backscatter and much of West Antarctica showing a generally negative trend in backscatter. Seasonal variations in backscatter throughout most of the continent are primarily attributed to thermal forcing, which alters the physical properties of the crystals. Severe seasonal variations along the coast are the result of melting, which which introduces liquid water into the snow and greatly dampens backscatter. Interannual trends are likely the results of melt/refreeze events, which create large ice scatterers within the snow pack, and accumulation, which further buries these ice formations. With the exception of the ice sheet crest, which has been shown to be geographically stable, and extreme southern regions where QuikSCAT has insufficiently variable coverage, the Antarctic continent has been shown to be a dynamic target.

Chapter 5

Long Term Change in the Backscatter Signature of the Antarctic Ice Sheet

In the previous chapter I studied change in the backscatter signature of the Antarctic ice sheet as observed by QuikSCAT. In this chapter I extend that analysis to include data taken from two other sensors, SASS and NSCAT, to study how the backscatter properties of the ice sheet have changed since 1978. Rather than use uniform four-day long temporal bins I use combined same-season data from individual sensors to track interannual changes only. I use SASS data from days 185 through 216, 1978, NSCAT data from days 170 through 179, 1997, QuikSCAT data from days 201 through 204, 1999 and QuikSCAT data from days 181 through 184 for years 2000 through 2007. These dates represent the closest seasonal match given the various times of year that the three sensors were in operation. The slight seasonal mismatch should not introduce inconsistencies as all occur during the austral winter, well before the Austral melt season [42]. I also use only V-pol data in this chapter, as SASS operated for most of its mission in V-pol mode only. I begin by comparing data taken from all three sensors at Dome C (study location 1 in Chapter 3) and the three study locations from Chapter 4. I then consider comparisons of continent wide data.

5.1 Study Locations

As with any data fusion, comparing data from different sensors is difficult. In the previous chapter I was able to use single 44.5 km by 44.5 km pixels as my study locations. Here I accommodate SASS and NSCAT's lower resolution and smaller number of observations by including data from the eight neighboring pixels of each

study location into the data presented. This results in study locations of approximately 133 km by 133 km. In all cases I am careful to avoid using pixels that fall on the coast, as this could result ocean backscatter contaminating the data. Other sensor differences for which I compensate are observation geometry and frequency.

5.1.1 Controlling for Observation Geometry

Controlling for observation geometry differences between sensors is somewhat difficult, as both SASS and NSCAT have variable azimuth and incidence angles. Long and Drinkwater [3] modified the empirical model (Equation 4.1) with

$$\begin{aligned} \mathcal{G} &= \{1\}, \\ \mathcal{F} &= \{1, 2\}, \\ C_1 &= c_1 + d_1(\theta - \theta_0), \\ C_2 &= c_2 + d_2(\theta - \theta_0), \end{aligned} \tag{5.1}$$

to control for azimuth and incidence angle interdependencies in their study of data collected by NSCAT, ERS-1/2 and the SSM/I radiometer. Unfortunately, this method becomes problematic when dealing with data collected by SASS, which has much less azimuth diversity than the other sensors. Since this full model (Equations 4.1, 5.1) has four azimuth angle dependent terms, four cross terms, and only one incidence angle dependent term, this model tends to predict erroneous values in the absence of sufficiently diverse azimuth angle data. An example of SASS data from Dome C with this model-fit superimposed is shown in Figure 5.1.

In the absence of an adequate method to effectively control independently for azimuth and incidence angle effects on backscatter from SASS, and to a lesser extent NSCAT, I am forced to neglect azimuth angle effects and instead control only for incidence angle. Thus, I make the following adjustments to Equation (4.1) when dealing with SASS and NSCAT data,

$$\begin{aligned} \mathcal{G} &= \{1\}, \\ \mathcal{F} &= \emptyset \Rightarrow C_j = 0, \end{aligned}$$

which results in the much simpler model

$$\sigma^0 = A + B(\theta - \theta_0). \tag{5.2}$$

I set $\theta_0 = 54.26$ to correspond to QuikSCAT's V-pol data set. Unfortunately, this results in some discontinuities between sensor data sets due to differences in azimuth sampling. Previous studies for Greenland [6, 43], where azimuth modulation is small relative to Antarctica, have used implementations of the SIR [20] algorithm, which enhances spatial resolution but does not consider azimuth modulation. Since I use raw data, I am able to make observations about possible azimuth angle effects at each of the study locations despite not controlling for it explicitly.

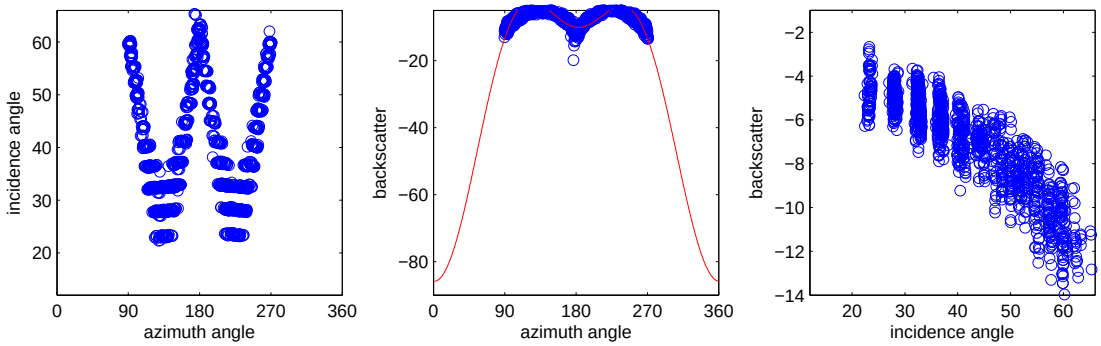

Figure 5.1: SASS observation geometry at Dome C, for days 185 through 216, 1978. Left) Azimuth angle, incidence angle interdependencies. Middle) Backscatter dependence on azimuth angle with superimposed model. Note the absurd predicted values in the absence of sufficiently diverse azimuth angle data. Right) Backscatter dependence on incidence angle.

5.1.2 Controlling for Frequency Differences

Controlling for the relatively small frequency differences between SASS, NSCAT, and QuikSCAT is very straightforward. If all other parameters remain constant, the radar equation predicts a change in backscatter of

$$\Delta\sigma^0 = -2(10\log(\frac{c}{f}) - 10\log(\frac{c}{f_0})) \tag{5.3}$$

for a frequency f compared to a reference frequency, f_0. I let QuikSCAT's operating frequency of 13.6 GHz serve as a reference, and I compensate for SASS and NSCAT's frequency difference accordingly. SASS and NSCAT's slightly higher operating frequencies result in adjustments of 0.25 and 0.62 dB relative to QuikSCAT, see Table 5.1. For this calculation to be appropriate it is necessary to assume that the principle backscatter mechanism is small relative to the wavelength of all sensors [17]. For volume scattering effects this assumption is easily justified in this case, where typical grain sizes of Antarctic firn are on the order of 0.1 mm [44], and wavelengths vary from 21 mm to 22 mm. For glazed or very rough surfaces, or in the presence of other larger scatterers, this calculation may introduce a small bias, although the bias is likely very small relative to the adjustment. All backscatter values from SASS and NSCAT presented in this chapter are adjusted by the relevant amount.

Table 5.1: Frequency difference backscatter adjustments.

Sensor	Frequency	Adjustment
QuikSCAT	13.600 GHz	-
SASS	14.600 GHz	0.62 dB
NSCAT	13.995 GHz	0.25 dB

5.1.3 Dome C

As discussed in Chapter 2, the ice sheet crest is the Antarctic location where one expects to see the least change, and indeed there is little change in data collected

by the three sensors, see Figure 5.2. Since QuikSCAT reported very little azimuth modulation ($C_2 = 0.057$ dB in 1999) at this location, distortions due to intra-sensor differences in azimuth sampling are likely very small. B values for both NSCAT and SASS are also very similar, -0.17 and -0.18 respectively, although the NSCAT data shows that beyond approximately 50° incidence angle effects may deviate slightly from the linear model, and SASS data shows high variability. If the general backscatter properties of Dome C have been consistent since 1978 - a not unreasonable but somewhat bold assertion given the absence of temperature or other ground truth data - then the data shown in Figure 5.2 suggests that backscatter from these three sensors can be compared, after adjusting for frequency and incidence angle effects, to within approximately 0.5 dB.

5.1.4 Location 1 - Ellsworth Land

SASS data from Location 1 in 1978 is much brighter than that observed by any other instrument, and NSCAT observations in 1997 are much darker. There are two plausible explanations for this behavior in light of the data presented at this location in the previous chapter: (1) The NSCAT data is anomalous and there has been a consistent negative trend in backscatter at this location since at least 1978 as a result of damping due to accumulation. (2) There was a severe melt event in Ellsworth Land either during the 1997/1998 or 1998/1999 melt season (and possibly others between 1978 and 1997) that produced bright ice scatterers that were subsequently buried under accumulation, as described in Chapter 4. In the absence of further evidence, I find both scenarios equally deserving of consideration.

Azimuth modulation reported by QuikSCAT at this location in 1999 was relatively large at $C_2 = 0.31$ dB and $C_4 = 0.22$ dB. Systematic distortions due to intra-sensor differences in azimuth sampling, however, are likely much smaller than this, as the empirical model (Equation 4.1) appears to describe the erratic dependence of backscatter on azimuth angle in this location (see Figure 5.4) more poorly than it does in others (see Figures 4.1 and 5.9).

5.1.5 Location 2 - Queen Maud Land and Location 3 - Marie Byrd Land

In both Queen Maud Land and Marie Byrd Land there is a overall increase in average backscatter since 1978, with a slight decrease in backscatter during 2000 and 2001, see Figures 5.5 and 5.6. Also, in both locations the dependence of backscatter on incidence angle, B, is slightly greater as observed by NSCAT in 1997 than by SASS in 1978, see Figure 5.12, discussion of the significance of these differences is saved for the following analysis (Section 5.2). At these locations there is a possibility of uncontrolled for azimuth modulation effecting the intra-sensor calibration, the value of C_2 at each location is 0.12 dB and 1.42 dB respectively, with somewhat more structure than is seen at location 1, see Figure 5.7. At location 3 the azimuth modulation is dominated by backscatter observed at azimuth angles close to north (zero degrees), as is common at southern latitudes.

5.1.6 Location 4 - King George V Land

The change in backscatter signature at King George V Land is different than at the previous study locations. QuikSCAT observed changes are small, approximately 0.5 dB, relative to the difference between the backscatter observed by SASS and QuikSCAT, which is greater than 2 dB. Also unlike the other locations, QuikSCAT data reveals very strong azimuth modulation at this location, which could distort the SASS and NSCAT observations if uncontrolled for. Fortunately this is the one study location for which SASS has sufficiently diverse azimuth observations to use the full Long and Drinkwater backscatter signature model (Equations 4.1, 5.1). SASS, NSCAT, and time series data with model fits are shown in Figure 5.8. Relevant backscatter signature parameters are listed in Table 5.2. Azimuth modulation for NSCAT and SASS data are approximately 1 to 2 dB, and the linear dependence of backscatter on incidence angle varies from 0.15 to 0.23 dB per degree depending on azimuth angle. Azimuth modulation parameters from QuikSCAT in 1999 are $C_1 =$ 0.30 dB and $C_2 = 1.49$ dB, see Figure 5.9, which in general agrees with SASS and NSCAT data.

Table 5.2: Values of backscatter signature parameters at location 4.

Fixed Azimuth Angle, $\sigma^0((\theta-\theta_0),\phi=\chi)$. $\theta_0 = 54.24$		
	SASS	NSCAT
$\chi = 0$	$-12.97 - 0.23(\theta-\theta_0)$	$-14.94 - 0.22(\theta-\theta_0)$
$\chi = 90$	$-12.97 - 0.15(\theta-\theta_0)$	$-14.94 - 0.17(\theta-\theta_0)$
$\chi = 180$	$-12.97 - 0.21(\theta-\theta_0)$	$-14.94 - 0.22(\theta-\theta_0)$

Fixed Incidence Angle, $\sigma^0(\theta_0,\phi)$.	
SASS	$-12.97 + 1.20\cos(\phi-31) + 0.51\cos(2\phi-13)$
NSCAT	$-14.94 + 1.39\cos(\phi+10) + 1.79\cos(2\phi+145)$

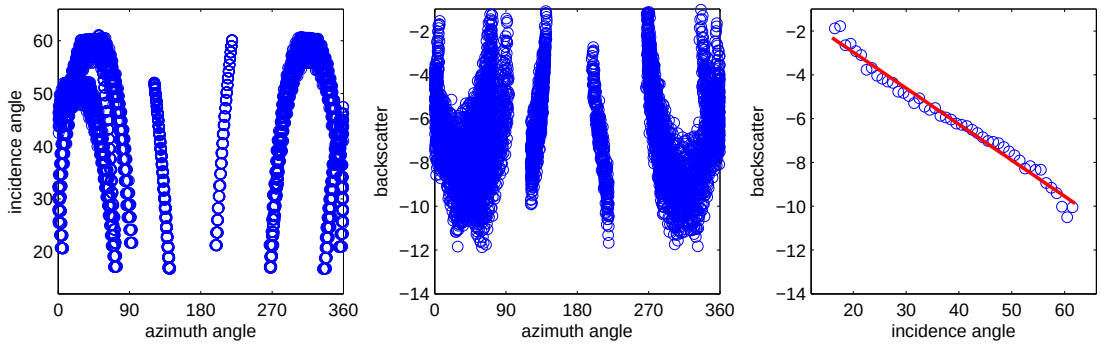

(a) NSCAT observation geometry and backscatter at Dome C. Left) Azimuth angle vs. incidence angle. Center) Azimuth angle vs backscatter. Right) Incidence angle vs backscatter. Data is averaged over one degree incidence bins, B = -0.17.

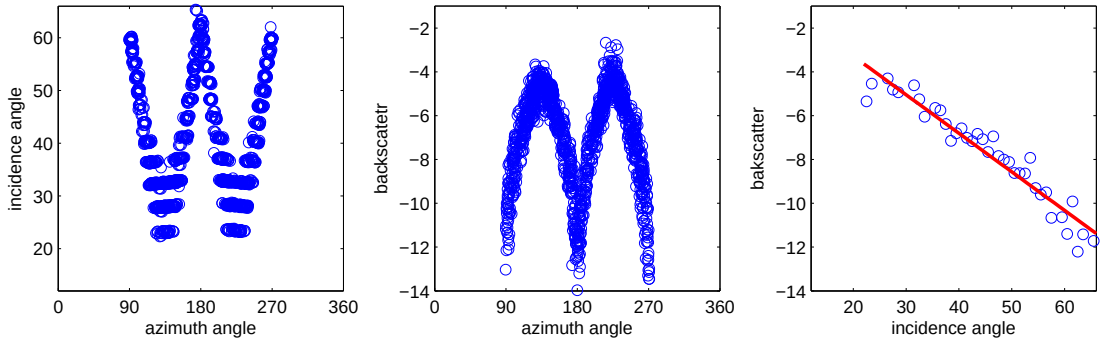

(b) SASS observation geometry and backscatter at Dome C. Left) Azimuth angle vs. incidence angle. Center) Azimuth angle vs backscatter. Right) Incidence angle vs backscatter. Data is averaged over one degree incidence bins, B = -0.18.

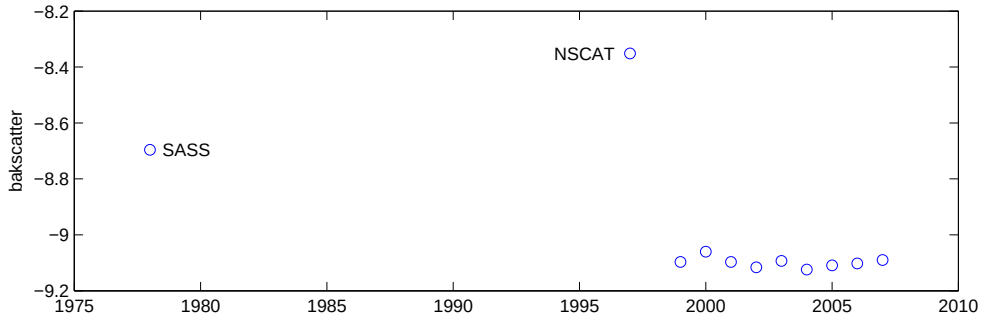

(c) Time series of A data at Dome C. The data point in 1978 is from SASS, the data point in 1997 is from NSCAT, the data points from 1999 through 2007 are from QuikSCAT.

Figure 5.2: Dome C A measurements.

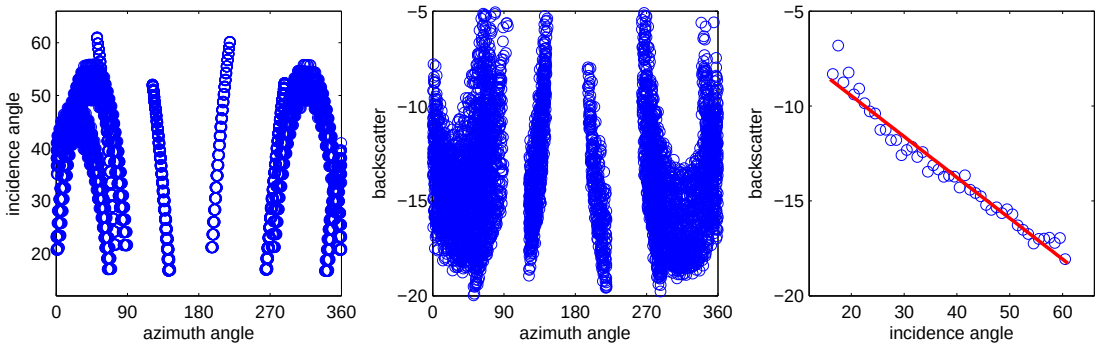

(a) NSCAT observation geometry and backscatter at Location 1. Left) Azimuth angle vs. incidence angle. Center) Azimuth angle vs backscatter. Right) Incidence angle vs backscatter. Data is averaged over one degree incidence bins, B = -0.22.

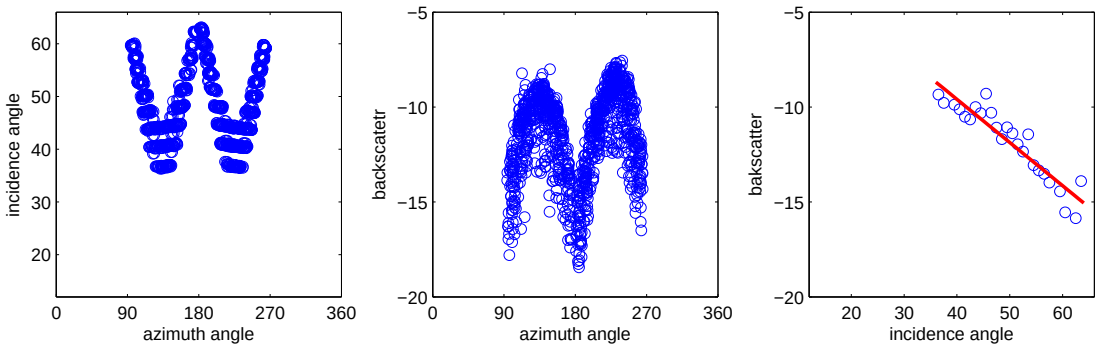

(b) SASS observation geometry and backscatter at Location 1. Left) Azimuth angle vs. incidence angle. Center) Azimuth angle vs backscatter. Right) Incidence angle vs backscatter. Data is averaged over one degree incidence bins, B = -0.23.

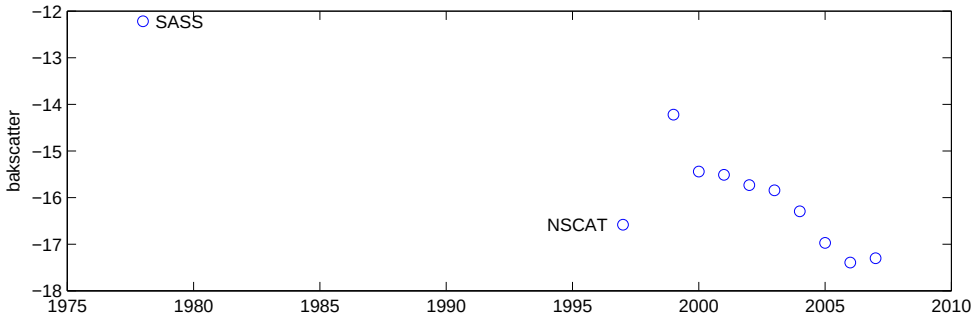

(c) Time series of A data at Location 1. The data point in 1978 is from SASS, the data point in 1997 is from NSCAT, the data points from 1999 through 2007 are from QuikSCAT.

Figure 5.3: Location 1 A measurements.

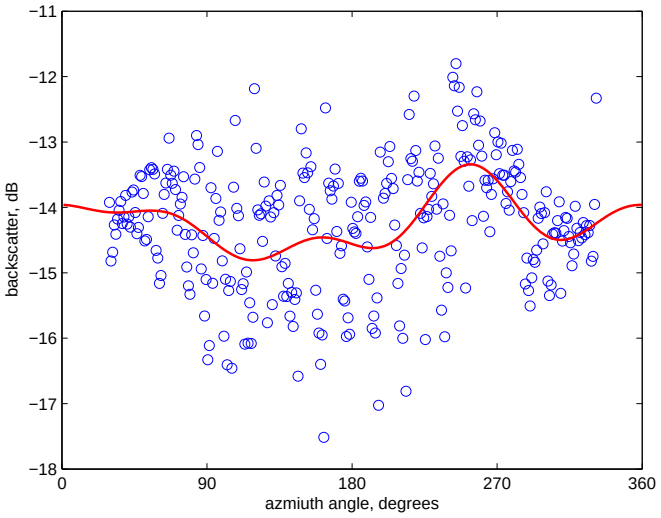

Figure 5.4: Azimuth modulation in QuikSCAT observed data at location 1, for days 201 through 204, 1999. $C_2 = 0.31$ dB. In this case the empirical model does not appear to adequately describe the underlying data.

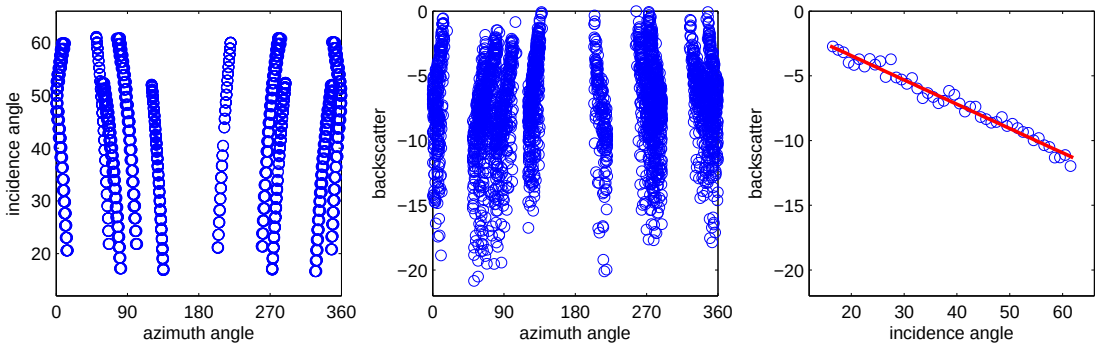

(a) NSCAT observation geometry and backscatter at Location 2. Left) Azimuth angle vs. incidence angle. Center) Azimuth angle vs backscatter. Right) Incidence angle vs backscatter. Data is averaged over one degree incidence bins, B = -0.19.

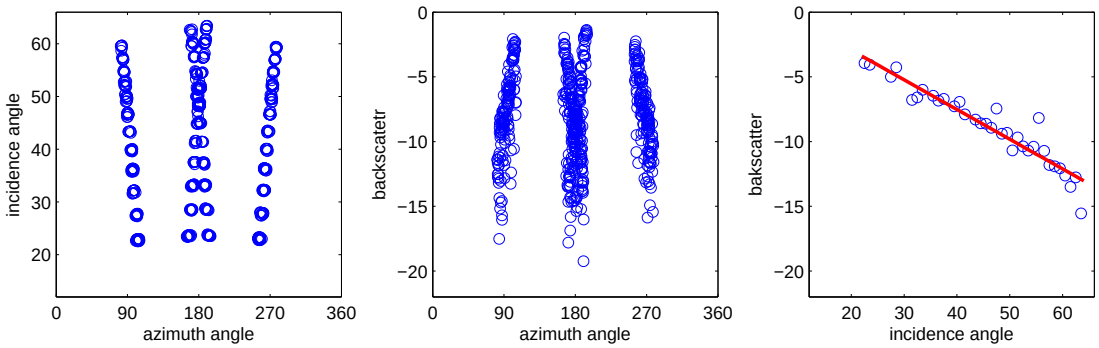

(b) SASS observation geometry and backscatter at Location 2. Left) Azimuth angle vs. incidence angle. Center) Azimuth angle vs backscatter. Right) Incidence angle vs backscatter. Data is averaged over one degree incidence bins, B = -0.23.

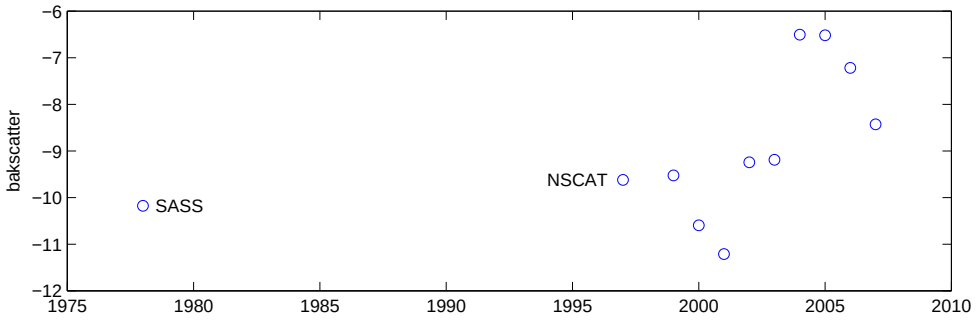

(c) Time series of A data at Location 2. The data point in 1978 is from SASS, the data point in 1997 is from NSCAT, the data points from 1999 through 2007 are from QuikSCAT.

Figure 5.5: Location 2 A measurements.

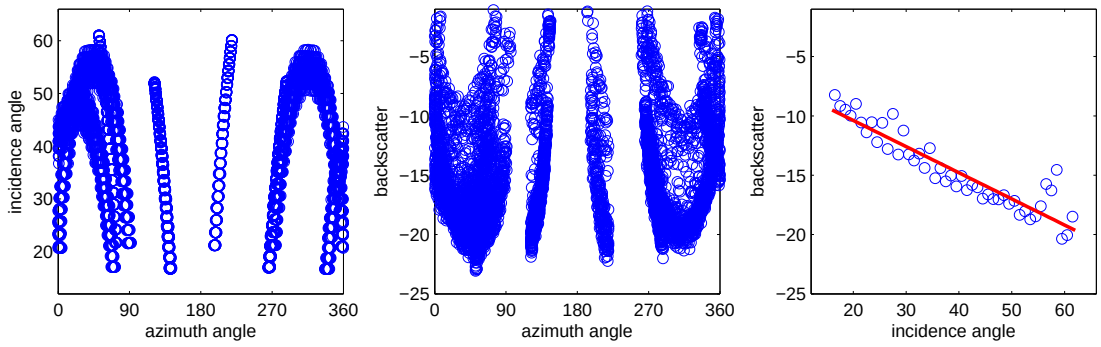

(a) NSCAT observation geometry and backscatter at Location 3. Left) Azimuth angle vs. incidence angle. Center) Azimuth angle vs backscatter. Right) Incidence angle vs backscatter. Data is averaged over one degree incidence bins, B = -0.22.

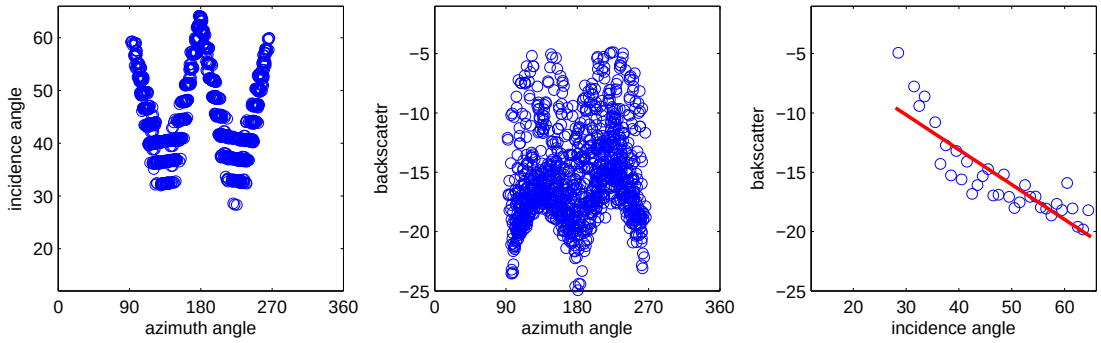

(b) SASS observation geometry and backscatter at Location 3. Left) Azimuth angle vs. incidence angle. Center) Azimuth angle vs backscatter. Right) Incidence angle vs backscatter. Data is averaged over one degree incidence bins, B = -0.29.

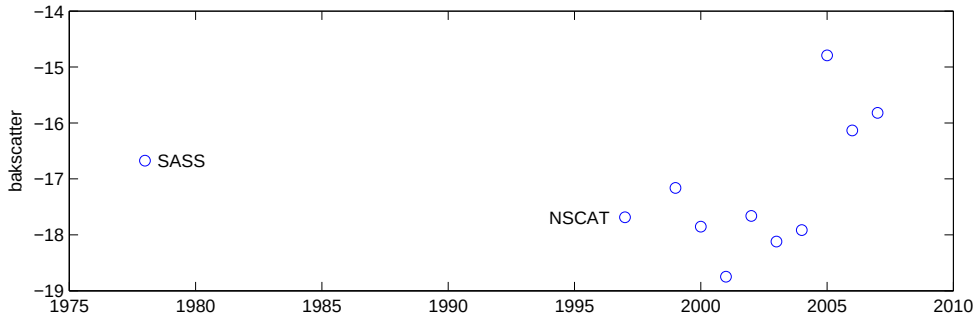

(c) Time series of A data at Location 3. The data point in 1978 is from SASS, the data point in 1997 is from NSCAT, the data points from 1999 through 2007 are from QuikSCAT.

Figure 5.6: Location 3 A measurements.

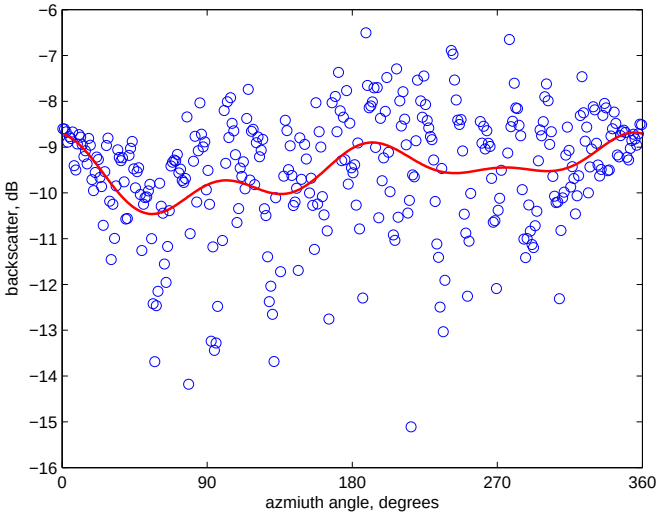

(a) QuikSCAT observed azimuth modulation at location 2. $C_2 = 0.12$ dB.

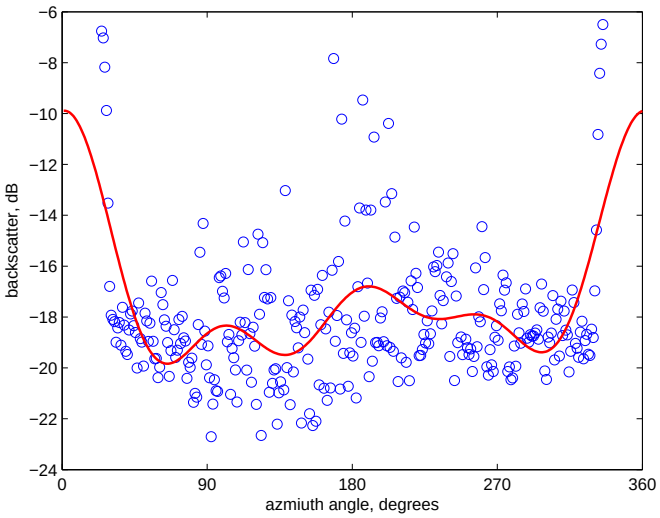

(b) QuikSCAT observed azimuth modulation at location 3. $C_2 = 1.42$ dB.

Figure 5.7: Azimuth modulation in QuikSCAT observed data at locations 2 and 3, for days 201 through 204, 1999.

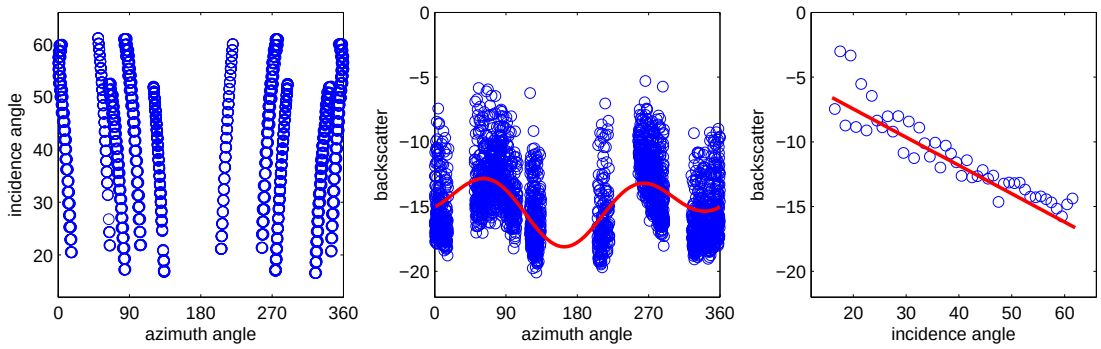

(a) NSCAT observation geometry and backscatter at Location 4. Left) Azimuth angle vs. incidence angle. Center) Azimuth angle vs backscatter adjusted for incidence angle effects. Right) Incidence angle vs backscatter adjusted for azimuth angle effects. Data is averaged over one degree incidence bins. The superimposed trend line is for a fixed azimuth angle of zero degrees, and has slope of -0.23 dB per degree.

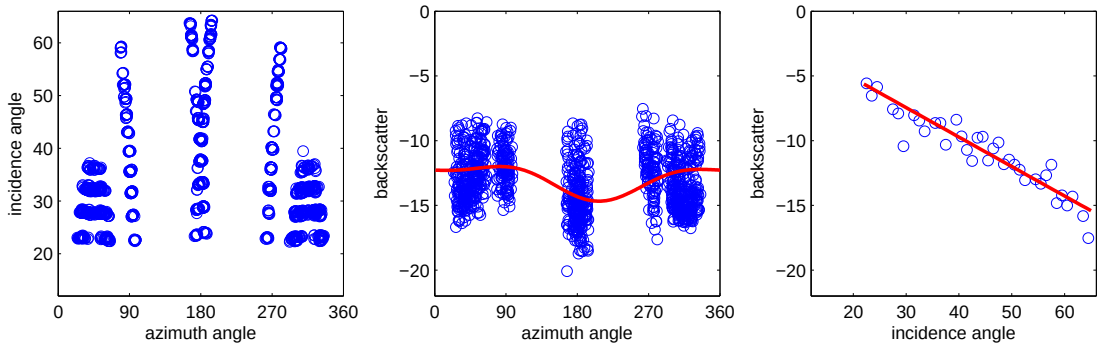

(b) SASS observation geometry and backscatter at Location 4. Left) Azimuth angle vs. incidence angle. Center) Azimuth angle vs backscatter adjusted for incidence angle effects. Right) Incidence angle vs backscatter adjusted for azimuth angle effects. Data is averaged over one degree incidence bins. The superimposed trend line is for a fixed azimuth angle of zero degrees, and has slope of -0.22 dB per degree.

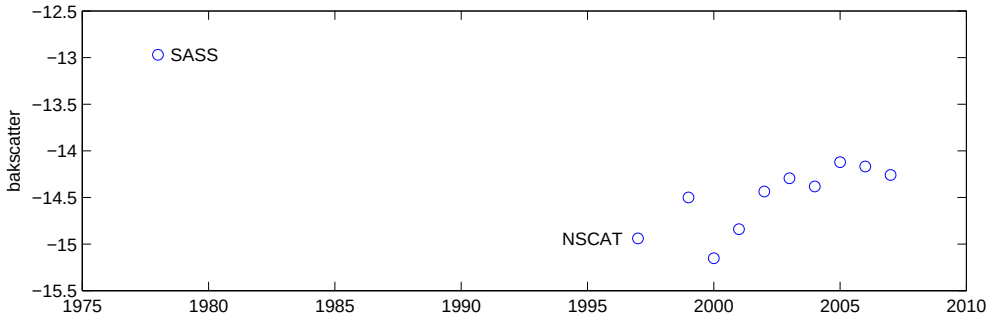

(c) Time series of A data at Location 4. The data point in 1978 is from SASS, the data point in 1997 is from NSCAT, the data points from 1999 through 2007 are from QuikSCAT.

Figure 5.8: Location 4 observation geometry and backscatter measurements. Unlike at location 1, 2, and three, there is sufficient azimuth variability to support an azimuth modulation model.

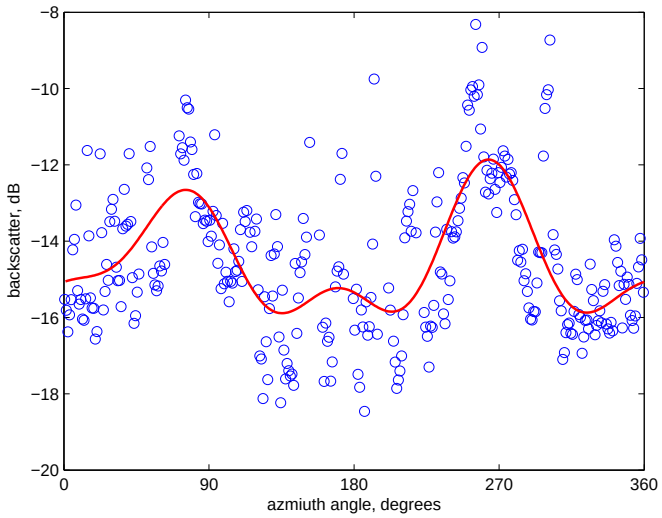

Figure 5.9: Azimuth modulation in QuikSCAT observed data at location 4, for days 201 through 204, 1999. $C_2 = 1.49$ dB.

5.2 Continental Analysis

I now consider analysis of sensor data on a continental scale. Figures 5.10 and 5.11 show A and A difference maps from SASS, NSCAT, and QuikSCAT in 1999 and 2007. Figure 5.12 shows B maps and a B difference map from SASS and NSCAT. These maps confirm and expand the results of the previous chapter and the preceding section of this chapter.

Figures 5.11 a, b, and c reveal what is perhaps an instrumentation bias between SASS and the other two sensors, as most of the continent, including the ice sheet crest, shows a slightly negative value. There are also regions of drastic change, most notably in Ellsworth Land, the remainder of West Antarctica, and along the cost. These images suggest very large structural changes to much of the West Antarctic ice sheet. They also suggest that perhaps these changes have been accelerating, as much of the change is also apparent in the QuikSCAT difference image (Figure 5.11 d). Other regions of apparently significant backscatter change are the Ross and Amery Ice Shelves. The regions of large negative change in Wilkes Land are possibly attributable to uncontrolled-for azimuth modulation effects, as they appear in the SASS/QuikSCAT images (Figures 5.11 b,c) but not in the QuikSCAT difference image (Figures 5.11 d).

Differences in B values from SASS and NSCAT are shown in Figure 5.12 and also show regions of large change. Again, West Antarctica exhibits the greatest difference, where NSCAT B values are consistently less than (more negative) corresponding SASS B values. Since this phenomena is regionally variable it is unlikely the result of instrumentation differences and likely indicative of significant changes in the structure of the ice sheet. Further study is required to resolve these questions.

5.3 Summary

Although its possible that some of the changes observed by the three Ku-Band scatterometers used in this chapter are the result of unaccounted for instrumentation differences, the spatial distribution of the observed changes makes this very unlikely. The data presented here, after controlling for frequency and observation geometry

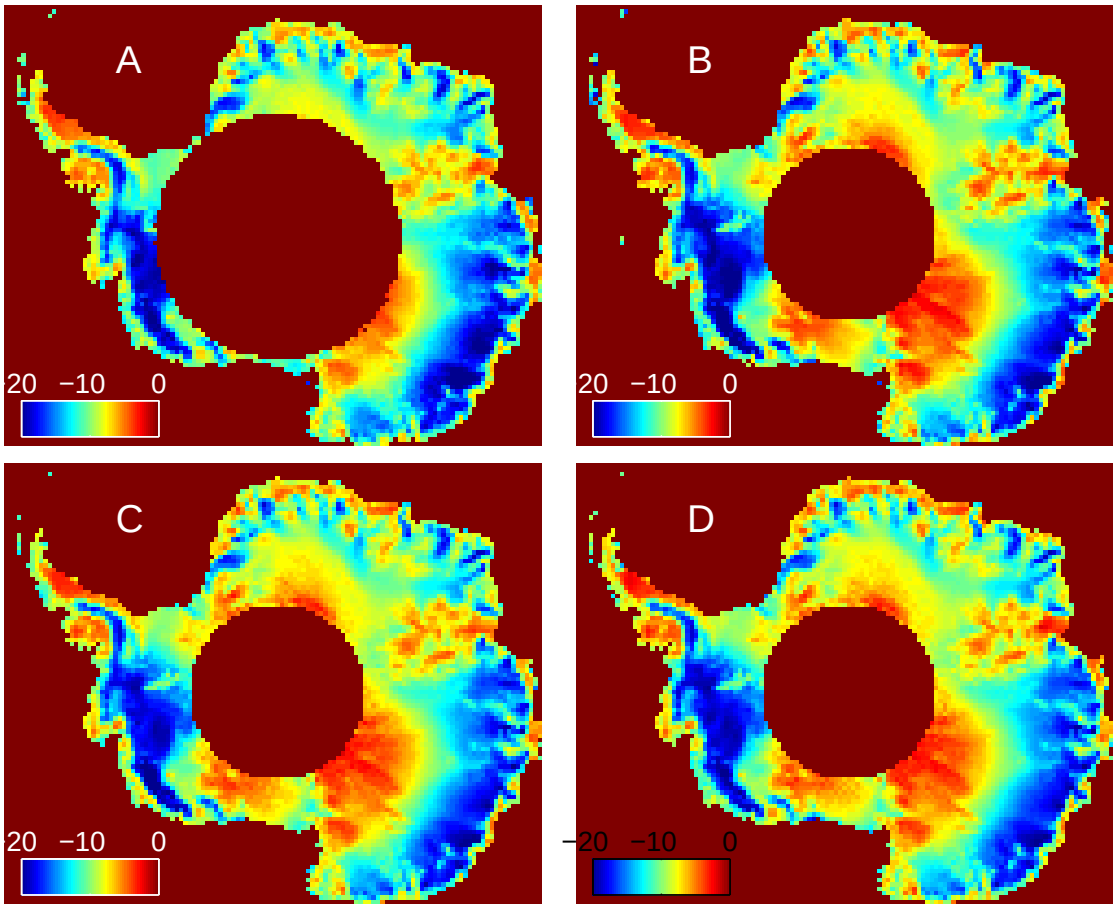

Figure 5.10: *A* maps. A) SASS, 1978. B) NSCAT, 1997. C) QuikSCAT, 1999. D) QuikSCAT, 2007.

differences, demonstrates that there are large-scale, spatially coherent changes in the backscatter signature of most of the Antarctic ice sheet. These changes are likely the result of changes in the composition of the ice sheet due to melting, accumulation, thermal forcing, and firn diagenesis. The data presented also demonstrates the utility of space-borne scatterometry, including combined observations from different sensors, in monitoring changes in the Antarctic ice sheet.

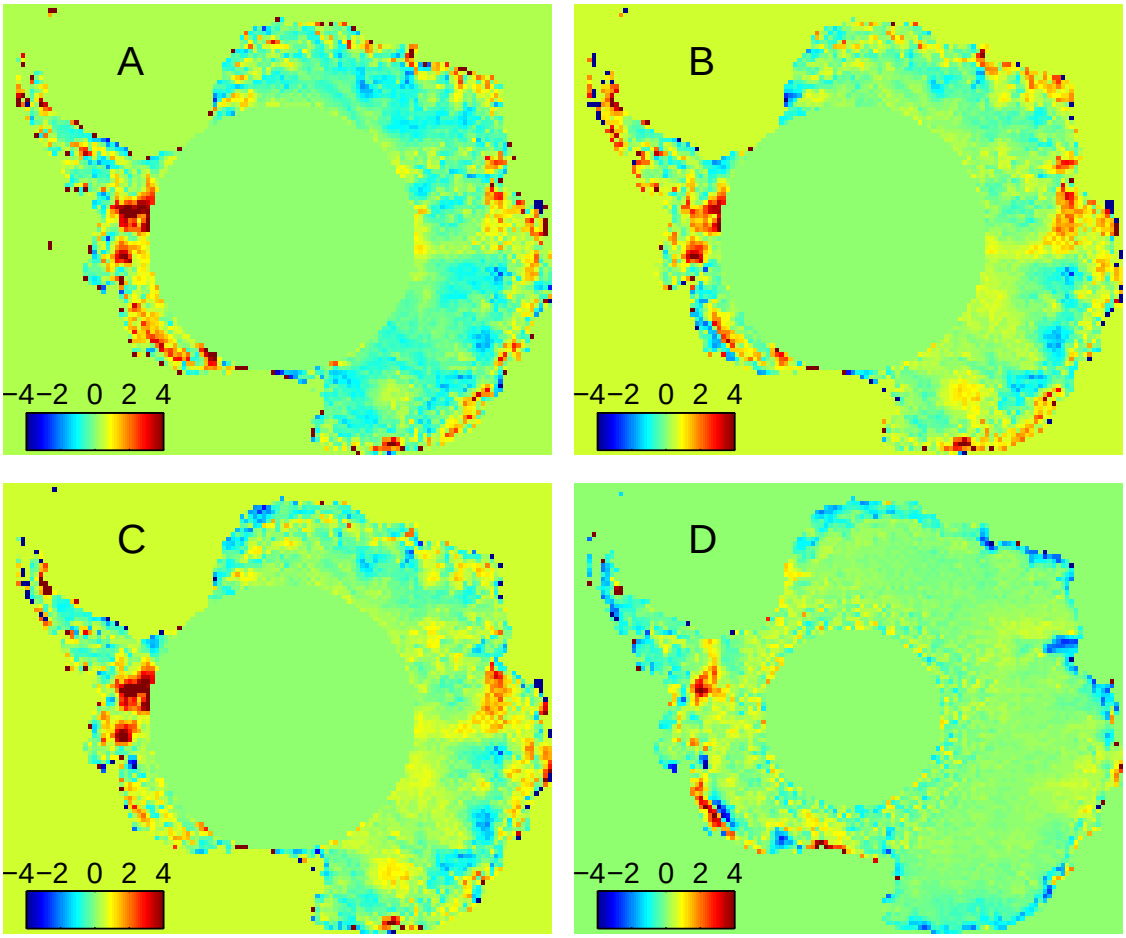

Figure 5.11: *A* difference maps. A) SASS 1978 - NSCAT 1997. B) SASS 1978 - QuikSCAT 1999. C) SASS 1978 - QuikSCAT 2007. D) QuikSCAT 1999 - QuikSCAT 2007.

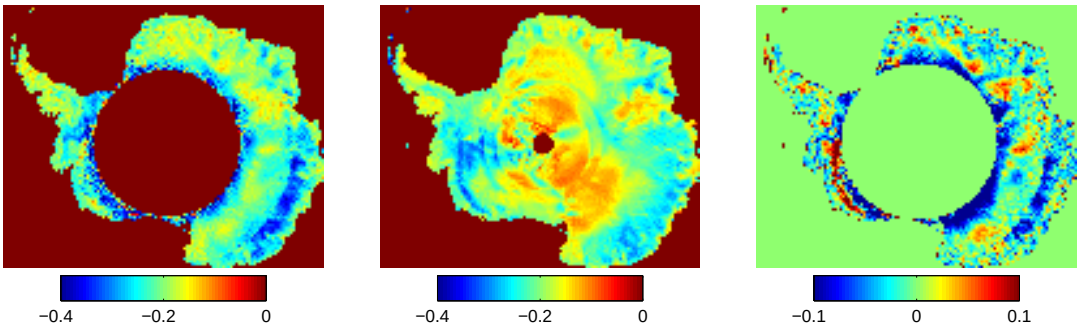

Figure 5.12: *B* images and *B* difference image. Left) SASS, 1978. Center) NSCAT, 1997. Right) SASS 1978 - NSCAT 1996. Large negative values near the center are artifacts from insufficient coverage by SASS.

Chapter 6

Summary and Conclusion

In this thesis I apply previously used backscatter signature observation techniques to data collected over the Antarctic ice sheet by three Ku-band space-borne scatterometers. The results are compared to find regions of significant seasonal, interannual, and long-term (multi-decadal) change. I find many such regions and propose and discuss the possibly responsible geophysical mechanisms. As warranted I also discuss the precision with which data from single and multiple sensors can be meaningfully compared.

6.1 Contributions

My specific contributions to the field of remote sensing and Antarctic studies are the following:

- I introduce a useful data binning system that achieves balance between spatial and temporal resolution for continent-scale studies.
- I confirm that QuikSCAT's observation geometry has remained consistent throughout its mission.
- I verify that backscatter measurements made by QuikSCAT have been consistent and can be very precisely compared to throughout its mission. This is a significant to finding to any researcher who uses QuikSCAT data.
- I confirm previous analysis made of high spatial-resolution Antarctic images. Since I use only raw backscatter measurements and not resolution enhanced images in my analysis, I am confident that the results are not influenced by unintended image processing artifacts from the resolution enhancement.

- I confirm that the crest of the Antarctic ice sheet is a suitable calibration location, despite seasonal temperature variations.

- I show that large portions of Antarctica experience large seasonal and interannual variations in backscatter signature. I attribute these changes to various geophysical causes, such as melting and accumulation.

- I identify regions of second and fourth order azimuth modulation in East Antarctica, and demonstrate that these quantities undergo significant seasonal and interannual variations. All previous similar studies of which I am aware considered change only in average backscatter and incidence angle dependence.

- I confirm that observations made from different sensors can be meaningfully compared after adjusting for observation geometry and frequency differences.

6.2 Future Work

The Antarctic ice sheet will remain a subject of intense study for many years to come. Future missions will contribute to the store of data to be analyzed and interpreted. Analysis of available data is by no means exhausted. Given that QuikSCAT is nearing its tenth year of nearly continuous service it might be possible to perform melt detection analysis on portions of Antarctica's wet snow zone to determine if the severity or frequency of Antarctic melt events is changing. Another possible avenue for future study is enhanced spatial resolution analysis of changes in the ice sheet. My continent-wide analysis requires a rather coarse spatial bin size, which likely obscures many interesting small-scale features. Of course, an enhanced resolution analysis would require a greater tolerance for image noise (see Appendix A).

During the late stages of writing this thesis JPL released the Beta version of QuikSCAT data for its entire mission [23]. By necessity my analysis used the original version of the data for 1999 through the end of 2005, and the Beta version for 2006 and 2007. Although the changes were shown to be very small, an easy - if somewhat tedious and computationally intensive - improvement of the research in this thesis would be to repeat my analysis with a fully consistent, all Beta, data set. There is

also a real need to expand my study of QuikSCAT's backscatter stability to include other, non-Antarctic, terrestrial targets.

In any case, scatterometry is only the first step in monitoring for future changes in the ice sheet. The most important work to be done in this field is to relate scatterometer findings to climate patterns to improve weather forecasting techniques and predict long-term climate changes, a task far beyond the abilities and interests of this humble electrical engineer. There are of course myriad other ways to use remote sensing instruments and techniques to improve and expand our present understanding of the Antarctic ice sheet.

Bibliography

[1] West Antarctic Links to Sea-Level Estimation Workshop at the University of Texas at Austin, "Statement: Thinning of West Antarctic ice sheet demands improved monitoring to reduce uncertainty over potential sea-level rise," http://www.jsg.utexas.edu/walse/statement.html, 2007. 1

[2] M. R. Drinkwater and D. G. Long, "Seasat, ERS-1/2 and NSCAT scatterometer observed changes on the large ice sheets," *Joint ESA-Eumestat Workshop on Emerging Scatterometer Applications*, pp. 91–95, 1998. 1

[3] D. Long and M. Drinkwater, "Azimuth variation in microwave scatterometer and radiometer data over Antarctica," *IEEE Transactions on Geoscience and Remote Sensing*, vol. 38, pp. 1857–1870, July 2000. 1, 2, 36, 47, 48, 51, 54, 74

[4] A. Bingham and M. Drinkwater, "Recent changes in the microwave scattering properties of the Antarctic ice sheet," *IEEE Transactions on Geoscience and Remote Sensing*, vol. 38, no. 4, pp. 1810–1820, July 2000. 1, 2, 63, 64, 66

[5] J. D. Flach, K. C. Partington, C. Ruiz, E. Jeansou, and M. R. Drinkwater, "Inversion of the surface properties of ice sheets from sateliete microwave data," *IEEE Transactions on Geoscience and Remote Sensing*, no. 4, pp. 743–752, 2005. 2, 64

[6] I. S. Ashcraft and D. Long, "Multi-annual changes in microwave backscatter over the Greenland ice sheet," *Proceedings of the International Geoscience and Remote Sensing Symposium*, pp. 958–960, 2001. 2, 75

[7] D. Long, I. Ashcraft, and J. B. Luke, "Observations of sastrugi on the great ice sheets," *Proceedings of SPIE Earth Observing Systems VIII*, vol. 5151, pp. 609–618, 2003. 2, 47, 48

[8] M. S. Moran, A. Vidal, D. Troufleau, Y. Inoue, and T. A. Mitchell, "Ku- and c-band sar for discriminating agricultural crop and soil conditions," *IEEE Transactions on Geoscience and Remote Sensing*, vol. 36, pp. 265 – 272, 1998. 2

[9] P. Hardin and D. G. Long, "Integration of sass ku-band imagery and avhrr imagery for historical tropical forest inventory," *Proceedings of the Topical Symposium on Combined Optical-Microwave Earth and Atmospheric Sensing*, pp. 232–235, 1993. 2

[10] H. Stephen and D. Long, "Spatial and temporal behavior of microwave backscatter directional modulation over the saharan ergs," *IEEE Transactions on Geoscience and Remote Sensing*, vol. 45, no. 5, pp. 116–1173, 2007. 2

[11] H. Liu and L. W. anf Kenneth C. Jezek, "Automated delineation of dry and melt snow zones in Anarctica using active and passive microwave observations from space," *IEEE Transactions on Geoscience and Remote Sensing*, pp. 2152 – 2163, 2006. 2, 6, 10

[12] British Antarctic Survey, http://www.antarctica.ac.uk/about_antarctica/geography/ice/sheets.php. 5

[13] Intergovernmental Panel on Climate Change, "Physical science basis of climate change," http://ipcc-wg1.ucar.edu/wg1/wg1-report.html, 2007. 5

[14] National Snow and Ice Data Center, Radarsat Antarctic Mapping Project Digital Elevation Model. 9, 63

[15] NASA, http://visibleearth.nasa.gov/view_rec.php?vev1id=11656. 9

[16] W. Patterson, *The Physics of Glaciers*, 3rd ed., 1994. 5

[17] F. T. Ulaby, R. K. Moore, and A. K. Fung, *Microwave Remote Sensing: Active and Passive*. Artech House, Inc., 1986, vol. 2. 7, 76

[18] J. W. Johnson, J. Leon A. Willims, E. M. Bracalente, F. B. Beck, and W. L. Grantham, "Seasat-a satellite scatteromoter instrument evaluation," *IEEE Journal of Oceanic Engineering*, vol. OE-5, no. 2, pp. 138–144, 1980. 7

[19] D. G. Long and M. R. Drinkwater, "Greland ice-sheet surface properties observed by the Seasat-A scatterometer," *Journal of Glaciology*, pp. 213–230, 1994. 7

[20] D. Early and D. Long, "Image reconstruction and enhanced resolution imaging from irregular samples," *IEEE Transactions on Geoscience and Remote Sensing*, vol. 39, pp. 291–302, 2001. 8, 75, 105

[21] F. Naderi, M. Freilich, and D. G. Long, "Spaceborne radar measurement of wind velocity over the ocean - an overview of the NSCAT scatterometer system," *Proceedings of the IEEE*, vol. 79, no. 6, pp. 850 – 866, 1991. 8

[22] Brigham Young University Microwave Earth Remote Sensing Labratory, "Scatterometer Climate Record Pathfinder," ftp://ftp.scp.byu.edu/. 12, 105

[23] Jet Propulsion Labratory, "SeaWinds data release beta description," ftp://podaac.jpl.nasa.gov/pub/ocean_wind/seawinds/doc/SeaWinds_Beta_Release.pdf. 12, 92

[24] N. I. Fisher, *Statistical analysis of circular data*. Cambridge University Press, 1993. 27

[25] K. V. Mardia, *Statistics of Direction Data*. Academic Press, 1972. 27

[26] D. Long and G. Skouson, "Calibration of spaceborne scatterometers using tropical rainforests," *IEEE Transactions on Geoscience and Remote Sensing*, vol. 34, no. 2, pp. 413–424, 1995. 36

[27] L. Kunz and D. Long, "Calibrating SeaWinds and QuikSCAT scatterometers using natural land targets," *Geoscience and Remote Sensing Letters*, vol. 2, pp. 182–186, 2005. 36, 66

[28] "The confluence zone of intense katabatic winds at terra nova bay, Antarctica, as derived form airborne sastrugi surveys and mesoscale numerical modeling," *Journal of Geophysical Research*, vol. 95, pp. 5495–5509. 36

[29] National Center for Atmospheric Research, http://dss.ucar.edu/, Bloulder, Colorado. 37, 63

[30] G. Hyland and N. Young, "Wind-induced directional anisotropy of microwave backscatter and its impact on imaging of the Antarctic continental snow cover," *IEEE Geoscience and Remote Sensing Symposium Proceedings*, pp. 1988–1990, 1998. 47, 51

[31] B. Lambert and D. G. Long, "Large-scale Ku-band backscatter model of the East-Antarctic megadune fields," *Proceeding of the International Geoscience and Remote Sensing Symposium*, pp. 3832 – 3834, 2006. 47

[32] I. Ashcraft and D. Long, "Observation and characterization of radar backscatter over Greenland," *IEEE Transactions on Geoscience and Remote Sensing*, vol. 43, pp. 237–246, 2005. 47

[33] F. Li, G. Neumann, S. Shaffer, , and S. L. Durden, "Studies of the location of azimuth modulation minima for ku band ocean radar backscatter," *Journal of Geophysical Research*, vol. 93, pp. 8229 – 8238, 1988. 48

[34] T. R. Parish and D. H. Bromwich, "The surface windfield over the Antarctic ice sheet," *Nature*, vol. 328, pp. 51–54, 1987. 51

[35] M. Frezotti, S. Gandolfi, and S. Urbini, "Snow megadunes in Antarctica: Sedimentary structure and genesis," *Journal of Geophysical Research*, vol. 107, p. 4344, 2002. 52

[36] M. A. Fahnestock, T. A. Scambos, C. A. Shuman, R. J. Arthern, D. P. Winebrenner, and R. Kwok, "Snow megadune fields on the East Antarctic plateau: extreme atmosphere-ice interaction." 52

[37] R. Bindschadler, "Future of the west antarctic ice sheet," *Science*, vol. 282, no. 5388, pp. 428 – 429, 1998. 53

[38] R. Bindschadler and P. Vornberger, "Changes in the west antarctic ice sheet since 1963 from declassified satellite photography," *Science*, pp. 689–692, 1998. 53

[39] T. Haran, J. Bohlagnder, T. Scambos, and M. Fahnestock, 2005, MODIS Mosaic of Antarctica. National Snow and Ice Data Center, digital media. 55, 63

[40] S. Nghiem, K. Steffen, G. Neumann, and R. Huff, *Dynamic planet: monitoring and understanding a dynamic planet with geodetic and oceanographic tools*. Springer, 2007, ch. Snow accumulation and snowmelt monitoring in Greenland and Antarctica, pp. 31–38. 57

[41] M. R. Drinkwater, D. G. Long, and A. W. Bingham, "Greenland snow accumulation estimates from satellite radar scatterometer data," *Journal of Geophysical Research*, vol. 106, no. D24, pp. 33 935–33 950, 2001. 64

[42] L. Kunz and D. Long, "Melt detection in Antarctic ice shelves using scatterometers and microwave radiometers," *IEEE Transactions on Geoscience and Remote Sensing*, vol. 44, pp. 2461–2469, 2006. 73

[43] M. R. Drinkwater and D. G. Long, "Seasat, ERS-1/2 and NSCAT scatterometer observed changes on the large ice sheets," *Proceedings of the International Geoscience and Remote Sensing Symposium*. 75

[44] M. Gay, M. Fily, C. Genthon, M. Frezzotti, H. Oerter, and J. Winther, "Snow grain-size measurements in Antarctica," *The Journal of Glaciology*, pp. 527–535, 2002. 76

[45] D. C. Montgomery, E. A. Peck, and G. G. Vining, *An Introduction To Linear Regression Analysis*, 4th ed. 103

Appendix A

Resolution Optimization

In Chapter 3 I choose to bin QuikSCAT data into approximately 45 km by 45 km, four-day-long bins. This binning scheme is a compromise between temporal resolution, spatial resolution, and noise. In this section I demonstrate how these three quantities are related. QuikSCAT has a nominal antenna footprint size of 25 km by 37 km. Pixels larger than this allow for more meaningful averaging and aggregation of data, and thus reduces noise, at the expense of resolution. Pixels smaller than this, cause a single footprint to spill into adjacent pixels, increasing noise as well as resolution. There is a similar compromise between temporal bin size and noise. Since temporal bins of four days have already been shown to obscure short-duration melt events (see Figure 4.12), temporal bins of longer than four days are not considered, despite the possibly large improvements in signal to noise ratio.

Figure A.1 shows maps of fourth order azimuth modulation phase (ϕ_4), the backscatter quantity most sensitive to small changes in azimuthal variation, for six different bin configurations: 22 km by 22 km 45 km by 45 km and 90 km by 90 km spatial bins, and two and four day long temporal bins. There are insufficient data points to find meaningful values for the nine coefficients of the empirical model (Equation 4.1) at finer spatial resolutions without using much longer temporal bins. Indeed, even the two day 22 km by 22 km case shows insufficient data over most of the continent. Both 90 km by 90 km images show intolerable spatial resolution, and actually show and increased noise level, likely the result of backscatter from many different targets being binned together. The two day 45 km by 45 km case and the four day 22 km by 22 km case both show acceptable noise and resolution. The four day 45 km by 45 km case shows more coverage at extreme southern latitudes than

the two day 45 km by 45 km case and less noise in many locations than the four day 22 km by 22 km case.

Thus I find the four day 45 km by 45 km case represents the best spatial bin size given the maximum tolerable temporal bin size for this thesis. For analysis of only locations with very strong fourth order modulation, such as Wilkes Land, it is likely the four day 22 km by 22 km binning scheme would also be sufficient. Were the focus of this thesis on spatial, not temporal, distribution of backscatter signature parameters, a single, extremely long (up to, say, 28 day) temporal bin observed during the austral winter may be appropriate.

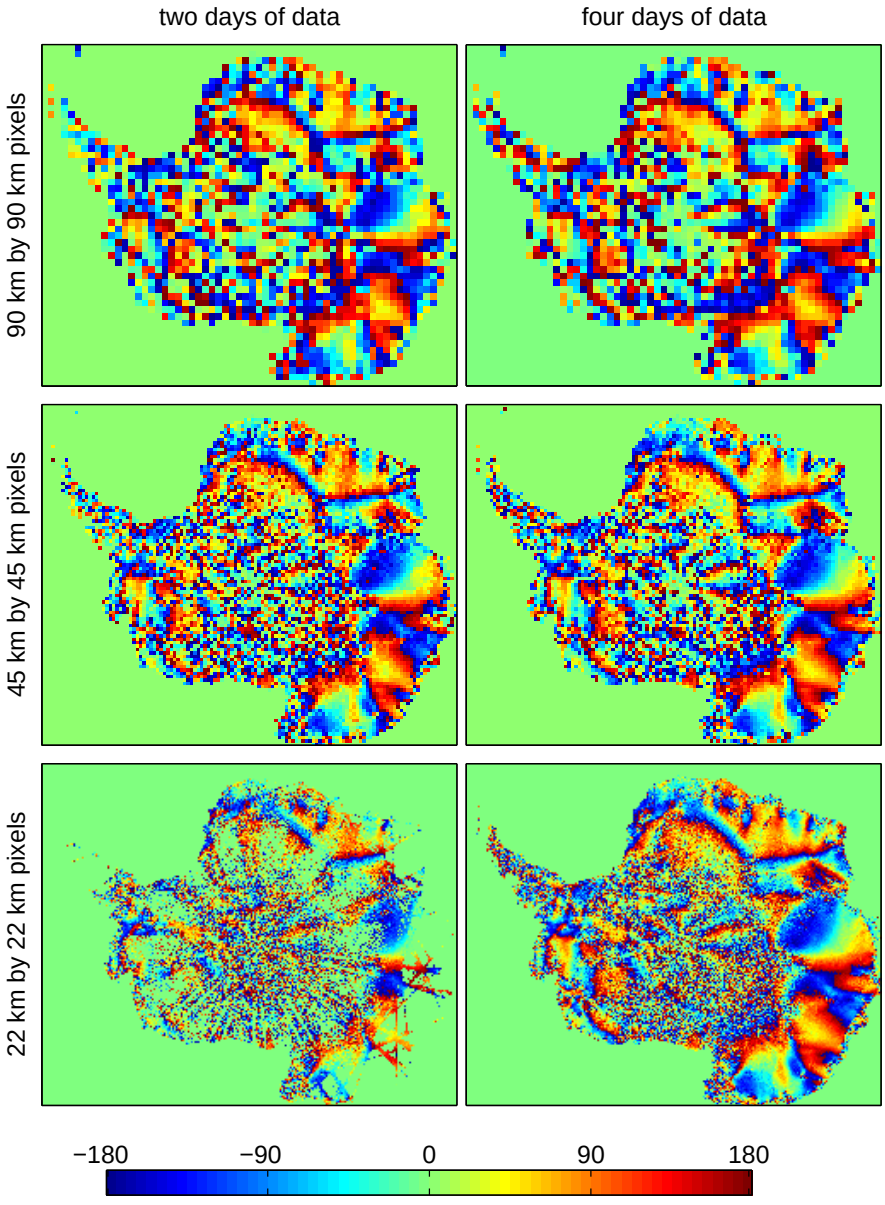

Figure A.1: Maps of fourth order azimuth modulation phase (ϕ_4) at various resolutions. Left Column) Two day (177 through 178, 2003) images. Right Column) Four day (177 through 180, 2003) images. Top Row) 90 km by 90 km pixel size. Second Row) 45 km by 45 km pixel size. Third Row) 22 km by 22 km pixel size.

Appendix B

Weighted Least Squares Regression and Hypothesis Testing

This appendix summarizes a classical approach to testing the significance of a regressing line found using a weighted least squares technique. Similar discussions can be found in any standard text on regression analysis (for example [45]).

Let (x_i, y_i) be ordered pairs of data, for $i = 1, \ldots, N$ where x is considered the independent variable and y is considered the dependent variable, and define $x = [x_1 \cdots x_N]^T$, $y = [y_1 \cdots y_N]^T$. If we assume x_i and x_j are independent for $i \neq j$, and each has known variance, $\text{var}(x_i) = \sigma_i^2$, then the variance of x is given as $\text{var}(x) = diag(\sigma_1^2, \cdots, \sigma_N^2)$, which we assign as the inverse of the weighting matrix: $W^{-1} = \text{var}(x)$.

We wish to model y as a linear function of x,

$$\sigma_i^0 = my_i + b, \tag{B.1}$$

and test the hypotheses

$$H_0 : \quad m = 0, \tag{B.2}$$

$$H_1 : \quad m \neq 0. \tag{B.3}$$

H_0 is the null hypothesis and is the quantity to be tested. To do this first define the following matrices

$$\beta = [\, b \;\; m \,]^T, \tag{B.4}$$

$$X = \begin{bmatrix} 1 & y_1 \\ 1 & y_2 \\ \vdots & \vdots \\ 1 & y_N \end{bmatrix}. \tag{B.5}$$

Then the minimum variance unbiased estimator of the model coefficients is

$$\hat{\beta} = (X'W^{-1}X)^{-1}X'W^{-1}y. \tag{B.6}$$

The variance of $\hat{\beta}$ is easily solved for

$$\begin{aligned} \mathrm{var}(\hat{\beta}) &= (X'W^{-1}X)^{-1}X'W^{-1}\mathrm{var}(y)((X'W^{-1}X)^{-1}X'W^{-1})' && \text{(B.7)} \\ &= (X'W^{-1}X)^{-1}X'W^{-1}W((X'W^{-1}X)^{-1}X'W^{-1})' && \text{(B.8)} \\ &= (X'W^{-1}X)^{-1}X'W^{-1}WW^{-1}X(X'W^{-1}X)^{-1} && \text{(B.9)} \\ &= (X'W^{-1}X)^{-1}. && \text{(B.10)} \end{aligned}$$

Now we test the significance of the estimate of the slope $\hat{m}$. We normalize $\hat{m}$ to determine how many standard deviations it is away from the hypothesized mean. This quantity is known as the Z-score, $Z_m = \frac{\hat{m}}{\sqrt{\mathrm{var}(\hat{m})}}$. We calculate the significance, or p-value, of $\hat{m}$, as $p_m = erf(\frac{Z_m}{\sqrt{2}})$. Although interpretations of significance vary, a standard practice is to reject the null hypothesis in favor of the alternative if p exceeds some threshold, usually 0.90, 0.95, or 0.99.

Appendix C

Processing

As part of my research I have been responsible for processing global enhanced resolution remote sensing images using the scatterometer image reconstruction (SIR) algorithm [20] and maintaining a publicly available database of such images on the Microwave Earth Remote Sensing Laboratory's web site [22]. These responsibilities involve using one of BYU's supercomputers, Marylou0, to produce over 2100 images per day and keeping the images logically arranged in the database. I also managed the implementation and assured the quality and consistency of new versions of the processing code as the code was updated to accommodate new research projects. Occasionally I processed special requests for regionally- or temporally-specific data sets, such as those for studies of rain rates in the Amazon, Australia, various Greenland studies, and the break up of the Wilkins Ice Shelf, in addition to processing the standard products. After three years I have processed, archived, and quality assured over 16 TB of images and associated data products.